# Development of a SERS aptasensor for detection of medical residues

**Frøhling, Kasper Bayer; Jakobsen, Mogens Havsteen; Boisen, Anja; Bache, Michael**

*Publication date:*
2015

*Document Version*
Publisher's PDF, also known as Version of record

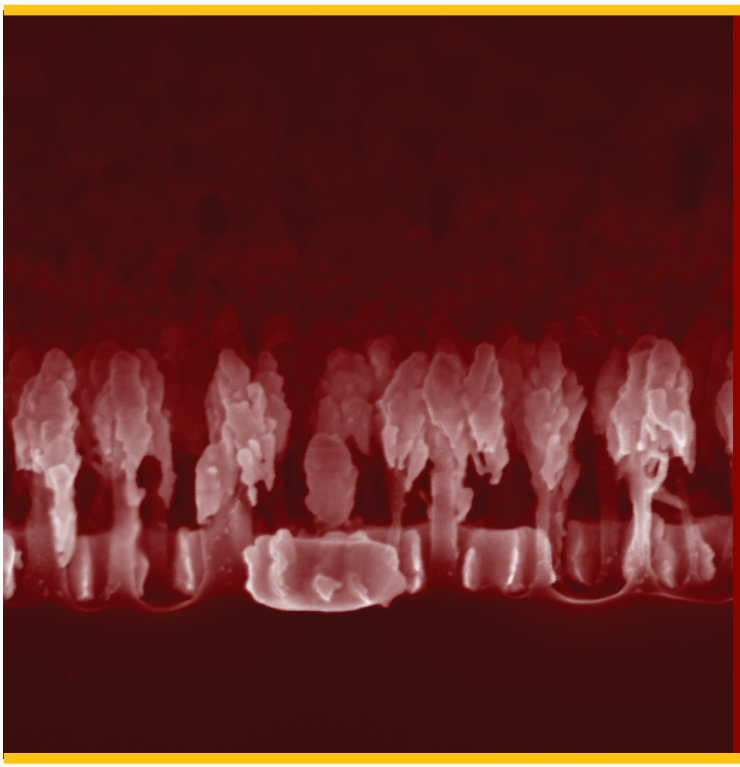

# Development of a SERS aptasensor for detection of medical residues

Kasper Bayer Frøhling
PhD Thesis August 2015

DTU Nanotech
Department of Micro- and Nanotechnology

Front page: Scanning electron microscopy image of gold coated silicon nanopillars (side view).

Back page: Scanning electron microscopy image of gold coated silicon nanopillars (top view)

*To my beloved wife*

# Preface

This thesis has been submitted as partial fulfilment of the requirements for obtaining the Doctor of Philosophy (PhD) degree at the Technical University of Denmark (DTU). The work has mainly been carried out at Department of Micro- and Nanotechnology (DTU Nanotech) from 15 August 2012 to 14 August 2015. Part of the work has been carried out at Columbia University in the city of New York, United States of America in the period 1 February 2014 to 1 May 2014.

The work has been supervised by senior researcher Mogens Havsteen Jakobsen and co-supervised by professor Anja Boisen and postdoc Michael Bache in the groups of 'Surface Engineering' and 'Nanoprobes'.

The work was financially supported by the Multi Sensor DVD Platform (MUSE) project funded by Innovation Fund Denmark.

# Acknowledgements

I would like to express my gratitude to my supervisors Mogens Jakobsen, Anja Boisen and Michael Bache for allowing me to perform research in a very exciting field. Also project partners Grundfos A/S and ViroGates A/S provided opportunities and collaborations that I would not have been without. The research environment created by Surface Engineering and Nanoprobes groups at DTU Nanotech truly inspire creativity and teamwork. Tommy Alstrøm deserves praise for his skills with a computer, which was crucial for interpreting the large amounts of data generated throughout the project. I would likewise like to extent the praise to professor Lin at Columbia University in the city of New York for inviting me to perform experiments in his laboratory. Jaeyoung Yang and Mirko Palla were exceptionally welcoming and helpful during my external stay, which aided in debugging the experimental problems encountered.

I would also like to recognise the social environment at DTU Nanotech. Especially Line, Mette and Tanya for providing invaluable amounts of cake, conversations and laughter. Some of this took place in the Friday Bar where my partner-in-crime, Peter, fortunately joined the crew of Lene, Marie and François alongside me. It was a place where many friendships where founded and beer bottles emptied. I have spent countless evenings there in the company of Søren and David, discussing every little detail in beer flavours and the like.

I want to thank my family for always supporting me in my choices throughout life. Lastly I want to thank my newly-wedded wife for supporting me throughout my education. It has not been an easy ride, but you stood firmly beside me. I dedicate this work to you.

# Abstract

Low levels of medical residues in environmental, industrial and domestic water systems is a growing concern. The biosensor industry is trying to accomodate the need of sensitive and specific sensor systems capable of ultra-low level detection of medical residues.

In this PhD project a surface enhanced Raman spectroscopy (SERS) sensor for the female sexhormone 17$\beta$-estradiol was attempted. It is commonly used in contraceptive pills from where it find its way through waste water treatment plants and into the environment. The SERS substrate was fabricated in a cleanroom facility using techniques well known from the electronics industry. The substrate consisted of silver or gold covered silicon nanopillars. The nanopillars were chemically functionalised with a DNA aptamer specific towards 17$\beta$-estradiol using thiol chemistry.

At first, an entire functionalisation protocol was carried out to detect Estradiol Glow, which is fluorescently labelled 17$\beta$-estradiol. It was shown that Estradiol Glow exhibit very strong Raman activity and was such ideal for initial test. Since a large amount of data was gathered for this experiment it was necessary to develop an algorithm capable of analysing large data sets. Non-negative Matrix Factorization (NMF) was utilised to effectively improve the detection limit of the system by one order of magnitude.

Due to issues relating to the functionalisation protocol it was secondly investigated whether the aptamer was properly immobilised on the nanopillar surface. By hybridisation to a labelled complementary strand it was proven that aptamer was indeed immobilised. It was also found that stronger binding to the gold covered nanopillars could be obtained by a short treatment in reactive $O_2$ plasma. Likewise it was found that the addition of a detergent to the washing buffer had a great influence on the unspecific binding to the nanopillars.

A thorough study of the parameters influencing the degree of functional-

isation was then conducted. By utilizing a developed peak-fitting model it was possbible to directly inspect the interplay between DNA aptamer and 6-mercapto-1-hexanol (MCH) used for blocking unspecific binding to gold. By inspecting the spectra of the molecules and their combination it was possible to observe attachment of DNA aptamer and MCH. Displacement/removal of DNA aptamer was also observed for high concentrations of MCH.

The final study was an attempt to detect pure 17$\beta$-estradiol using the developed functionalisation parameters. Unfortunately the inherent weak Raman signal of 17$\beta$-estradiol proved to faint for direct detection. Therefore Estradiol Glow was employed, however without success. Despite several attempts with varying degree of stringency successful detection was never accomplished.

In conclusion, this PhD project successfully characterised the chemical functionalisation parameters needed for generic SERS aptasensor development using only the Raman signals of the molecules. The SERS substrate was successfully fabricated repeatedly and showed great enhancement of Raman signals. Two analysis methods (NMF and peak-fitting) was developed in collaboration with DTU Compute in order to accomodate for the large amount of data gathered throughout the project. This work displays the complexity in SERS aptasensor development, which is needed for sensitive and selective capture of medical residues.

# Dansk resumé

Små mængder af forskellige medicinrester i vandmiljøer er et stigende problem. Blandt eksperter spekuleres der i, om der kan forekomme krydsreaktioner mellem medicinrester på trods af den meget lave mængde. Derfor bliver der brugt mange midler indenfor udvikling af såkaldte biosensorer, som er i stand til at detektere forskellige molekyler i ultra-lave koncentrationer. Ved hurtigt at detektere farlige stoffer er det muligt, at sætte ind overfor problemerne før de udvikler sig.

I dette ph.d.-projekt er det forsøgt, at udvikle en molekylær biosensor mod det kvindelige kønshormon 17$\beta$-østradiol. 17$\beta$-østradiol bruges almindeligvis i p-piller, hvorfra det finder vej ud i kloakken. På nuværende tidspunkt renses der ikke for stoffet på rensningsanlæg, hvilket gør, at det hober sig op i naturen.

Den udviklede sensor er baseret på Surface Enhanced Raman Spectroscopy (SERS). De følsomme SERS sensorer består af nanostrukturerede overflader, som er fabrikeret ved brug af renrumsfaciliteter kendt fra elektronikindustrien. Nanostrukturerne er fabrikeret i silicum, som sidenhen er pålagt et tyndt lag guld eller sølv. Dernæst er de blevet kemisk funktionaliseret med DNA aptamerer, som specifikt kan binde 17$\beta$-østradiol.

Til at starte med blev det forsøgt, at detektere en fluorescerende variant af 17$\beta$-østradiol kaldet Estradiol Glow. Det blev bevist, at Estradiol Glow har et meget stærkt og karakteristisk Raman spektrum, hvilket gjorde det ideelt til indledende forsøg. I disse forsøg blev der opsamlet store datamængder, hvilket gjorde det nødvendigt at udvikle en matematisk algoritme til brug i dataanalysen. Non-negative Matrix Factorization (NMF) blev anvendt til, at forbedre detekteringsgrænsen for Estradiol Glow med én størrelsorden.

Som det næste blev det undersøgt, om DNA aptameren var ordentligt immobiliseret på den nanostrukturerede overflade. Dette skyldtes problemer relateret til den kemiske funktionalisering, der blev opdaget under det indledende

forsøg. Ved at hybridisere en komplimentær DNA streng til DNA aptameren, blev det bevist, at immobiliseringen var en succes. Under forsøgene blev det også bevist, at en rensning af guldoverfladen i oxygenplasma øgede bindingen betragteligt. Ligeledes blev det vist, at tilsætning af detergent til vaskeproceduren af overfladen, havde stor indvirkning på graden af uspecifik binding.

Et grundigt studie i parametrene forbundet med den kemiske funktionalisering blev sidenhen udført. Ved at anvende en udviklet peak-fitting model blev det muligt at inspicere funktionaliseringen direkte vha. Raman spektrene. Her blev det vist, at DNA aptamer og 6-mercapto-1-hexanol (MCH), som bruges til at eliminere uspecifik binding til guld, interagerer på den nanostukturerede overflade. Ved brug af for stor mængde MCH blev det observeret at DNA aptamer blev fjernet fra overfladen. Ud fra disse målinger kunne et sæt parametre vælges til videre forsøg.

Det sidste studie var et forsøg på at detektere rent 17$\beta$-østradiol vha. den udviklede kemiske funktionalisering. Desværre viste stoffet sig, at have en meget lav Raman aktivitet og det var ikke muligt, at adskille det i det komplekse spektrum fra DNA aptamer og MCH. Derfor blev det også forsøgt at detektere Estradiol Glow, da det tidligere havde vist sig at have et stærkt og karakterisk Raman signal. På trods af flere forsøg med varierende grad af stringens blev en succesfuld detektering aldrig opnået.

Afslutningsvis kan det konstateres, at dette ph.d.-projekt lykkedes med at udvikle en kemisk funktionalisering af en nanostruktureret overflade til brug i en SERS biosensor. Analysen som ligger forud for disse parametre kan bruges som en generel fremgangsmåde til udvikling af SERS biosensorer baseret på DNA aptamerer. SERS sensoren blev gentagne gange reproduceret og udviste fremragende sensoregenskaber. For at kunne håndtere den store datamængde som blev genereret igennem projektet, blev to analysemetoder (NMF og peak-fitting) udviklet i samarbejde med DTU Compute. Dette ph.d.-projekt afspejler den store kompleksitet der er forbundet med udviklingen af en SERS sensor baseret på DNA aptamerer. På trods af, at detektering af 17$\beta$-østradiol mislykkedes, har denne type sensor dog stor potentiale i effektivt, at detektere medicinrester i ultra-lave koncentrationer.

# Contents

# List of Figures

# List of Tables

# List of abbreviations

| Abbreviation | Explanation |
|---|---|
| Aptasensor | Molecular sensor using aptamers as recognition element |
| BiASERS | SERS using a bi-analyte technique |
| BPE | 1-2-di-(4-pyridyl)-ethylene |
| DNA | Deoxyribonucleic acid |
| cDNA | Complementary DNA |
| E-beam | Electron beam |
| EDTA | Ethylenediaminetetraacetic acid |
| FDA | Food and drug administration in USA |
| hCG | Human chorionic gonadotropin |
| HPLC | High-performance liquid chromatography |
| IgG | Immunoglobulin G |
| IR | Infrared |
| MALDI-TOF | Matrix assisted laser desorption/ionization - time of flight |
| MCH | 6-mercapto-1-hexanol |
| MUSE | Multi Sensor DVD Platform |

| Abbreviation | Explanation |
|---|---|
| ncDNA | Non-complementary DNA |
| NMF | Non-negative matrix factorization |
| NMR | Nuclear magnetic resonance |
| NSAID | Nonsteroidal anti-inflammatory drug |
| PBS | Phosphate buffered saline |
| PCA | Principal component analysis |
| PCR | Polymerase chain reaction |
| QCM-D | Quartz crystal microbalance with dissipation |
| RIE | Reactive ion etch |
| RNA | Ribonucleic acid |
| SAM | Self-assembled monolayer |
| SELEX | Systematic evolution of ligands by exponential enrichment |
| SEM | Scanning electron microscopy |
| SERS | Surface enhanced Raman spectroscopy |
| SM-SERS | Single molecule SERS |
| SSC | Saline sodium citrate |
| suPAR | Soluble urokinase Plaminogen Activator Receptor |
| TBA | Thrombin binding aptamer |
| TBS | Tris-buffered saline |
| TCEP·HCl | Tris(2-carboxyethyl) phosphine hydrochloride |
| UV | Ultraviolet |

# List of publications

The following publications were achieved during the PhD project.

[Danish] Anna Line Brøgger and **Kasper Bayer Frøhling**. Mikrosensorer skal hjælpe skadestuer med prioritering af patienter. *Dansk kemi*, Vol. 94, No. 9, **2013**, p. 12-14.

Anna Line Brøgger, Filippo Bosco, Michael Bache, **Kasper Bayer Frøhling**, En-Te Hwu, Ching-Hsiu Chen, Jesper Eugen-Olsen, Ing-Shou Hwang, Anja Boisen. Towards Picomolar Detection with DVD-ROM Optical Technology. *Proceedings of 2013 Nanomechanical Sensing Workshop*. **2013**.

Michael Bache, Filippo Bosco, Anna Line Brøgger, **Kasper Bayer Frøhling**, Tommy Sonne Alstrøm, En-Te Hwu, Ching-Hsiu Chen, Jesper Eugen-Olsen, Ing-Shouh Hwang, Anja Boisen. Nanomechanical recognition of prognostic biomarker suPAR with DVD-ROM optical technology. *Nanotechnology*, Vol. 24, No. 44, 444011, **2013**.

Tommy Sonne Alstrøm, **Kasper Bayer Frøhling**, Jan Larsen, Mikkel Nørgaard Schmidt, Michael Bache, Michael Stenbæk Schmidt, Mogens Havsteen Jakobsen, Anja Boisen. Improving the robustness of Surface Enhanced Raman Spectroscopy based sensors by Bayesian Non-negative Matrix Factorization. *Proceedings of the 2014 IEEE International Workshop on Machine Learning for Signal Processing (MLSP)*, **2014**.

Tommy Sonne Alstrøm, Filippo Bosco, Jan Larsen, Michael Bache, Anna Line Brøgger, **Kasper Bayer Frøhling**, En-Te Hwu, Ching-Hsiu Chen, Ing-Shouh Hwang, Anja Boisen. Characterization of the time-evolving bending profile of micro-cantilevers. *Poster session presented at 11th International Workshop on*

*Nanomechanical Sensing*, **2014**, Madrid, Spain.

**Kasper Bayer Frøhling**, Tommy Sonne Alstrøm, Michael Bache, Michael Stenbæk Schmidt, Mikkel Nørgaard Schmidt, Jan Larsen, Mogens Havsteen Jakobsen, Anja Boisen. Statistical analysis of large areas of Raman mapped DNA functionalized gold coated silicon nanopillar SERS substrates. *8th International Conference on Advanced Vibrational Spectroscopy*, Oral presentation, **2015**, Vienna, Austria.

**Kasper Bayer Frøhling**. Detection of small organics in water - the MUSE project. *Danish Water Forum*, Oral presentation, **2015**, Copenhagen, Denmark.

An additional manuscript has been submitted to the journal 'Vibrational Spectroscopy':

**Kasper Bayer Frøhling**, Tommy Sonne Alstrøm, Michael Bache, Michael Stenbæk Schmidt, Mikkel Nørgaard Schmidt, Jan Larsen, Mogens Havsteen Jakobsen, Anja Boisen. Surface-enhanced Raman spectroscopic study of DNA and 6-mercapto-1-hexanol interactions using large area mapping. *Vibrational Spectroscopy*, **submitted**.

The following patent application have been filed based on the methods and results described in section 4.3. It will become publicly available 18 months after filing date.

Tommy Sonne Alstrøm, Mikkel Nørgaard Schmidt, Jan Larsen, **Kasper Bayer Frøhling**, Anja Boisen, Michael Stenbæk Schmidt. Method to lower the detection limit and enhance the sensitivity of Surface Enhanced Raman based sensors, EPO 14185146.9-1504, filed 17 September 2014.

# 1 The MUSE Project

Detection of different biological species ranging from single molecules to whole cells, continues to challenge scientists and private companies worldwide. Discovering new and innovative methods to detect low levels of target analytes will have high impact in healthcare, food safety and environmental science. Especially molecular sensors with focus on biological markers (large molecules) or medical residues (small molecules) are of interest. Being able to detect biological markers in body fluids would enable clinicians to accurately diagnose patients, without having a to wait days for samples to be analysed in a centralised laboratory. Whereas detection of medical residues in environmental or waste water would enable environmental agencies to quickly analyse the chemical pollution of a sample. However it is not an easy task to develop molecular sensors since obtaining high sensitivity, selectivity, accuracy and reproducibility is crucial for a sensor to be reliable.

The Multi Sensor DVD Platform (MUSE) project aims at developing molecular sensors using micro- and nanofabrication for use in both diagnostics and environmental monitoring. Soluble urokinase Plasminogen Activator Receptor (suPAR) was discovered by clinicians at Hvidovre Hospital, Denmark [1] to be a prognostic biomarker. They found that suPAR blood levels correlated well with the degree of activation of the immune system, which enabled better interpretation of the severety of a given disease. The project partner ViroGates A/S pursues opportunities within this area and seek new sensors for quantitative detection of suPAR.

Another project partner, Grundfos A/S, pursues new sensors for trace amount detection of pharmaceuticals in water samples. A recent press release from the European Commission has highlighted the need for monitoring of pharmaceuticals in the aquatic environment [2]. This is due to the unknown effects of being exposed to several low level endocrine-disrupting chemicals, such as hormones and steroids, at once. This is known as the 'cocktail-effect' [3].

Development of a small, on-line sensor for domestic waste water monitoring is strategically important for Grundfos A/S.

Previous projects carried out within the group at DTU Nanotech aimed at developing highly sensitive molecular sensors [4]. Among others, microresonators (cantilevers) and Raman spectroscopy-based sensors were developed to facilitate sensitive and specific detection of molecules. The MUSE project aims at combining sensor technologies on a suitable miniaturized platform to complement each other. By combining the individual strengths of the different sensors it is possible to develop a powerful tool for molecular detection. To achieve this a DVD platform was chosen. Control of the rotation speed of a DVD-shaped polymer disc allows for accurate control of liquids in microchannels [5]. DVD optics can then be utilized to read out cantilever deflection or scattering of light on a nanostructured surface.

## 1.1 This PhD project

The aim of this PhD project was to develop chemical functionalisation protocols of sensor surfaces for selective capture of a specific target. Based on the needs of the commercial partners and the sensor technologies available two individual tracks where possible:

**Track 1** suPAR detection using anti-suPAR antibodies on cantilevers.

**Track 2** Hormone detection (particularly 17$\beta$-estradiol) detection using DNA aptamers on a Surface Enhanced Raman Spectroscopy (SERS) sensor.

suPAR detection was suggested on mass-sensitive cantilevers since suPAR is a large protein (60,000 Da). Whereas detection of the small molecule 17$\beta$-estradiol (272 Da) was suggested on the chemically sensitive SERS sensor. Early in the PhD project Track 2 was prioritised as the developed SERS sensor had shown excellent progress [6] and detection of suPAR was initiated on other platforms.

## 1.2 Thesis outline

A brief description of the MUSE project is given in chapter 1. Chapter 2 describes general concepts important for the experiments conducted throughout the project. A motivation is given to develop a biosensor towards 17$\beta$-estradiol. Chapter 3 describes fabrication of SERS substrates and the chosen chemical functionalisation strategy. Chapter 4 describes in detail the experiments carried out regarding development of a SERS sensor for 17$\beta$-estradiol detection. Chapter 5 and 6 provide conclusion to and outlook of the project.

## 1.3 Popular science publications

Two popular science publications were made during the project to communicate the efforts of the MUSE project to other scientific fields.

### Dansk Kemi

The following popular science article was published in the Danish Journal "Dansk Kemi" (english: Danish Chemistry). In brief it describes the potential of small, specific molecular sensors to improve efficiency in triaging hospital patients; if patients could more easily be risk assessed it would save time, money and hospitalisations. The inflammatory marker suPAR has the potential to meet these needs in combination with proper sensors.

It can be found at:
`http://ipaper.ipapercms.dk/TechMedia/DanskKemi/2013/9/`

### Oral presentation at 9th Annual Meeting of Danish Water Forum

The following popular science abstract was accepted for an oral presentation at 9th Annual Meeting of Danish Water Forum, 29 January 2015 in Copenhagen, Denmark. Briefly, it describes the efforts of the MUSE project in developing new sensitive sensors for environmental analysis.

It can be found at:
`http://www.danishwaterforum.dk/Research/Annual%20meeting%202015/Presentations/Proceedings_DWF_2015.pdf`

# 2 Introduction and Concepts

This chapter describes general concepts important for the experiments conducted throughout the project. The structural build-up of two successful commercial biosensors is outlined to provide in-depth understanding of the requirements for biosensing applications. Thereafter a brief description of chemical and physical forces involved in molecular interactions and biosensors is given. Antibodies and aptamers are described in order to yield appropriate background knowledge for the sensor development described in the project. Lastly, the SERS phenomenon is explained in combination with different aptasensors for 17$\beta$-estradiol.

## 2.1 Pharmaceuticals

The widespread use of pharmaceuticals has gained considerable attention lately, due to the potential risk of leakage into the environment causing disturbance to eco systems. The European Commission updated their chemical watch list to include pharmaceuticals for the first time in January 2012 [2]. The Commission does not question the medical effect of the chemicals, but raises concern about their influence on the environment. Common to the newly listed pharmaceuticals (17$\alpha$-ethinylestradiol, 17$\beta$-estradiol and diclofenac) is that they are all heavily used by humans on a daily basis. The first two are both female sex hormones used in contraceptive pills and hormonal treatment of menopausal women, whereas diclofenac is a nonsteroidal anti-inflammatory drug (NSAID) used for pain relieve and to reduce inflammation. These drugs are very resistant to degradation in the wild were animals are continuously exposed to low levels of the drugs. Studies have even shown that certain fish react very strongly to the presence of drugs, causing them to change sex [7]. Simultaneously the drugs are also not removed in many waste water treatment plants. This causes the drugs to enter the drinking water systems of domestic house-

holds. Even though the concentration of drugs is very low (typically at the pico- to nanomolar level) they still possess a risk for humans as these drugs can accumulate and have cross-reactions with other drugs. The latter is known as the 'cocktail effect' [3]; a drug may be harmless in a very low concentration, but added together with other low concentration drugs the effect may be severe. The cocktail effect is even thought to be the cause of the declining fertility in men, but the debate is still ongoing.

## 2.2 Biosensors

Miniaturised biosensor for point-of-care have been widely researched since the 1970s where the first home pregnancy test was approved by the FDA [8]. The development of miniaturised biosensors have greatly improved since then and they now come in various forms depending on their desired functionality. A general structural build-up can though be observed, shown schematically in Figure 2.1. A typical biosensor consists of a recognition element linked to an interface. Some biosensors do not require a recognition element, but instead relies on deconvolution of a complex signal. The recognition element is capable of selectively capturing a target analyte. The interface is connected to a transducer that transmits a signal to a computer when the analyte is caught. Typical transducers are electrochemical [9,10], optical [11–13] or electronic [14]. Each of these have different strengths and weaknesses and must be carefully chosen to achieve a specific functionality. Once a signal is received from the transducer it must be analysed and yield an appropriate answer to the user.

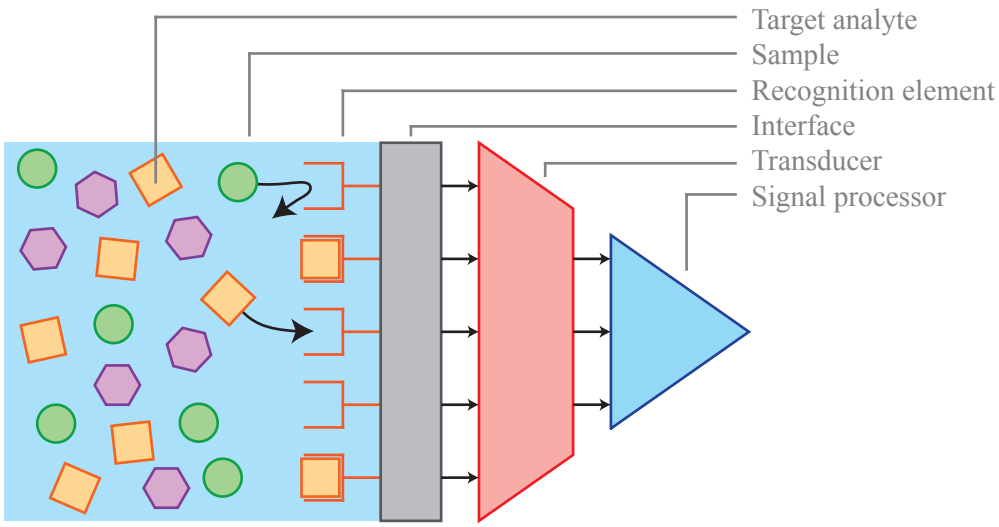


Figure 2.1: Schematic of a biosensor structure showing elements common to many biosensors. The target analyte must be specifically recognised in a complex sample by a recognition element immobilised on an interface. Capture of the target should invoke a change in the transducer, which is then sent to the signal processor.

Biosensors varies greatly in complexity and functionality. The two most well-known are probably the home pregnancy test and blood sugar measurer (glucometer) for diabetes patients. Even though they are both major successes within the healthcare industry, they rely on completely different sensing mechanisms. The modern home pregnancy test is a lateral flow device (Figure 2.2), which relies on capillary flow of a liquid sample through a filter. During the flow it dissolves dried antibodies immobilised on gold nanoparticles, which mixes with the sample. If the sample is positive the antibodies will capture a particular hormone (human chorionic gonadotropin (hCG)) only present in pregnant women. Further downstream are two rows of new antibodies. The first row captures the target molecule in a different binding pocket than the nanoparticle antibodies. The second (control) row binds specifically to the nanoparticle antibodies, making sure that the test worked as intended. Once a row binds the nanoparticles a visible line is seen. This type of sensor works well for qualitative yes/no sensors.

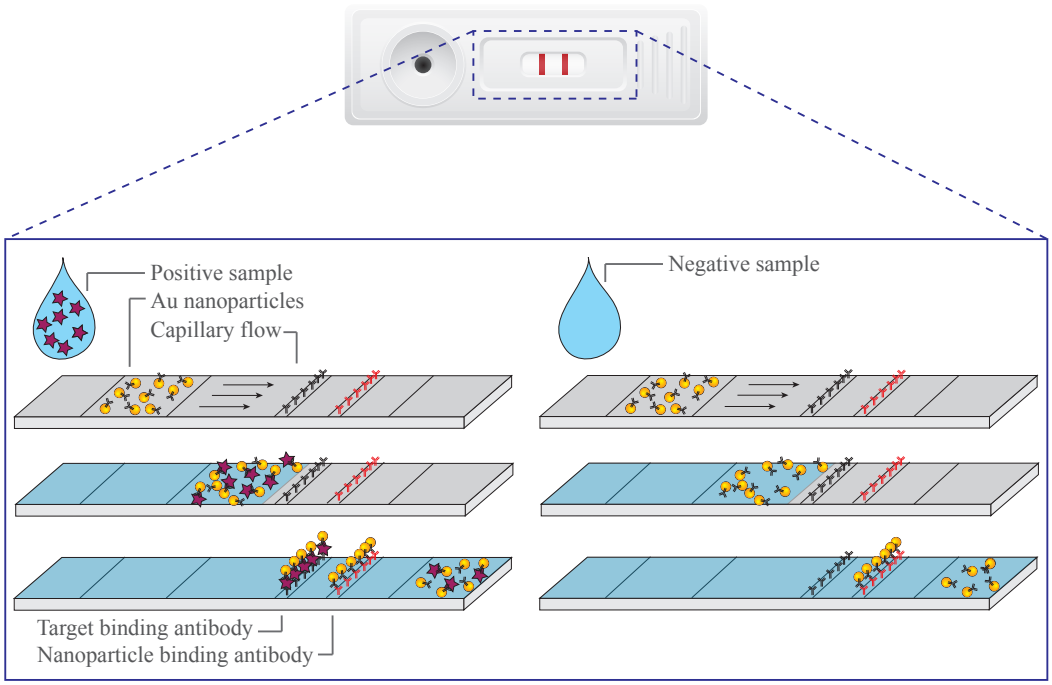


Figure 2.2: Schematic of lateral flow device showing how it is build up. Usually the sample flows in a filter at a given speed in capillary flow. It reaches several different dried components, which aid in signal enhancement. At first the sample reaches dried gold nanoparticles coated with specific antibodies. These antibodies binds to the target in the sample, which is analysed by two rows of immobilsed antibodies. The first row acts as the test row, which binds specifically to the target, whereas the second (control) row binds specifically to the nanoparticles as a positive control. The agglomeration of nanoparticles yields a visible line on the sensor.

The glucometer is a quantitative electrochemical sensor [15] that utilizes enzymes to generate a current between electrodes. The sensor consists of a single-use test strip and a readout unit. The test strip usually contains all necessary components for electrochemical detection, and the readout unit contains electronic connections and signal analysis. Once the sample reaches an immobilized enzyme (normally glucose oxidase) in the test strip it generates electrons that can be measured by the electrodes. By comparing the amount of current generated with an internal calibration, the readout unit can give a quantitative answer on a small display. Since diabetes patients need to monitor their glucose level several times a day, it is important that the sensor is compact and easy to use.

These two commercial examples of molecular sensors reveal very different technologies. One general difference is the use of a label (gold nanoparticle) in the home pregnancy test to visualize if the sample is positive or not. Whereas the glucometer is label-free, in that it directly measures a chemical reaction

happening due to the interaction of glucose with the enzyme.

All molecular sensors can be divided into these two groups. The (often) cheapest and most elegant solution is the label-free version, since there is no need for additional components in the sensor. However not all molecules are suited for label-free sensing as the sensitivity, accuracy and precision of the sensor can be greatly enhanced by using labels. In the case of the home pregnancy test the positive line would simply not be visible if the gold nanoparticles were removed from the sensor. Whereas in the glucometer case adding additional labels to glucose in the sample would not enhance the enzymatic reaction - in fact it would probably hinder it. It is therefore often a trade-off between complexity and functionality that determines if a sensor will be label-free or not.

New opportunities within biosensors have been created by the modern development of smartphones and other 'smart' devices. These devices are increasingly becoming an integrated part of billions of people's daily life. By utilizing the built-in electrical connectors it is possible to design sensor devices and software that communicate with the smart device. This means that companies do not need to develop complicated hardware for their readout units, as long as they design the sensors to match the smart device electrical input. This also eliminates the need for the user to carry extra equipment, which makes a product more desirable. Several companies are pursuing these opportunities within the areas of e.g. temperature sensing, blood pressure monitoring, heart rate monitoring, breath analysis, air quality monitoring and gas sensing.

## 2.3 Molecular interactions

In order to make biosensors selective towards a specific target a recognition element must be immobilised on the surface of the sensor. There are several ways of accomplishing this depending on the surface material and target type. Molecular interactions rely on chemical reactions and physical forces. Chemical reactions are often stronger and more selective than physical forces, but they can be harder to control. The following describes different molecular forces in brief, which all contribute to immobilization of recognition molecules to a surface. This serves as background information to the discussion of antibodies and aptamers given later. Lastly, current published aptasensors for 17$\beta$-estradiol detection is discussed.

### 2.3.1 Molecular forces

#### Chemical bonds

The covalent bond is the most classical chemical bond; atoms bind to each other by sharing electrons. Some atoms have a few excess electrons in their outer shell, which can be accepted by other atoms that are missing electrons. This gives rise to a strong bond where atoms involved in the bond have their electronic configuration satisfied. In the case of water, oxygen is capable of accepting two electrons. The covalent bond is the strongest of the chemical bonds which makes it desirable for immobilization purposes.

The co-ordinate bond is a special type of covalent bond where both electrons come from the same atom. It is also known as a dative covalent or covalent-like bond. This type of bond is particularly interesting for SERS purposes as silver or gold nanoparticles are often used, which excibits very low chemical reactivity. However atoms like sulphur and nitrogen can form a covalent-like or co-ordinate bond to both gold and silver [12, 16, 17]. By modifying the recognition element with a suitable functional group, it is possible to form a strong bond to the surface.

#### Electrostatic force

When two point charges are brought in close proximity they exhibit a force upon each other. This interaction is described in the Coulomb law, which also states that the force is inversely proportional to the square distance between the charges [18]. Molecules or nanoparticles can have a fixed charge distribution ($\delta$), which makes one part more or less charged than the other; hence a dipole is created. When suspended in solution dipoles can freely rotate to orient themselves towards other dipoles as shown in Figure 2.3. The dipoles will through electrostatic forces align with other dipoles until a stable state is reached.

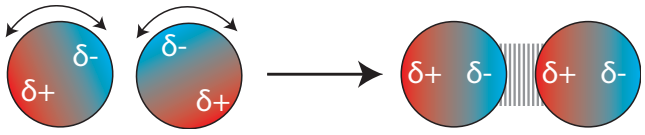


Figure 2.3: Schematic of electrostatic dipole interactions. When a dipole is achieved in a substance with a charge distribution $\delta$ and brought in close proximity of another dipole they interact. Positive charges will attract negative charges by re-orienting the substance accordingly.

### Electrostatic screening of charges

Consider a charged surface in a fluid containing ions. The surface will immediately attract oppositely charged ions, which will create a layer surrounding it. Depending on the strength of the charged surface it might still be capable of attracting more ions than one single layer as shown in Figure 2.4; this is called an electrical double layer [19]. At some distance the electrical field from the surface will be completely screened off by the ions making it essentially invisible to other charged species. This length scale on which charges interact is called the Debye length ($\lambda_D$) after the Dutch physicist Peter Debye, given by:

$$\lambda_D = \sqrt{\frac{\epsilon k_B T}{2(Ze)^2 c_0}}, \tag{2.1}$$

where $\epsilon$ is the permittivity of the fluid, $k_B$ is Boltzmann's constant, $T$ is the temperature, $Z$ is the valence number, $e$ is the elementary charge and $c_0$ is the concentration of the ions. From this expression it is seen that controlling the temperature and concentration of ions in the fluid plays a vital role in screening of electrical charges on molecules of interest.

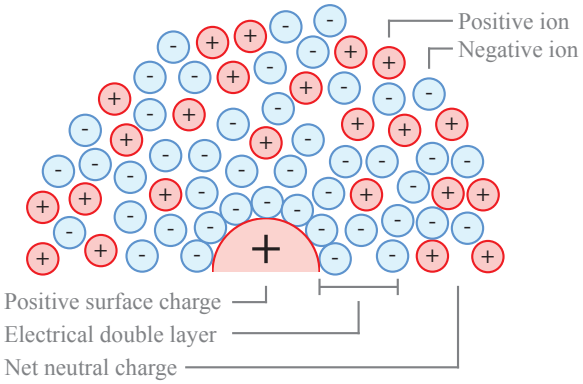


Figure 2.4: Close to a charged surface in liquid there will be electrostatic screening. The surface (here positive) will attract counter-ions (here negative) from the solution in order to screen off the electric field. At a distance away from the surface the charge is essentially invisible to other similarly charged species.

### Hydrogen bond

The hydrogen bond is a specially strong electrostatic attraction force involving hydrogen and electronegative atoms such as nitrogen, oxygen and fluorine. Figure 2.5 shows the phenomenon between water molecules, where the electronegativity of oxygen (red) leaves the hydrogen atoms (white) positively

charged. The electrostatic attraction between two water molecules is very strong due to the small size of hydrogen. Hydrogen bonds are weak compared to covalent bonds, but strong enough to have significant implications in many areas ranging from the relatively high boiling point of water to binding of DNA strands to form a double helix structure.

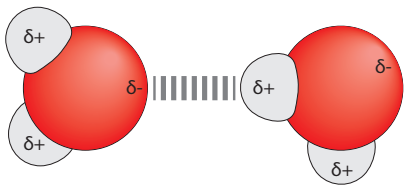


Figure 2.5: Schematic of the hydrogen bond between oxygen and hydrogen in water. The small size of hydrogen makes the electrostatic interaction with negative charges particularly strong.

### Hydrophobic force

Non-polar substances are immiscible with water due to hydrogen bonds between water molecules. Phospholipids consisting of a polar head group with a non-polar tail will rearrange themselves to shield off the non-polar region when mixed with water. This is shown in Figure 2.6. This rearrangement of molecules minimises the energy of the system by forming structures of different shapes (here shown as a sphere) based on the chemical structure or physical size of the molecules. This type of force has been observed in e.g. antibody-antigen binding as well as in the formation of lipid membranes and vesicles.

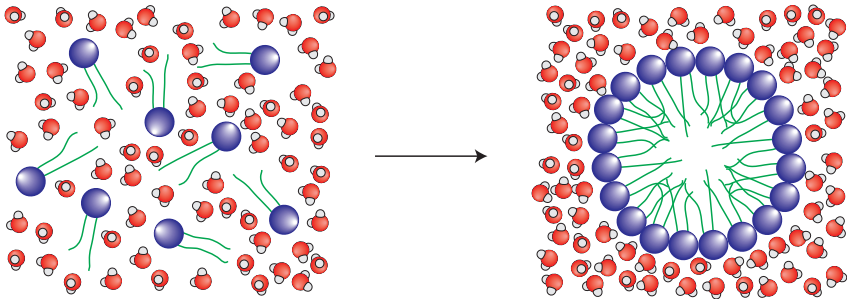

Figure 2.6: Hydrophobic forces shield the hydrophobic tail of lipids by forcing them together in groups. This group rearranges itself to a shape which requires the least energy (here a sphere). Other shapes and sizes can arise from this self-assembly depending on parameters such as tail length, head size and concentration of lipids.

## 2.4 Recognition elements

### Antibodies

The classical type of recognition element used in biosensors is a class of proteins called antibodies. They are produced by the reaction of the immune system to foreign bodies in the blood. Antibodies specifically bind to the foreign body in order to neutralise it by e.g. hindering proper function and vitality of the specie. Antibodies used are often a type of immunoglobulin G (IgG) consisting of two short (light) and two long (heavy) polypeptide (amino acid) chains linked by disulphide bonds. Figure 2.7 shows the characteristic Y-shape of IgG's, where only the tip of the two arms are involved in target binding. These arms are highly flexible in order to encompass for the unknown structure of intruding species. The antibodies are produced in the lymphocytes before the intruder has even entered the body. By producing a huge library (100+ million [20]) of different antibodies the human body is ready to handle most threats immediately.

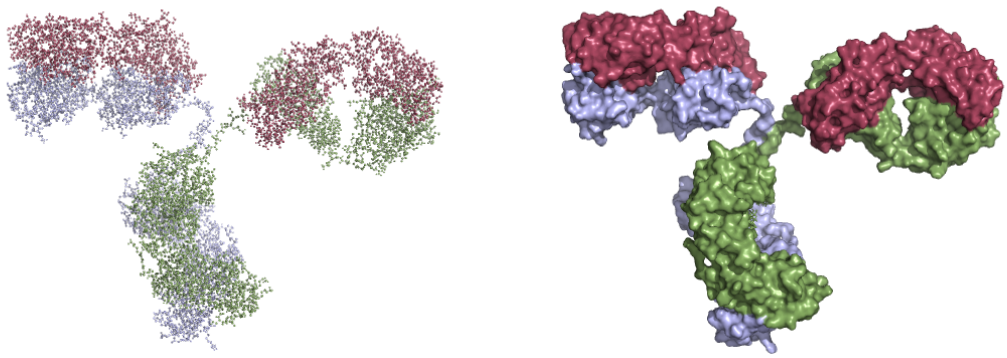

Figure 2.7: Molecular structure of an antibody (IgG). The two red chains on the flexible arms of the structure are involved in target binding. PDB database entry: 1IGT.

Assays based on antibodies as the recognition element are termed immunoassays. They are widespread within diagnostics and therapeutics, where they among others detect surface proteins of cancer cells or stimulate a specific reaction of the immune system. However antibodies are very hard to produce artificially. The normal procedure is to inject antigens into laboratory animals, in order to produce large amounts of antigen-specific antibodies [21]. Antigens are molecules able to invoke a reaction from the immune system. The antibodies can then be recovered from the animal and purified for further use. There is currently no easy way to artificially produce antibodies due to its large and complicated structure.

### DNA aptamers

In 1990 three groups independently reported on single stranded nucleic acid sequences that selectively bind non-nucleic acid targets with high affinity [22–24]. Based on *in vitro* selection and amplification it was possible to select sequences from a vast library of nucleic acids. This technique was named 'systematic evolution of ligands by exponential enrichment' (SELEX) and the resulting oligonucleotides were termed 'aptamers' derived from the latin word *aptus* meaning 'to fit'. Aptamers can be either RNA or DNA depending on their targets and desired function, however RNA has a generic short lifetime in biological fluids due to nucleases, making them unsuitable for certain applications. During the SELEX process short primers (15-30 bases long) are often flanking the varying aptamer sequence since the process involves a polymerase chain reaction (PCR) amplification step of the aptamer during selection. This is an issue since aptamer binding affinity is generally better for shorter sequences [25]. These primers are however hard to avoid, since they might aid in structural support of the aptamer or even be part of the binding motif [26].

Since its discovery, aptamers have gained significant attention as a potential replacement for antibodies. It is desirable since aptamers can be synthesised very easily and cheap without the use of animals. Aptamers can be modified with a broad range of either labelling molecules or functional groups for surface immobilization purposes, without hindering the binding affinity towards the target. Since aptamers are single-stranded oligonucleotides it is often desirable to covalently modify one end of the strand to avoid any implications on the binding affinity.

The most studied aptamer is the thrombin binding aptamer (TBA) selected by Bock et al. in 1992 [27] consisting of only guanine and thymine bases. Thrombin is an enzyme involved in blood coagulation and plays a role in diseases related to blood clots. TBA is very short consisting of only 15 bases making it easy to model. A lot of work has been put into understanding the complex binding mechanism of aptamers and here TBA has often been used as the model. X-ray crystallography and nuclear magnetic resonance (NMR) investigations have revealed a secondary and tertiary structure of the aptamer in the form of a chair-like structure [28, 29] (shown in Figure 2.8). Generally an aptamer folds upon itself by forming intra-strand base pairing. In the case of TBA the structure is supported by hydrogen bonds between neighbouring guanine bases, which can be stabilized by potassium ions [29]. TBA has been shown to bind to thrombin at the so-called 'exosite I' through hydrophobic interactions. A second 29-mer aptamer towards thrombin (named HD22) was published in 1997 [30] and was shown to bind to a different site (exosite II) of thrombin. This has been widely used in conjunction with TBA to form sandwich assays for diagnostic purposes.

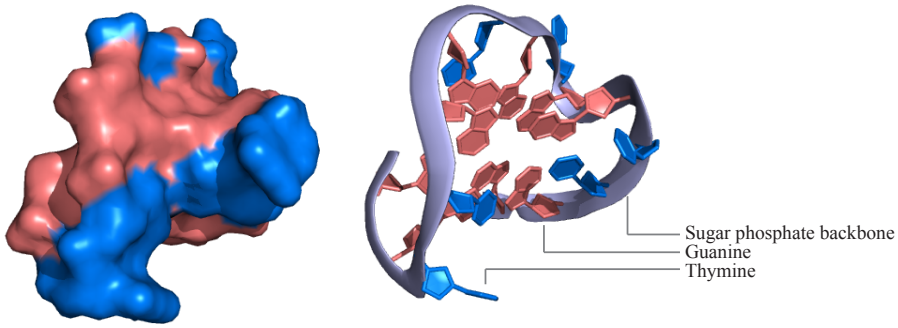


Figure 2.8: Molecular structure of thrombin binding aptamer. The single stranded DNA fold upon itself by forming internal base pairs. The chair-like structure is seen, which is essential for TBA to properly bind thrombin. PDB database entry: 4DII.

The intensive study of thrombin binding aptamers have led to selection of aptamers towards many different targets ranging from small molecules [10, 31, 32] to even whole cells [33]. A variety of different molecular sensors based on aptamers (so-called aptasensors) [34] have been employed to detect these targets, with reported limit of detection being at the femtomolar level.

### 2.4.1 Aptasensors for 17$\beta$-estradiol detection

Detection of 17$\beta$-estradiol using aptamers have been demonstrated on many sensor systems the past 8 years. The first report of a 17$\beta$-estradiol specific aptamer was published in 2007 [10], which enabled research groups to develop molecular sensors. Especially electrochemical detection have been utilised to demonstrate the capability of a selective 17$\beta$-estradiol biosensor [10, 35–38], but also optical [31, 39] and colorimetric [25] biosensors have been reported. These biosensors demonstrate the growing interest in detecting 17$\beta$-estradiol and other pharmaceuticals. To this date no information of a SERS biosensor for 17$\beta$-estradiol has been published. SERS has the potential to surpass the detection limit of all of the aforementioned biosensors, as single molecule detection is theoretically possible.

## 2.5 Surface enhanced Raman spectroscopy

In this project a surface enhanced Raman spectroscopy (SERS) sensor is applied for sensitive detection of 17$\beta$-estradiol. Raman spectroscopy is a vibrational technique that relies on the interaction of incoming light with matter by measuring the reflected light. Changes in reflected wavelengths reveal molecular information about the substance. Molecular bonds interacts with the in-

coming photon by either dampening or enhancing it. By this method it is possible to 'fingerprint' molecules by providing a unique spectrum for each molecule due to the abundance of different molecular bonds present in molecules. However Raman scattering is a very rare effect (i.e. it has a small cross section ($10^{-30}$-$10^{-27}$ cm$^2$) [40]), which requires highly concentrated samples [41] making it inferior to traditional fluorescence spectroscopy (cross section $10^{-16}$ cm$^2$ [42]). Raman and fluorescence spectroscopy share some commonalities in that they interact light, but for Raman scattering this happens instantaneously compared to nanosecond delays betweem absorption and emission in fluorescence caused by a cascade of relaxation events. Figure 2.9 schematically shows both phenomena using energy level diagrams. In fluorescence spectroscopy the incident wave is absorbed by the molecule bringing the molecule from a ground state to an excited state. By internal relaxation the molecule is eventually returned to the ground state by emission of a photon with slightly less energy (longer wavelength) than the incident wave [42]. In Raman scattering the incident light inelastically scatter with vibrations (phonons) or other excitations in the molecule. The molecule gets excited to a virtual energy state and instantly relaxes. The relaxed state can be of either lower or higher energy than the original state, which in turn releases a photon with higher (anti-Stokes) or lower (Stokes) energy respectively. Since these are rare events most of the reflected light will have the same wavelength as the incoming light - this is termed Rayleigh scattering. Raman spectroscopy is often compared to infrared (IR) spectroscopy, since both yield chemical information of a molecule as IR spectroscopy relies on absorption of light at different wavelengths in the IR range. In many ways IR and Raman spectroscopy are complementary techniques in that molecules might either be IR or Raman active. However in this project only Raman spectroscopy was used.

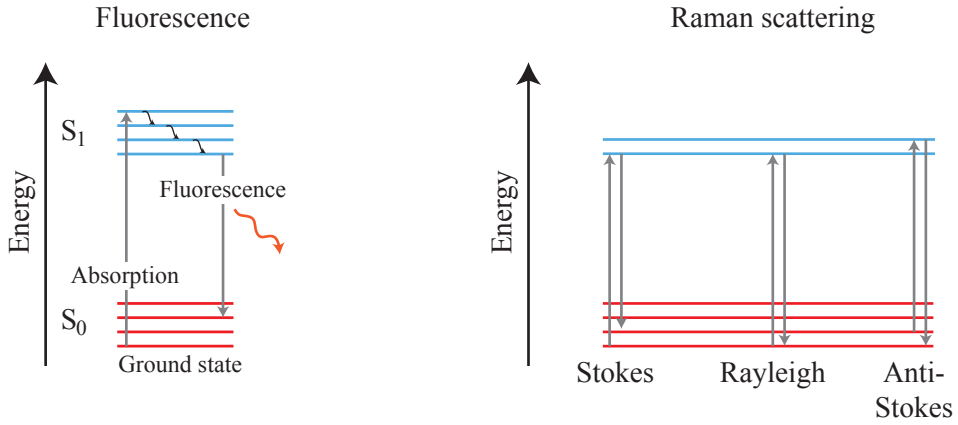


Figure 2.9: Energy diagrams for fluorescence and Raman scattering. In fluorescence an electron absorbs a photon bringing it to an excited state. Here it undergoes internal scattering effects losing energy and is eventually returned to the ground state by emission of a photon with slightly less energy than the original photon. In Raman scattering the photon interacts with vibrations (phonons) in the molecule. The molecule gets excited to a virtual energy state before it instantly relaxes. The relaxed state can be of either identical (Rayleigh scattering), lower (Stokes scattering) or higher (anti-Stokes) energy.

### 2.5.1 SERS phenomenon

By locally enhancing the electric field it is possible to compensate for the low cross section of Raman scattering. High enhancements are needed to succumb for the orders of magnitudes required for Raman scattering to reach the sensitivity of fluorescence. By only increasing the energy of the incident light the molecule would simply be destroyed. SERS is one way of locally enhancing electric fields in so-called 'hot spots'. It was first discovered in 1974 by Fleischmann et al. [43] measuring enhanced Raman signals on roughened silver surfaces. By trapping a portion of the incoming light, metal is capable of supporting oscillations of electrons at the interface to a dielectric (e.g. air). This is known as surface plasmons as shown in Figure 2.10. The localised surface plasmon depends heavily on the size, geometry and composition of the metal, which is why metal nanoparticles are often used [12]. The motion of the electrons creates an electric field outside (and inside) the particle, which can couple with another particle in close vicinity.

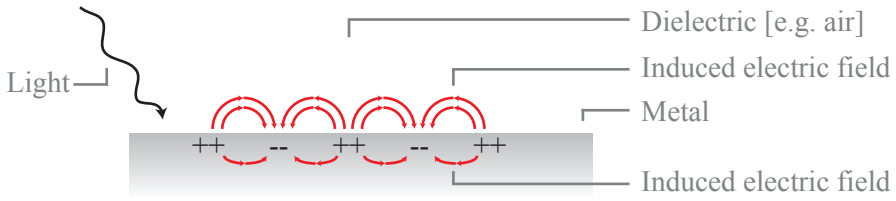


Figure 2.10: Schematic of surface plasmon generation. Surface plasmons can be generated at the interface between a metal and a dielectric by excitation with light.

Figure 2.11 shows how two nanoparticles can create high local enhancement of an electric field. Typically silver and gold have been used for nanoparticle material. Silver has the highest electrical field enhancement capability due to its favourable dielectric function [11], but gold is more chemically stable and not prone to oxidation. By using silver nanoparticles Kneipp et al. [44] and Nie and Emory [45] both reported in 1997 about single molecule (SM) SERS detection, proving the potential of SERS in molecular detection. Nevertheless both silver and gold have been extensively used in nanoparticle fabrication for SERS measurement. A vast selection of different sizes and shapes can be found in literature, e.g. cubes, spheres, rods, stars, tetrahedra and nanoshells [11].

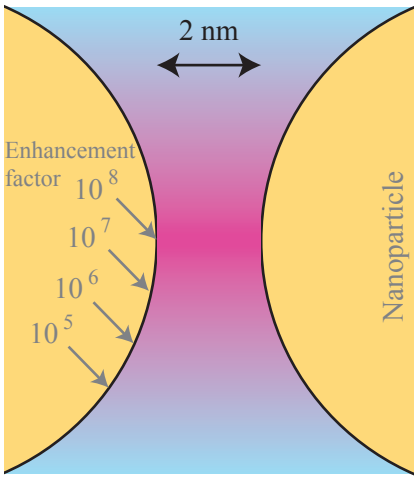


Figure 2.11: Schematic of SERS enhancement factors. In small gaps between metal surfaces strong electromagnetic fields can be generated by surface plasmons. By trapping molecules in these gaps it is possible to observe strong enhancement of Raman signals. Adapted from [12]

Another contributing factor to the enhancement of Raman signals in SERS is assigned to the 'chemical effect'. This relates to polarizability and thereby orientation of the molecule to be detected. Depending on how the molecule interacts with the nanoparticle surface, it might orient in a favourable configuration [12]. Several anions have likewise been reported to yield chemical enhancement of different molecules, likely owing to creation of surface active sites on the nanoparticle [46] and change in surface orientation/polarizability [47]. The enhancement factors found by 'chemical effects' are on the order of $10^2$, which is much lower than electromagnetical enhancement which is on the order of $10^8$-$10^{14}$ [40, 45]. The actual mechanism for chemical enhancement is still being debated [48, 49].

### 2.5.2 Nanoparticles and 2D SERS substrates

In order to achieve strong local electrical field enhancements it is necessary to form clusters of nanoparticles. This is most commonly facilitated by aggregation in solution followed by drying the solution on a solid support as shown in Figure 2.12. Aggregation can be achieved by either chemical forces (molecular linkers), physical forces (hydrophobicity/hydrophilicity, magnetism, electrostatic interactions, etc.) or a combination (e.g. enhanced binding due to magnetic aggregation or electrostatic attraction [50]). However the stability of the nanoparticles in solution is highly dependent on several factors such as ionic strength, pH and temperature. Hydrodynamic forces during drying can also be a contributing factor to the cluster size and shape.

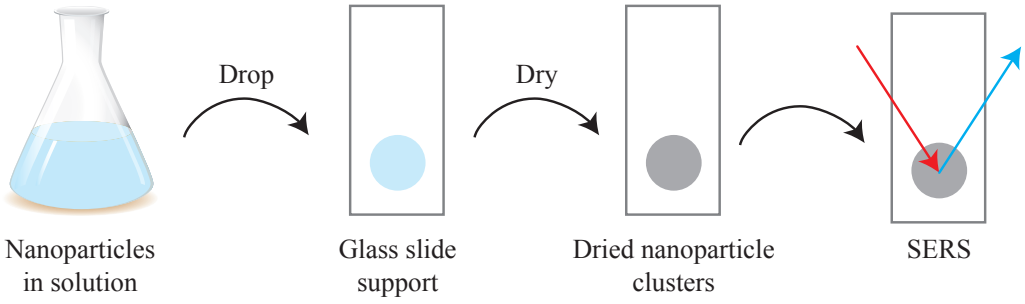


Figure 2.12: A drop of nanoparticles in solution can be applied to a solid support (like a glass slide) and dried to form hot spots. By capturing a target analyte on the nanoparticles in solution it is possible to create a molecular sensor.

.

One major drawback of nanoparticle SERS is the poor reproducibility of hot spots. Even though nanoparticles can be created with extreme precision on the nanometer scale, chemical stability in solution is an issue and the aggregation process remains random. The latter results in difficulties finding hot spots on the solid support making the detection very labour intensive.

These obstacles have been tackled by many researcher resorting to nanoscale fabrication in cleanroom facilities well-known from the electronics industry. By engineering structures at the nanoscale it is possible to achieve well defined 2D arrays, where the electrical field enhancement can be optimised. Most commonly used is lithography where layers of deposited material is removed in selected patterns using illumination of UV light onto photosensitive polymer. However to overcome the limit of diffraction electron beam (E-beam) lithography has been used to make highly enhancing substrates [51, 52], but this technique is only suitable for research purposes due to its very high costs and slow production speed. Therefore a lot of effort have been put into making highly performing SERS substrates at low cost [11, 53]. Most substrates are based on immobilization of nanoparticles on various solid supports [53, 54]. However some substrates are based on etching of a substrate to make it rough, followed by a metal deposition [6]. A sample can then be dried on the surface, where the nanostructures will create uniform enhancements in a 2D array. This is schematically shown in Figure 2.13.

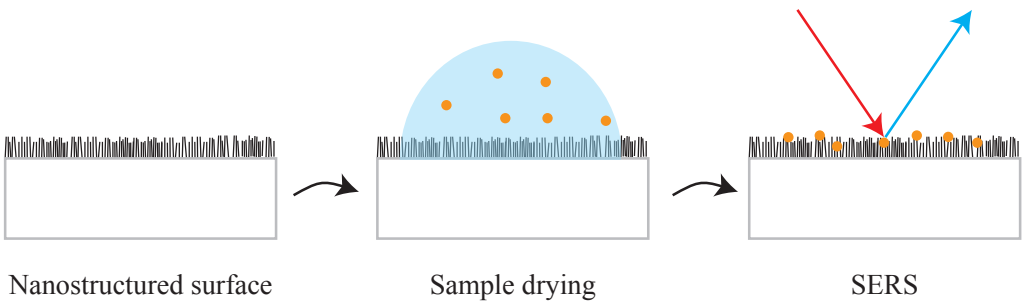


Figure 2.13: By fabricating nanostructures (either ordered or random) in metal it is possible to achieve very high electromagnetic enhancement factors. By drying a sample onto the substrate molecular SERS sensors can be achieved.

### 2.5.3 Statistics in SERS

The SERS effect has been intensively studied and many theories have been discussed. When Kneipp et al. [44] and Nie and Emory [45] independently reported on SM-SERS in 1997 it was believed that there was an underlying Poissonian distribution of SERS intensities, due to the assumption that a hot spot contained either zero or one molecule at very low concentration. This

was presumably supported by measurements of 100 SERS spectra by Kneipp et al. [44], which showed three peaks of SERS intensities attributed to measuring one, two or three molecules respectively. However ten years later Etchegoin et al. [40] demonstrated that the peaks arising from these measurements were probably due to insufficient sampling size. In fact the assumption of a Poissonian distribution of SERS intensities was challenged, and it is no longer believed to be valid. Instead it has been experimentally demonstrated [55] that SERS intensities follow long/heavy tailed distributions (e.g. Pareto). This is due to the strong localisation of the electromagnetic enhancement factor on metal surfaces in close proximity; a minute displacement of 1 nm can give a vastly different intensity making SM-SERS troublesome. The same group of scientists also investigated SM-SERS using a bi-analyte technique (BiASERS) [50]. By super position of spectral data they showed that SM signals can be detected in BiASERS for even relatively large analyte concentration not relying on 'rare events'. These observations, including heavy tailed intensity distributions, have been widely supported when studying ensemble (non-SM) SERS [56, 57].

Even though SERS should be considered a statistical tool most groups are currently still reporting SERS biosensor detection limits based on only few ($n < 10$) measurement points. These types of measurements are certainly valuable in the sense of qualitative yes/no sensors, as the mere presence of target molecule is an indication of proper sensor function. However as demonstrated by the aforementioned work of Etchegoin et al. it is statistically insignificant to report quantitative detection based on these few measurements. The inherent problem probably relates to the lack of formed hot spots in nanoparticle clusters. Since these are randomly created on solid supports it can be challenging to find sufficient spots to acquire data from, which leads to poor statistics and unreliable results.

The development of 2D SERS substrates helps to overcome this obstacle as hot spots can be created uniformly on large areas [6]. Using these substrates it is possible to obtain large amounts of data in an easy way by letting the Raman instrument perform so-called area mappings/scans. Utilizing an automated stage the instrument can map large areas with micrometer resolution obtaining SERS spectra in every single point. This was demonstrated in previous work within our group [57]. Using proper statistical analysis on these data sets can ultimately lead to quantitative SERS biosensors.

# 3 Methods

This project mainly concerned the development of a SERS aptasensor for 17$\beta$-estradiol detection (Track 2). Only one minor experimental study was carried out in relation to Track 1 - it will be described in full in the next chapter. This chapter describes the methods related to SERS substrate fabrication and the chosen chemical functionalisation strategy. A list of chemicals can be found in Appendix A.1.

## 3.1 SERS substrate fabrication

SERS substrates with uniform nanopillar distribution at wafer scale were continously fabricated in the cleanroom facility at DTU Danchip throughout the project. Both silver and gold covered nanopillars were investigated as they both showed excellent enhancement of Raman signals. In order to develop a SERS aptasensor a chemical functionalisation strategy was developed to accomodate both metals. All batches of SERS substrates were fabricated following the same recipe [6] - the procedure is sketched in Figure 3.1. Silicon nanopillars were created in a reactive ion etch (RIE) (STS ICP Advanced Silicon Etcher, SPTS Technologies) using $SF_6$ and $O_2$ in combination to randomly etch an un-masked silicon wafer (4", <100>, boron doped). The etch is both chemical and physical as the reactive $SF_6/O_2$ gas is accelerated towards the surface by an electric field. Using this mixture it is possible to create high aspect ratio structures on the micro and nanometer scale [58, 59]. Depending on the etching time the height of the nanopillars can be controlled. In this project 4 min etching time was used as a standard, which created roughly 500 nm tall silicon pillars. At this height it was seen that a metal (gold or silver) layer of 200-225 nm yielded excellent and reproducible SERS signals. The nanopillars were uniformly formed on most of the 4" wafer. A minor variation was observed in SERS intensity across the wafer, but this was deemed insignificant. The outermost 1-2 cm rim of the wafer formed no nanopillars and was discarded.

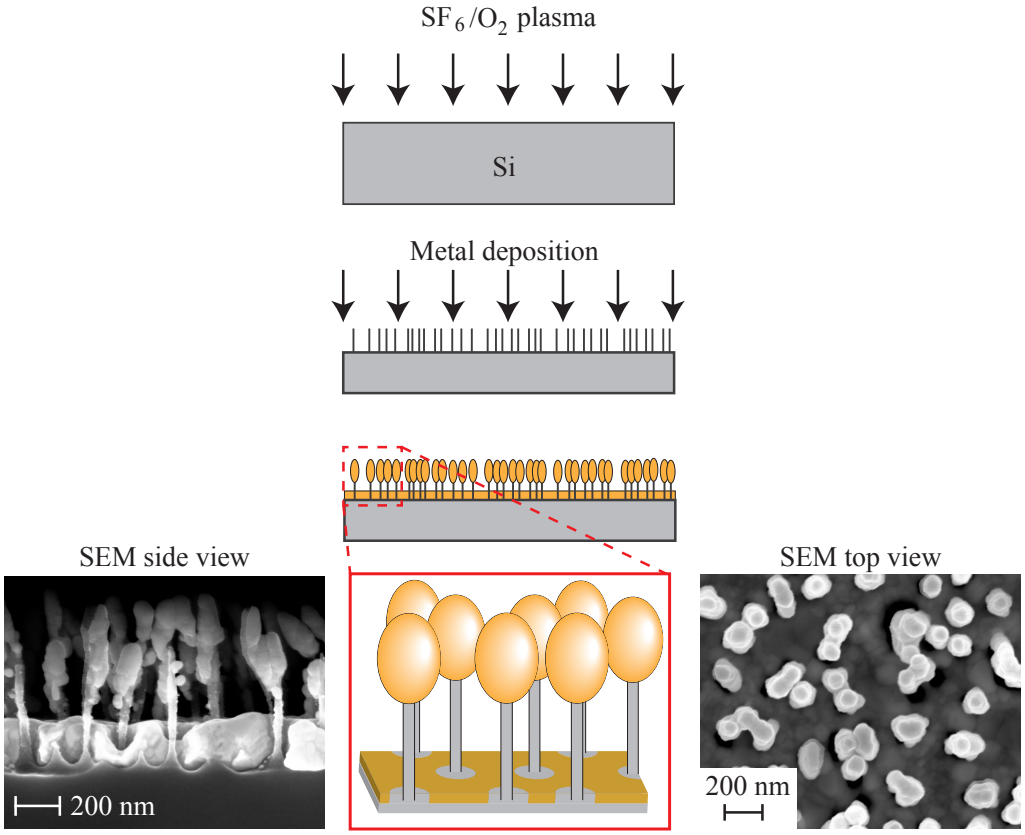


Figure 3.1: Schematic of the SERS fabrication process. An $SF_6/O_2$ plasma is accelerated towards the un-masked silicon surface. This yields a chemical and physical etch of the silicon forming free-standing nanopillars. The height and surface coverage can be controlled in the fabrication process, but it remains to fabricate randomnly positioned nanopillars. By E-beam evaporation of metal the nanopillars can recieve a metal capping. This is shown on the Scanning Electron Microscopy (SEM) inserts (left: side view, right: top view).

After etching (before metal deposition) a one minute cleaning procedure in $O_2$ plasma was performed in order to remove excess fluorine and sulphur species still present on the silicon surface. This was to suppress any background signal before metal deposition. E-beam evaporation (Alcatel SCM 600) was used for metal deposition due to its unidirectional deposition [60]. Approximately 200 nm of gold or 225 nm of silver was deposited on the 500 nm tall pillars. This ensures that metal being deposited on the top of the pillar is electrically isolated from the metal film forming at the bottom on the silicon substrate. This is also seen in the SEM pictures inserted in Figure 3.1. The electric isolation is important since localised plasmon resonances are formed at the border between the metal cap and the silicon nanopillar [61]. Hot spots between

nanopillars are created when liquid is applied to the surface and left to dry. The hydrodynamic forces of the drying droplet pull the nanopillars towards each other to create larger clusters. This effect is clearly seen in Figure 3.2 where the uniformity of the etching process is also visible. It should be noted that minor clusters of nanopillars are inherently created during the random etching process. These clusters also aid in hot spot formation as well as the metal film on the bottom of the nanopillars.

This type of fabrication method for SERS substrates[1] has several advantages compared to other methods as listed in Table 3.1. It is capable of forming uniformly distributed hot spots at wafer scale, without requiring complicated process steps involving lithographic masks or expensive tools such as E-beam writers. The degree of control over the structures is however limited compared to lithopgraphy due to the random nature of the un-masked RIE.

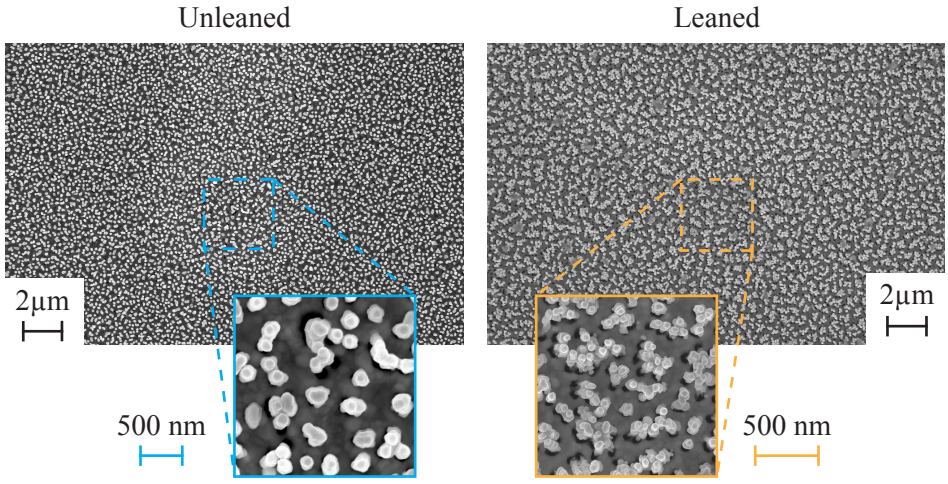


Figure 3.2: SEM images of large scale nanopillar fabrication. Leaned nanopillars (right) are seen to cluster compared to unleaned nanopillars (left). The leaning facilitate local hot spots between neighbouring nanopillars, where strong enhancement of the electromagnetic field can be achieved.

Optimisation of the SERS substrate has been thoroughly described by other members of the group [6, 61, 62]. Briefly, they tested different metal thicknesses in combination with varying etching times in order to optimise SERS enhancement. It was also tested whether the background signal could be further suppressed using various methods such as 'post etch' heating and 'post metal deposition' heating [62]. Even though some improvement was obtained it was not deemed reproducible and therefore this strategy was not pursued in this project.

[1]These substrates have been made commercially available through DTU Nanotech start-up company SILMECO.

Table 3.1: Comparison of different SERS substrate fabrication methods.

| Method | Uniformity | Control of hot spots | Fabrication speed | Cost |
|---|---|---|---|---|
| Nanoparticle | Few clusters | Low | Quick | Cheap |
| Mask-less RIE | Wafer scale | Medium | Very quick | Cheap |
| UV lithography | Wafer scale | High | Slow | Costly |
| E-beam lithography | Extreme* | Extreme | Very slow | Expensive |

*In $\mu m^2$ areas.

### 3.1.1 Batch information

Several batches of SERS substrates were fabricated throughout the project whenever deemed necessary. Even though silver oxidises at ambient pressures the SERS acitivity of silver covered nanopillars remained very satisfactory after 3 months storage. This duration of storage was also seen not to affect SERS intensity of gold covered nanopillars significantly. No substrates were used past 4 month storage. Table 3.2 shows information about the SERS substrate batches fabricated throughout the project. All batches were etched for four minutes and $O_2$ plasma treated for one minute before metal deposition unless otherwise stated. After fabrication the wafers were diced into smaller pieces for easy handling.

Table 3.2: Information about all batches of SERS substrates fabricated throughout the project. The reproducibility of the substrates was excellent for both silver and gold coated nanopillars.

| Batch | Etching | Metal deposition | Metal type | Metal thickness | Comment |
|---|---|---|---|---|---|
| KF1 | 25-09-2013 | 27-09-2013 | Au | 200 nm | No pre-metal $O_2$ clean |
| KF2-1 | 29-10-2013 | 29-10-2013 | Ag | 250 nm | No pre-metal $O_2$ clean |
| KF2-2 | 29-10-2013 | 29-10-2013 | Ag | 190 nm | 2 min etch. No pre-metal $O_2$ clean |
| KF3-1 | 12-12-2013 | 17-12-2013 | Ag | 225 nm | |
| KF3-2 | 12-12-2013 | 17-12-2013 | Ag | 225 nm | |
| KF4-1 | 27-01-2014 | 28-01-2014 | Ag | 225 nm | Columbia University |
| KF4-2 | 27-01-2014 | 28-01-2014 | Ag | 225 nm | Columbia University |
| KF5-1 | 10-06-2014 | 10-06-2014 | Au | 200 nm | |
| KF5-2 | 10-06-2014 | 12-06-2014 | Ag | 220 nm | |
| KF5-3 | 10-06-2014 | 10-06-2014 | Au | 200 nm | 3 min etch |
| KF5-4 | 10-06-2014 | 12-06-2014 | Ag | 160 nm | 3 min etch |
| KF6-1 | 17-09-2014 | 18-09-2014 | Au | 200 nm | |
| KF6-2 | 17-09-2014 | 18-09-2014 | Au | 200 nm | |
| KF6-3 | 17-09-2014 | 18-09-2014 | Au | 200 nm | |
| KF7-1 | 12-01-2015 | 12-01-2015 | Au | 200 nm | |
| KF7-2 | 12-01-2015 | 12-01-2015 | Au | 200 nm | |
| KF8-1 | 06-05-2015 | 06-05-2015 | Au | 200 nm | |
| KF8-2 | 06-05-2015 | 06-05-2015 | Au | 200 nm | |

## 3.2 Chemical functionalisation

Since both gold and silver coated substrates were fabricated it was necessary to develop selective surface chemistry targetting both of these materials. For this thiol chemistry was chosen due to sulphurs capability of forming covalent-like bonds to both: the bond strength to gold is roughly twice as strong compared to silver [63]. Generally the performance of the silver substrates were slightly better compared to gold, but issues relating to the functionalisation procedure (explained later) made it necessary to switch to gold substrates as seen from batch KF6-1 onwards. Figure 3.3 shows a schematic of the functionalisation strategy. Firstly the aptamer is physically adsorbed onto the cleaned metal nanopillar surface (a,b). Further incubation allows a covalent-like bond to be formed between the metal surface and the aptamer (c), which is the rate-limiting step. Blocking the remaining binding sites by small molecule 6-mercapto-1-hexanol (MCH) (d) prevents both unspecific binding of non-DNA molecules and the DNA phosphate backbone, which lifts the aptamer from the metal surface ensuring complete functionality [16]. Self-assembled monolayers (SAMs) are quickly formed by MCH. By proper folding of the aptamer it is possible to obtain selective aptamer-target binding (e).

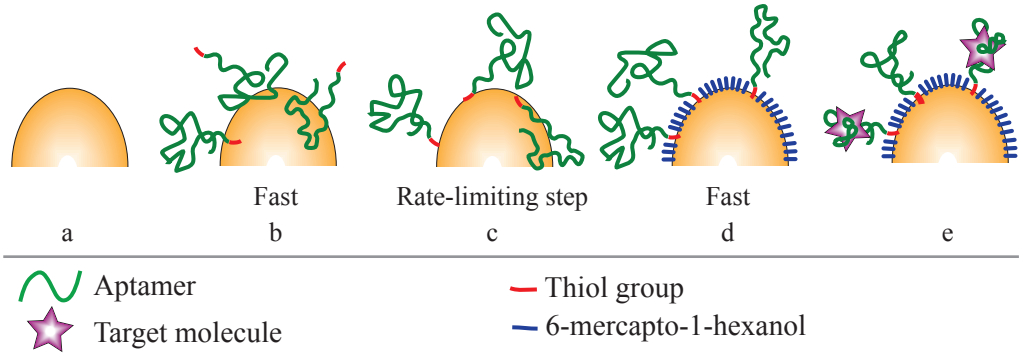


Figure 3.3: Schematic of the chosen functionalisation strategy. Aptamer is first quickly physically adsorbed to the cleaned metal nanopillar surface (a,b). Sufficient incubation will allow the thiol group of the aptamer to bind to the metal surface (c). Unspecific binding is then prevented by 6-mercapto-1-hexanol (MCH) (d), which quickly form self-assembled monolayers (SAMs) on the metal surface. Aptamer-target capture is achieved by proper folding of the aptamer (e).

### 3.2.1 Pretreatment

Prior to any chemical functionalisation a cleaning procedure of the metal coated nanopillars was required. This was to remove any organic contamination which might have accumulated since fabrication. An important note is, that once the functionalisation protocol was started all steps were done

wet-in-wet, as drying in between steps would facilitate irreversible leaning of the nanopillars, making it difficult to trap molecules in hot spots.

#### Silver substrates

Silver substrates were sequentially immersed in 99 % ethanol and $H_2O$ for 3 min each. By starting chemical functionalisation with immersion in ethanol the super hydrophobic nanopillars could easily be wetted, which made downstream handling easier. Substrates fresh out of metal deposition are not super hydrophobic, but rather the contrary. During the course of a day the substrates are contaminated with organics, which renders the surface hydrophobic.

#### Gold substrates

Since gold is not prone to oxidation a more harsh chemical cleaning could be applied. This meant that organic contamination on gold substrates were removed by 35 sec $O_2$ plasma treatment at 0.5 mbar oxygen pressure (Plasma cleaner ATTO, Diener Surface Technology). The substrates were then sequentially immersed in 99 % ethanol and $H_2O$ for 3 min each within 15 min of the $O_2$ plasma treatment. It was observed that gold substrates would regain its hydrophilic surface after the $O_2$ plasma treatment. A recent study by Xue et al. [64] even demonstrate that oxidation of the gold surface can enhance binding of thiols. The immersion in 99 % ethanol will however chemically reduce the gold to zero state (metallic gold). They report on 120 min immersion for complete reduction of the gold surface, which could indicate that not all of the gold surface is reduced after 3 min.

### 3.2.2 DNA aptamer immobilisation

DNA aptamer sequences were acquired with a $C_6$-disulphide ($C_6$-S-S) modification in the 5'-end. By breaking the disulphide bond it is possible to create two individual thiol functional groups ready for immobilisation. This is done by utilizing the reducing agent Tris(2-carboxyethyl)phosphine hydrochloride (TCEP·HCl), which is very effective at reducing disulphide bonds at room temperature.

Table 3.3 lists the DNA sequences used throughout the project. The DNA strands were ordered HPLC purified and lyophilised from DNA Technology A/S (Aarhus, Denmark). The acquired powder was dissolved in $H_2O$ and kept at -18°C. In order to avoid repeated freezing and thawing a portion of the solution was aliquoted into suitable amounts when initially dissolved.

Table 3.3: DNA sequences used in experiments throughout the project.

| Name | Sequence 5'-3' | Ref. |
|---|---|---|
| E2 aptamer #1 (76-mer) | GCTTCCAGCTTATTGAATTACACGCA-GAGGGTAGCGGCTCTGCGCATTCAA-TTGCTGCGCGCTGAAGCGCGGAAGC | [10] |
| E2 aptamer #2 (75-mer) | ATACGAGCTTGTTCAATACGAAGGG-ATGCCGTTTGGGCCCAAGTTCGGCA-TAGTGTGGTGATAGTAAGAGCAATC | [31] |
| E2 cDNA#2 | GATTGCTCTTACTATCAC | |
| E2 ncDNA#2 | AGTCGTCATGGCAAGGAT | |

### 3.2.3 Blocking

Once the DNA aptamer has been immobilised on the metal surface it is important to block the remaining binding sites with a proper molecule. This is to prevent unspecific binding of target molecules and the DNA phosphate backbone. Several molecular options are available in varying sizes and structure. In this project MCH was chosen due to its identical length to the $C_6$ spacer of the DNA modification. MCH likewise utilises its thiol group to bind to gold and silver and have been reported to yield SAMs on both metals [65–68]. The combination of DNA and MCH is also widely described in literature and have been used for decades for passivation of gold and silver. It is also reported that MCH serves to lift off collapsed DNA from the surface [16] making sure it obtains its optimal availability for target binding.

### 3.2.4 Aptamer folding

To enable target capture of the aptamer it is important to obtain the proper tertiary 3D structure. This can be done by denaturing (unfolding) the DNA strand and allowing it to regain its structure. There are currently two common ways of achieving this:

1. Heating to 94°C for 10 min followed by rapid cooling on ice [69].
2. Immersion in high ionic strength solution to break hydrogen bonds by electrostatic screening [57].

The first method is the least invasive considering possible contributions to the background Raman signal, whereas the second method requires less instrumentation. However by heating the substrate above approximately 70°C it is

possible to break thiol-gold bonds [70] and thereby lower the surface coverage of both aptamer and MCH. Therefore the second option was chosen in this project.

### 3.2.5 Target capture

After aptamer folding it should be immersed in a suitable buffer solution. The tertiary structure is heavily dependent on the composition of the salts in the buffer solution. Hence it is critical for target capture capabilities of the aptamer to be in a proper buffer. Studies have shown that multivalent cations (e.g. $Mg^{2+}$, $Ca^{2+}$) in particular aid in stabilizing intra-strand hydrogen bonds and helps maintain proper aptamer folding [69, 71]. Buffers for aptamers used in this project were chosen from the reported SELEX process in which the aptamers were selected. Succeeding capture, unbound target molecules can be washed off in pure buffer solution.

### 3.2.6 Cross-contamination and chip handling

In all functionalisation steps it is important to avoid any source of contamination as the fabricated SERS substrates are extremely sensitive to any molecular adsorption. Often several SERS chips were being handled simultaneously, which made cross-contamination a great risk. All (roughly) 4x4 mm diced chips were handled using stainless steel tweezers, which had been cleaned in ethanol and water followed by drying with compressed air prior to any functionalisation step. The use of tweezers introduced several scratches on the edge of the nanostructured surface, but they did not hinder SERS measurements in the centre of the chips. Eppendorf LoBind™ microtubes and LoRetention™ pipette tips were used when appropriate.

### 3.2.7 Assay parameters

Figure 3.4 shows a diagram of the functionalisation procedure including the parameters having an effect on the individual step. The time of incubation in any step is always a parameter that could have significant influence on the overall functionality of the sensor. Often there is also a concentration of a molecule to control, which is correlated to the incubation time. For each experiment performed these parameter will be stated and discussed.

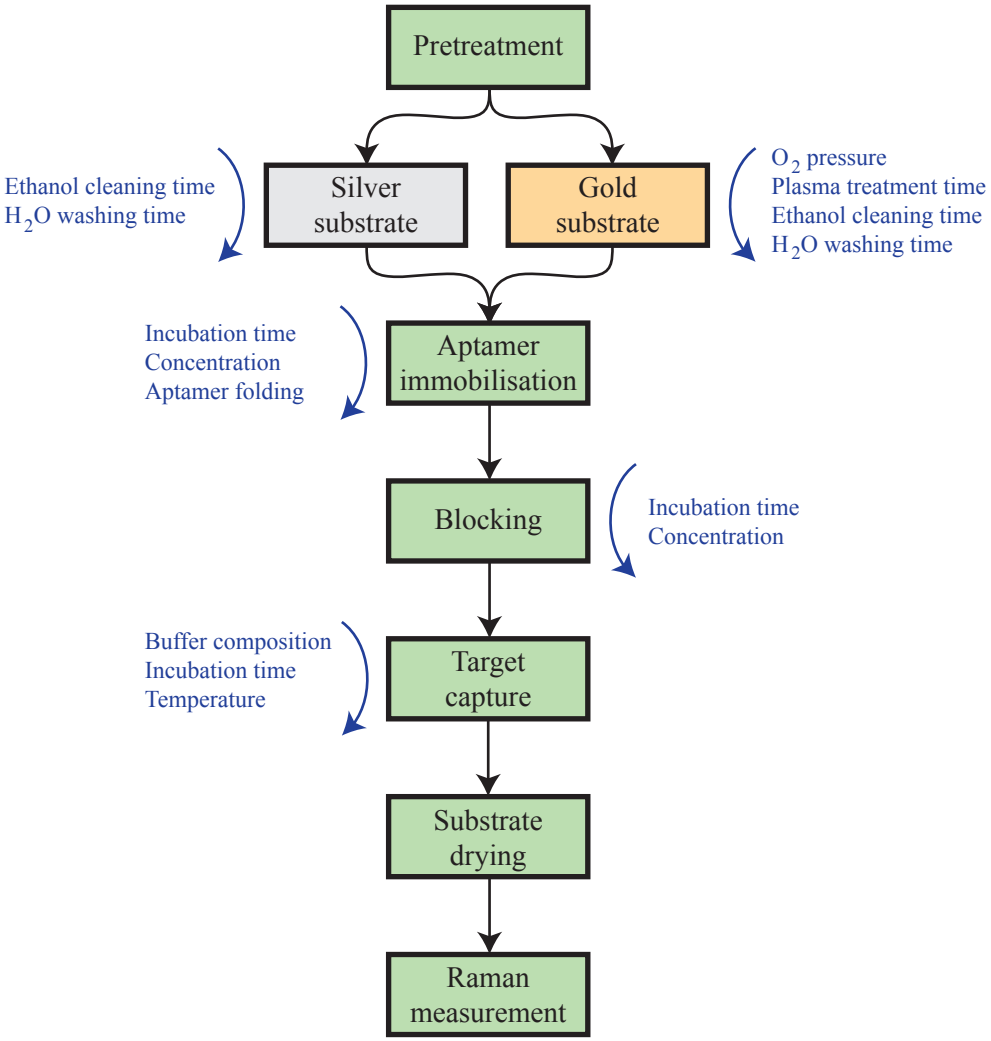


Figure 3.4: Diagram showing all steps and parameters in the chosen functionalisation strategy. Silver and gold substrates require different pretreatment steps, as silver is prone to oxidation. All steps prior to substrate drying were done wet-in-wet to prevent nanopillar leaning.

# 4 Results and Discussion

Several experimental studies were carried out during the course of the project. Initially a minor study related to Track 1 was conducted. It was investigated whether a thiolation of an anti-suPAR antibody would enhance binding to gold and increase the selectivity compared to silicon dioxide. This was to aid in developing the cantilever immunoassay performed by other group members. Following the initial study the focus was set on Track 2 and developing a SERS aptasensors for 17$\beta$-estradiol detection. The initial efforts for development of this sensor are described in Experiment A. Based on these results a better understanding of the functionalisation protocol was needed. This resulted in investigation of aptamer binding to the nanopillar surface described in Experiment B, followed by a thorough investigation of functionalisation parameters for development of a generic aptasensor SERS protocol in Experiment C. Lastly it was attempted to develop a SERS aptasensor specifically targeted at detecting 17$\beta$-estradiol, which is described in Experiment D.

## 4.1 Thiolated anti-suPAR antibody

Initially in the project a minor experiment relating to Track 1 was conducted. Gold coated silicon cantilevers were to be used for suPAR detection (by other group members), which meant that anti-suPAR antibodies were to be immobilised on the surface. The cantilevers only had a gold coating on the top side, which meant that unspecific binding to the bottom silicon dioxide side was expected. Since cantilever biosensors rely heavily on capturing a target on one side only, it was investigated if adding a functional thiol-group to the antibody would yield enhanced binding to gold. This was conducted on a Quartz Crystal Microbalance with Dissipation (QCM-D) (Q-sense E4 system, Biolin Scientific, Sweden) system. Briefly, a QCM-D operates by measuring changes in resonant frequency of an oscillating quartz crystal. When a molecule adsorbs on the surface the mass of the crystal changes, which in turn changes

the resonant frequency. The dissipation (ring-off) of the crystal carries information regarding the stiffness of the formed layer, however in this study only the resonant frequency changes were studied.

### Method

The first, third, fifth and seventh order resonant frequency was monitored at 20°C on silicon dioxide and gold coated quartz crystals (Biolin Scientific) in these experiment. Before any experiment was carried out the system was cleaned by flushing with 2 % Hellmanex® in $H_2O$. A new QCM-D chip (gold or silicon dioxide coated) was inserted afterwards and the liquid chamber was filled with 100 µl antibody solution (10 µg/ml in 1xPBS). The antibody analysed in this set of experiments were anti-D3 antibody supplied by MUSE project partner ViroGates A/S. It is specific towards the D3-region of the suPAR molecule [1]. The solution was allowed to immobilise onto the QCM-D chip surface without flow. The resonant frequencies were monitored for 90 min.

### Results and discussion

Figure 4.1 shows average frequency shifts and standard deviations of three repeat experiments. From here only a slight difference is seen between silicon dioxide and gold coated chips when investigating un-modified anti-D3 adsorption. However a clear discrepancy is seen for thiolated anti-D3. Even though only a minor improvement was obtained for the gold coated surface, a clear change in binding to silicon dioxide is seen. This shows that by adding a functional thiol-group to the antibody it is possible to avoid unspecific binding to silicon dioxide in cantilever experiments. This should greatly enhance cantilever biosensor performance.

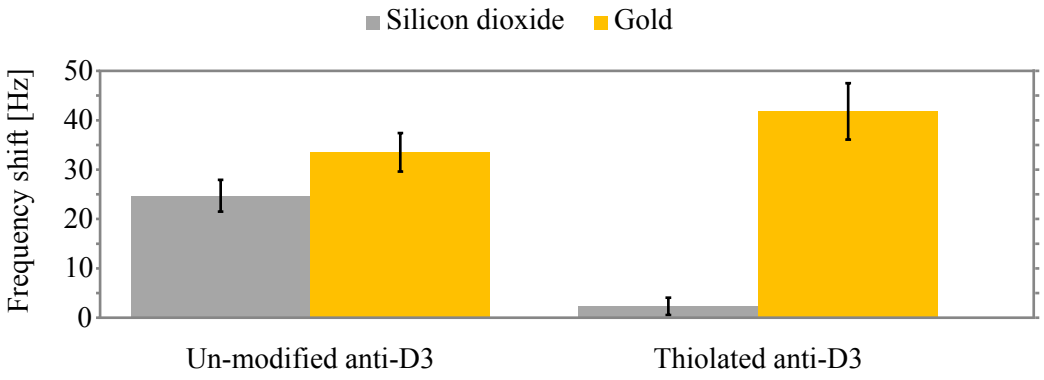


Figure 4.1: Results from the QCM-D experiment showing average resonant frequency shifts and standard deviations of three repeat measurements. It is seen that thiolated anti-D3 antibodies exhibit a slightly higher binding towards gold compared to un-modified antibodies. However almost no change in resonant frequency was observed for thiolated antibodies functionalised on silicon dioxide crystals, which is in contrast to the results for un-modified antibodies. This shows that by using thiolated antibodies it is possible to obtain a higher degree of functionalisation of antibodies while simultaneously decreasing the unspecifically bound antibodies on silicon dioxide.

### Conclusion to QCM-D experiment

Initially in the project it was investigated how binding of anti-D3 antibody was affected on gold and silicon dioxide surfaces by addition of a functional thiol-group. Binding to gold showed only a slight improvement, however it was observed that almost no binding to silicon dioxide occurred. This is of great importance in cantilever biosensors, which relies on selective adsorbtion on a single side of the cantilever.

### Publication

Based on the measurements performed on the QCM-D and subsequent cantilever experiments (by other group members) the following article was published in the journal 'Nanotechnology'. In brief it describes detection of nanomolar level suPAR using multiple (16-24) cantilevers in serial on a rotating polymer platform. Cheap DVD optics were used as a highly sensitive readout method. This work demonstrated the possibility of developing reliable and robust tools for diagnostics and prognostics.

It can be found at:
`http://www.ncbi.nlm.nih.gov/pubmed/24113286`

## 4.2 General SERS substrate performance

All batches of SERS substrates had very strong enhancements. Uniformity was achieved on all but a 1-2 cm rim on the edge of each wafer. A slight variation in the Raman intensity was seen when testing chips from different areas using 1,2-di-(4-pyridyl)-ethylene (BPE). BPE is commonly used in SERS for analysis of substrate performance due to its very strong Raman activity [72, 73]. These tests were not performed on all batches, but visual inspection followed by normal experiments determined that batch-to-batch variations were of minor character. Average spectra ($n = 3$) of BPE (1 µl of 100 µM BPE in ethanol dried on a 5x5 mm chip) from 3 different gold substrates are shown in Figure 4.2, where only minor variations are seen in peak intensities. The molecular structure of BPE is shown as an insert. These spectra prove that the fabrication process is reliable and repeatable. Measurement performed by other group members have determined that silver substrates exhibit even stronger enhancement factors than gold substrates [61, 74]. This meant that a free choice of substrate was available at the beginning of the development of a SERS aptasensor.

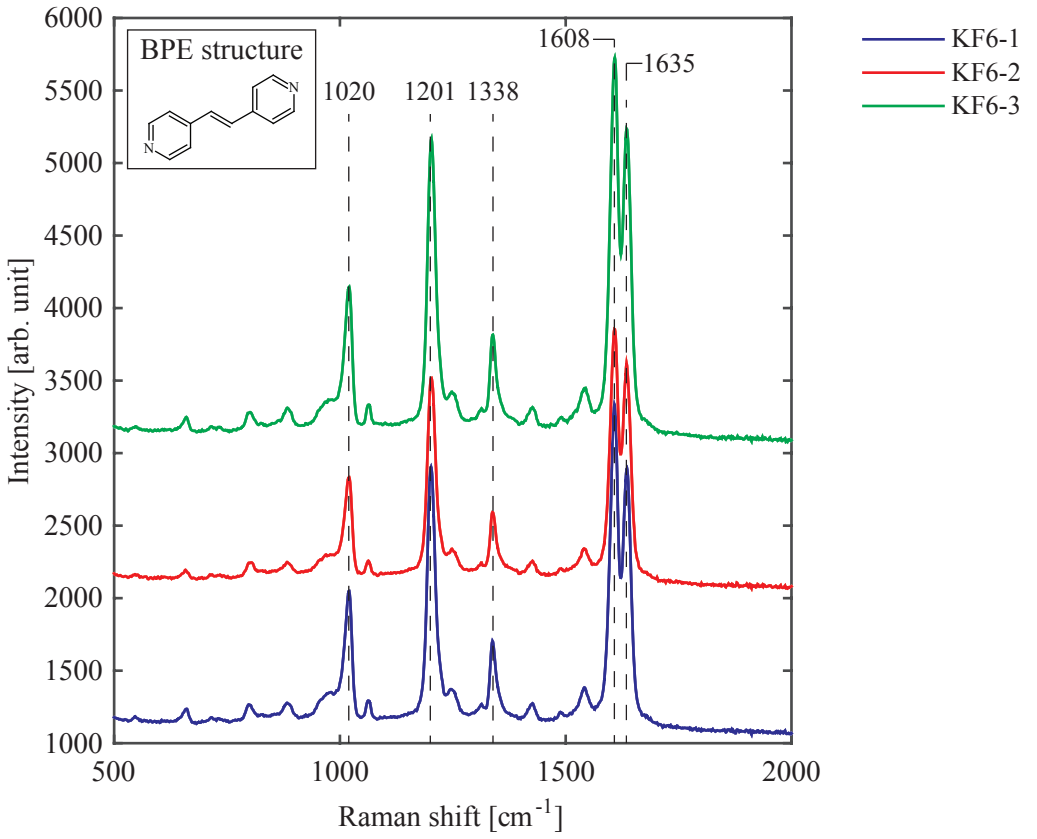


Figure 4.2: BPE benchmark spectra on batch KF6. The three different wafers show very similar spectra. This is evidence of a reproducible fabrication process.

# 4.3 Experiment A - Labelled target

Development of an aptasensor for 17$\beta$-estradiol detection was initiated on the silver SERS substrates. Two different functionalisation assay options existed in the early stage development:

1. Direct assay with label-free detection of 17$\beta$-estradiol.
2. Indirect assay with labelled 17$\beta$-estradiol in competition with pure 17$\beta$-estradiol.

Since labelled molecules are easier to detect in Raman systems it was decided to initiate aptasensor development using the second option. Estradiol Glow (Jena Bioscience GmbH, Germany) was chosen as a starting point since it is fluorescently labelled 17$\beta$-estradiol. It was chosen due to its inherently strong Raman activity, which was ideal for initial studies. The chemical structure is shown in Figure 4.3. It should be noted that it could not be known beforehand if the fluorescent label would hinder aptamer binding. Estradiol Glow is however biologically active (see data sheet in Appendix A.2), which aspired optimism towards successful aptamer binding.

Silver substrates were chosen over gold since initial studies showed stronger enhancement factors on silver. This however put some limits on the chemical cleaning procedures: as silver oxidises easily no oxygen plasma cleaning was performed.

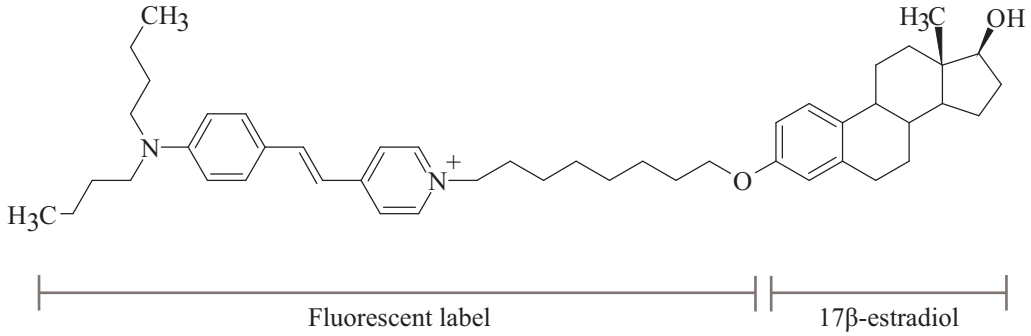


Figure 4.3: Schematic of the molecular structure of Estradiol Glow. The fluorescent label exhibits a very strong Raman signal.

## 4.3.1 Raman acquisition settings

The Raman settings displayed in Table 4.1 were used throughout this set of experiments. A laser at 780 nm wavelength was used throughout the SERS studies. Excitation at 780 nm yielded very strong enhancement for both silver

and gold substrates. The highest magnification available was used in order to achieve the smallest laser spot size possible. This allowed for probing the minimum number of nanopillar hot spots as possible to yield the lowest detection limit. A 1.6 µm laser spot size diameter however still covers 20-40 single nanopillars, which means that spectra obtained do not originate from a single nanopillar cluster.

Table 4.1: Raman acquisition settings for Experiment A.

| Parameter | Setting |
|---|---|
| Wavelength | 780 nm |
| Estimated laser spot size | 1.6 µm |
| Power | 0.5 mW |
| Magnification | 50x |
| Exposure time | 0.5 sec |
| No. of exposures | 2 |
| Baseline correction | 6th order polynomial |

The spectrum of Estradiol Glow on silver substrates was obtained by drying 1 µl on the substrate after the initial ethanol and water cleaning procedure. Two different concentrations (100 nM and 1000 nM in ethanol) were investigated in a 100x100 µm area with 1 µm step size in both directions, yielding $n = 10,000$ spectra to be inspected. The average spectra is shown in Figure 4.4 where several peaks are present. The most prominent are 1166 $cm^{-1}$, 1325 $cm^{-1}$, 1465 $cm^{-1}$ and 1580 $cm^{-1}$, where the first and the latter should prove to be most prominent in later experiments. It should be noted that for this series of experiments an internal baseline correction (6th order polynomial) was done before the data was exported from the DXR Raman Spectroscope. This meant that non-physical negative intensity values could be obtained.

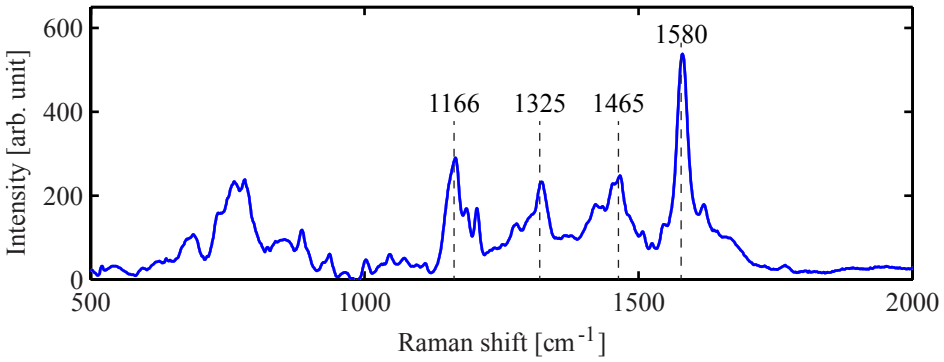


Figure 4.4: Average spectrum ($n = 10,000$) of 1000 nM Estradiol Glow on silver substrate. The most dominant peaks are 1166 $cm^{-1}$, 1325 $cm^{-1}$, 1465 $cm^{-1}$ and 1580 $cm^{-1}$, where the first and the latter proved most reliable in further experiments.

By calculating the average spectrum it is easy to obtain information about the most dominant peaks in a spectrum, however the distribution of these are lost. To get a better view of the data the peak value can be plotted for the entire area map. Figure 4.5 shows the intensity of the 1166 $cm^{-1}$ peak, where it is easy to identify the areas with the strongest enhancement (red areas).

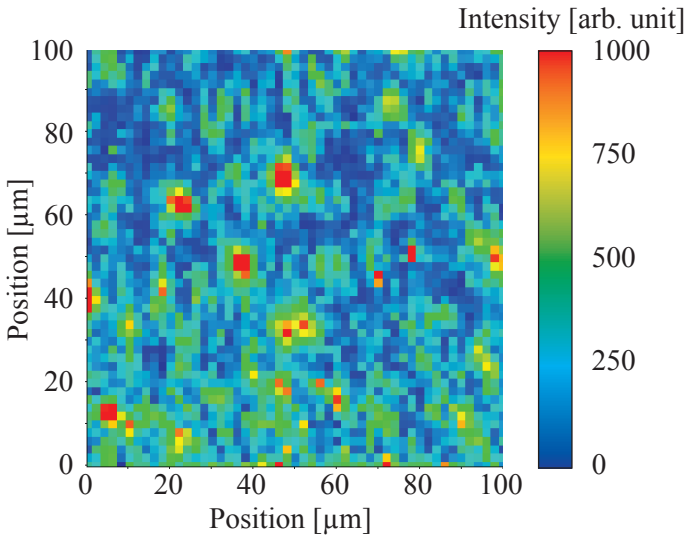


Figure 4.5: Intensity map of the 1166 $cm^{-1}$ peak for 1000 nM Estradiol Glow. Regions of strong signal intensity (red) are clearly seen in between regions of low intensity (blue).

This type of plot provides a good visual overview of the data, where concentration dependent behaviour can be observed - as shown in Figure 4.6. Here 100 nM and 1000 nM maps display a large variation in high-intensity areas, which is indicative of molecules being more sparsely spread for the lower concentration.

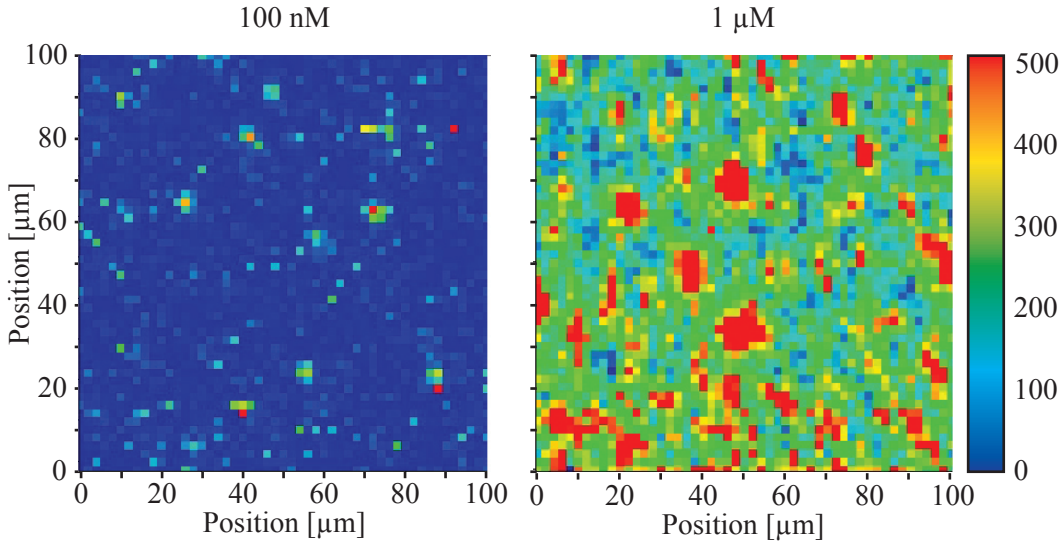


Figure 4.6: Intensity maps of the 1166 $cm^{-1}$ peak for 100 nM and 1000 nM Estradiol Glow. A significant difference between the two maps are seen, where the strongest intensities are seen for the highest concentration. This is expected due to the sparse distribution of Estradiol Glow molecules at 100 nM compared to 1000 nM. However strong regions of high intensity can still be observed for 100 nM, which shows that some hot spots generate stronger enhancement than others.

Together with plotting a histogram (Figure 4.7) of the intensity of peaks observed, these type of plots yield powerful tools for visualisation of large amounts of Raman spectra. From the histograms it can be seen that when the concentration of Estradiol Glow is increased so is the intensity. The distribution is also broadened, which shows that more molecules are trapped in high intensity hot spots yielding strong Raman signals. Both distributions are seen to exhibit heavy tailed behaviour as expected for SERS measurements [40].

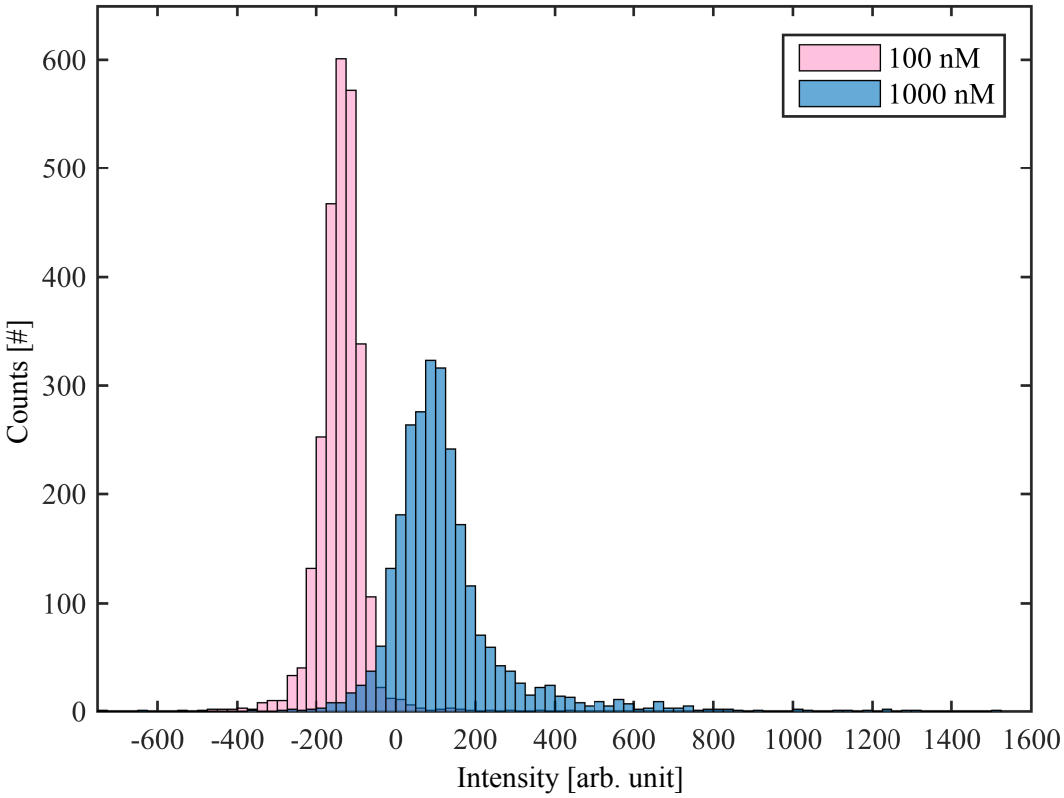


Figure 4.7: Histogram of intensities at 1166 $cm^{-1}$ for 100 nM and 1000 nM Estradiol Glow. When the concentration is increased there is a clear shift towards higher intensities and a broadening of the distribution. This is expected due to sparse scattering of molecules at low concentration.

### 4.3.2 Multivariate analysis

Despite being a powerful visual tools these type of data analysis can hide important variations in the map, which could have influence on the conclusions drawn. This is highlighted in Figure 4.8, where three vastly different spectra yield high intensities for the Raman shift of 1166 $cm^{-1}$. By solemnly relying on the visual representation of a certain Raman shift, it is clear that faulty conclusions can be drawn, since a peak might not be observed in this position. It is important in Raman spectroscopy to observe peaks rather than just an enhanced background, which could arise for many reasons. The grey spectra of Figure 4.8 shows the expected Raman spectrum for Estradiol Glow (as shown by the 1000 nM average in Figure 4.5). The green spectrum shows a peak in at the 1166 $cm^{-1}$ position, which could be indicative of Estradiol Glow being present. However the spectrum is seen to consist of more peaks than the pure Estradiol Glow spectrum. This shows that some sort of contamination is also present in the spectrum, which was un-observable in the visual map. Lastly the red spectrum shows an elevated background spectrum. This could arise from salt aggregation on the nanopillars, which experience fluorescence. This is clearly not a spectrum of Estradiol Glow, but in the visual map it is analysed as such.

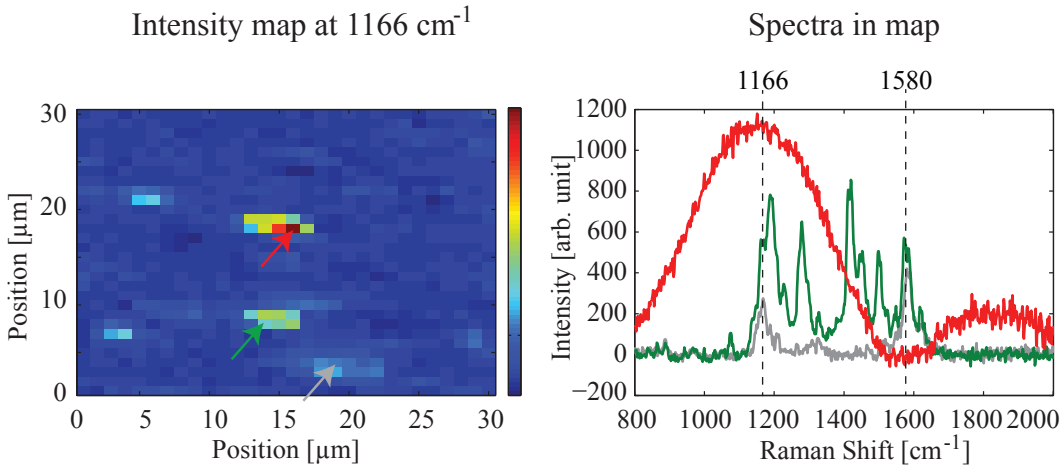


Figure 4.8: Intensity map of 1000 nM Estradiol Glow including three spectra (marked by arrows) from high intensity regions. The three spectra are clearly different when inspected individually, however they appear alike in the intensity map. This will cause miss-interpretation of spectral data on large ensembles.

To eliminate miss-interpretation of the results a filtering method was developed in close collaboration with DTU Compute. Non-negative Matrix Factorization (NMF) is a multivariate analysis method in which the data ($X$) is divided into a loadings matrix ($L$) and a spectral component matrix ($S$) that multiplied approximately yields the observed data

$$X = LS, \tag{4.1}$$

where $X \in \mathbb{R}, L \in \mathbb{R}_+$ and $S \in \mathbb{R}_+$. Neither of the matrices ($L$ and $S$) are allowed to contain negative elements, which put some constraints on the application. However for spectral analysis like Raman spectroscopy where intensities are measured, this is a suitable analysis. In fact by using NMF compared to more conventional multivariate analysis like Principal Component Analysis (PCA) it is possible to gain more information, since the matrices can be individually interpreted without losing physical meaning. This would not be the case of e.g. PCA where a negative element in one of the matrices could never relate to a spectroscopic intensity.

In addition to $L$ and $S$, measurement noise and spectral background is to be expected. Therefore the complete model of the data is described as

$$X = LS + B + E, \tag{4.2}$$

where $B$ is the spectral background and $E$ is the measurement noise/error, which can take all real values (including negative). By allowing numerical factorization of the data according to this method it is possible to obtain a new visualisation of the data shown in Figure 4.9. Here the first two vectors of $S$ are shown along with the corresponding values of $L$. The first spectral component of $S$ clearly resembles the average spectra of Estradiol Glow with peaks at 1166 $cm^{-1}$ and 1580 $cm^{-1}$. It should be noted that the y-axis does not represent the intensity of the data, but rather a 'vector intensity'. By inspecting the corresponding loadings for this particular vector is it seen that certain regions are highlighted. These are areas where this vector have a 'high loading', meaning that it is highly present in the spectrum. This allows for quick identification of areas of interest where Estradiol Glow spectra can be seen. The second spectral component reveals a strong peak at 1166 $cm^{-1}$, which could be indicative of Estradiol Glow, including some contamination. This spectra is confined to a single region in the NMF map. By utilising NMF is it possible to easily identify regions of interest for detection of a specific spectra.

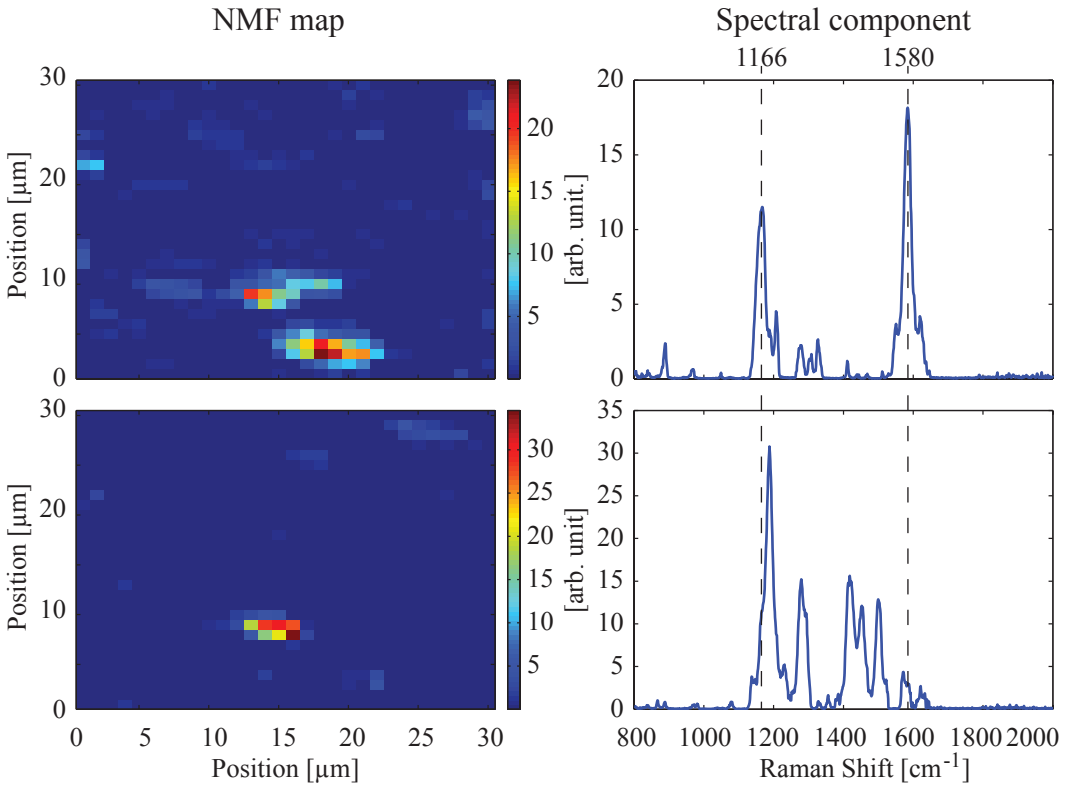


Figure 4.9: Non-negative Matrix Factorization of 1000 nM Estradiol Glow intensity map. Two maps (left) are shown for the two first spectral components (right). The first spectral component strongly resembles the average spectra of Estradiol Glow. Regions of high loading in the NMF map reveals where Estradiol Glow spectra can be found. The second spectral component reveals strong vector intensity at 1166 $cm^{-1}$, which could be indicative of Estradiol Glow including some contamination. This spectrum is confined to a single region in the NMF map. Based on this separation of spectra it is easy to categorise regions of interest compared to normal intensity maps.

It should be noted that there are several differences between the normal intensity map and the NMF map. Especially the high intensity area by the red arrow in intensity map of Figure 4.8 is seen to vanish in the NMF map for the first spectral component Figure 4.9. When inspecting the actual spectra it was seen that this area did not contain any Estradiol Glow peak, but rather an enhanced background. These are correctly not identified as Estradiol Glow by the NMF model, which proves its validity.

### 4.3.3 Functionalisation protocol

As a starting point for assay parameters a functionalisation protocol published by Yang et al. [57] was used. The protocol had been previously developed in a collaboration between professor Lin's group at Columbia University in the

city of New York and our group. The protocol was based on an earlier version of the SERS substrate with 4 min etch and only 30 nm gold deposited. The following describes the general protocol, which was used throughout the experiments on silver substrates.

In this set of experiments the E2 aptamer #1 from Table 3.3 was used. The binding buffer composition was [10]: 100 mM Tris–HCl, 200 mM NaCl, 25 mM KCl, 10 mM $MgCl_2$, 5 % ethanol.

1. **Aptamer pre-treatment**
   (a) Prepare 100 µl 5 µM aptamer solution in $H_2O$.
   (b) Prepare 100 µl 500 µM TCEP·HCl solution in Tris-Buffered Saline (TBS).
   (c) Adjust pH of TCEP solution to 4-5 using drops of 37 % HCl for optimal disulphide reduction [57].
   (d) Mix 100 µl TCEP solution into the aptamer solution and incubate for 15 min at room temperature.
   (e) Add 100 µl TBS to the mix immediately before immersion of the SERS substrate.

   The final volume is 300 µl, which is sufficient for full immersion of 2-3 4x4 mm SERS substrates in different 500 µl microtubes. The final aptamer concentration is 1.66 µM.

2. **Substrate pre-treatment and aptamer functionalisation**
   (a) Immerse the substrate in 99 % ethanol for 3 min.
   (b) Immerse the substrate in $H_2O$ for 3 min.
   (c) Transfer directly into the aptamer/TCEP solution and incubate for 240 min at 37°C.

3. **Blocking and aptamer folding**
   (a) Transfer directly to 2 mM MCH in $H_2O$ for 60 min.
   (b) Immerse the substrate in $H_2O$ for 3 min.
   (c) Immerse the substrate in 4 M UREA in TBS for 3 min.
   (d) Immerse the substrate in $H_2O$ for 3 min. Repeat once.

4. **Target binding and rinsing**
   (a) Prepare Estradiol Glow in binding buffer.
   (b) Immerse substrate into solution and incubate for 240 min at 37°C.

(c) Transfer directly to pure binding buffer to remove unbound molecules. Incubate for 15 min.

(d) Dip quickly for 5 sec in $H_2O$ to prevent salt aggregation on substrate. Repeat once.

(e) Leave the substrate to dry.

Once the substrate is dry Raman measurements can be obtained.

Since different concentrations of Estradiol Glow was attempted to be detected, it was decided to obtain Raman spectra for varying area sizes to minimize the data acquisition. It was expected that low concentration of test analyte would require more data to be obtained in order to account for the sparse distribution of molecules. Based on previous work in the group by Yang et al. [57], it was decided to use the area map sizes shown in Table 4.2 to have statistical sufficient data.

Table 4.2: Area map sizes for experiments with varying concentration of Estradiol Glow. The step size was set to 1 µm in each direction.

| Concentration | Map size | Measurement points |
|---|---|---|
| 0 nM | 100x100 µm | 10,000 |
| 10 nM | 100x100 µm | 10,000 |
| 100 nM | 40x40 µm | 1,600 |
| 1000 nM | 30x30 µm | 900 |

### 4.3.4 Detection limit

The detection limit of this SERS sensor was investigated by firstly analysing the intensity maps of the 1166 $cm^{-1}$ peak. Figure 4.10 shows data for 1000 nM, 100 nM, 10 nM and blank samples of Estradiol Glow. For blank and 10 nM samples almost no signal is seen at 1166 $cm^{-1}$ which indicates no presence of Estradiol Glow. The minor "peaks" seen for 10 nM showed to be due to enhanced background rather than a peak. At 100 nM regions appear with high intensity. When inspected, these were shown to reflect the expected spectrum of Estradiol Glow. At 1000 nM these regions are stronger and more frequent. Despite some of these belonging to enhanced background, there was a clear presence of Estradiol Glow in the data. Notice also that despite the small area analysed for 100 nM and 1000 nM (1600 $\mu m^2$ and 900 $\mu m^2$ respectively) compared to blank and 10 nM (10,000 $\mu m^2$) a strong presence of Estradiol Glow could easily be detected by normal visual inspection.

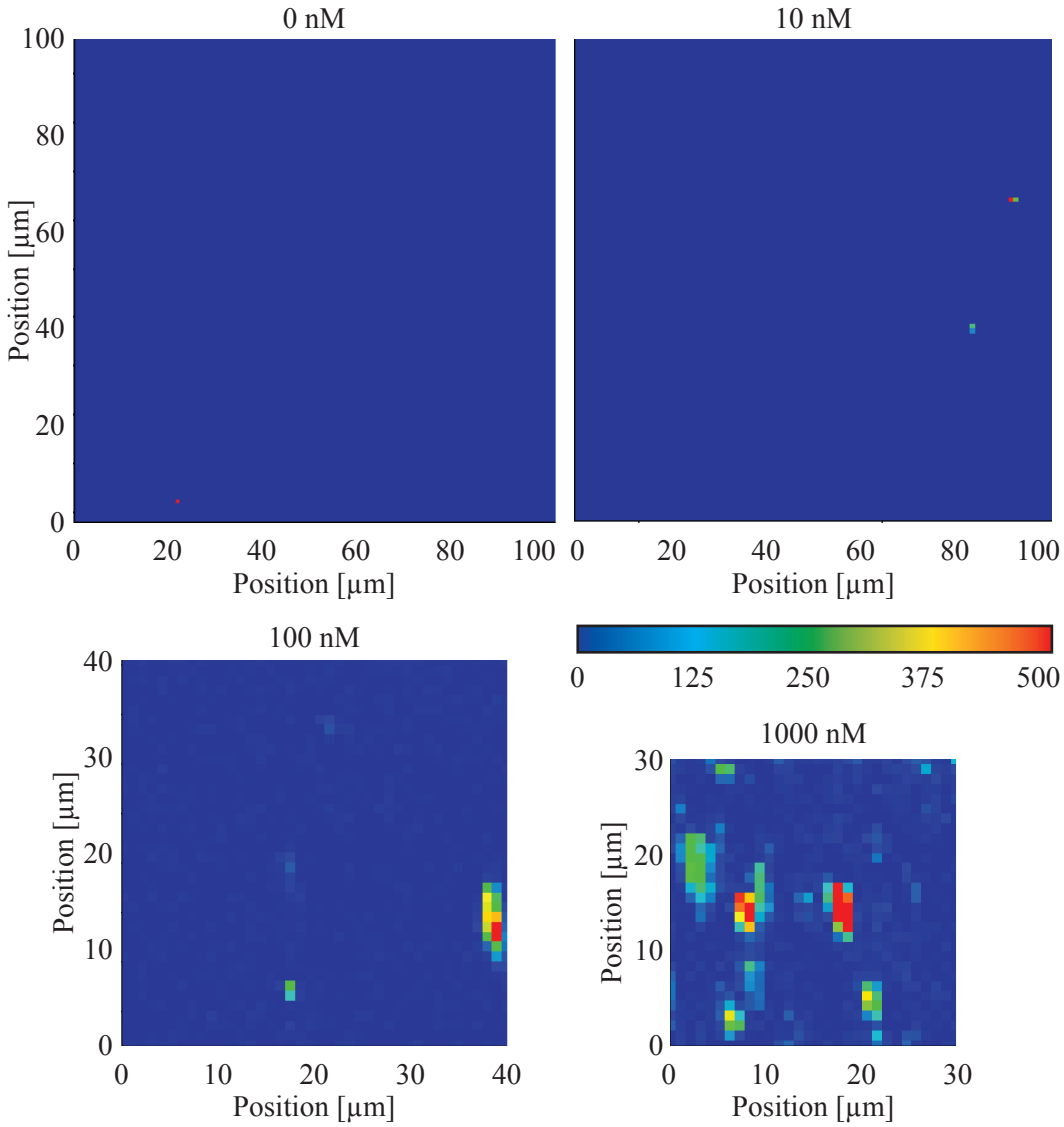


Figure 4.10: Intensity maps of 1166 $cm^{-1}$ for varying concentrations of Estradiol Glow (batch: KF3-2). Blank and 10 nM maps show very limited intensities at 1166 $cm^{-1}$, which is indicative of no Estradiol Glow being present. However for both 100 nM and 1000 nM regions of strong intensities are seen. It should be noted that the measurement points for different concentrations were varied to take into account the sparse distribution of molecules at low concentration. Based on this analysis only 100 nM Estradiol Glow could be detected.

However when applying NMF on the dataset for 10 nM several interesting features are seen. Figure 4.11 shows the analysis, where the intensity map (left), which is rescaled compared to Figure 4.10, still shows little activity at 1166 $cm^{-1}$. However when inspecting the NMF map (middle) a minor area indicated by the white arrow is clearly highlighted. A spectra from this region is shown on the right. Here it is seen that a faint Estradiol Glow signal is observed. The two peaks at 1166 $cm^{-1}$ and 1580 $cm^{-1}$ are present in this spectra, which proves the presence of Estradiol Glow. The spectra in this area had not been identified earlier as Estradiol Glow due to the low intensity at 1166 $cm^{-1}$ as all ten thousand spectra can not be indiviually examined. However by utilizing NMF they can now easily be properly classified. Using NMF have effectively increased the sensitivity of the SERS sensor one order of magnitude, since very faint spectra can be located.

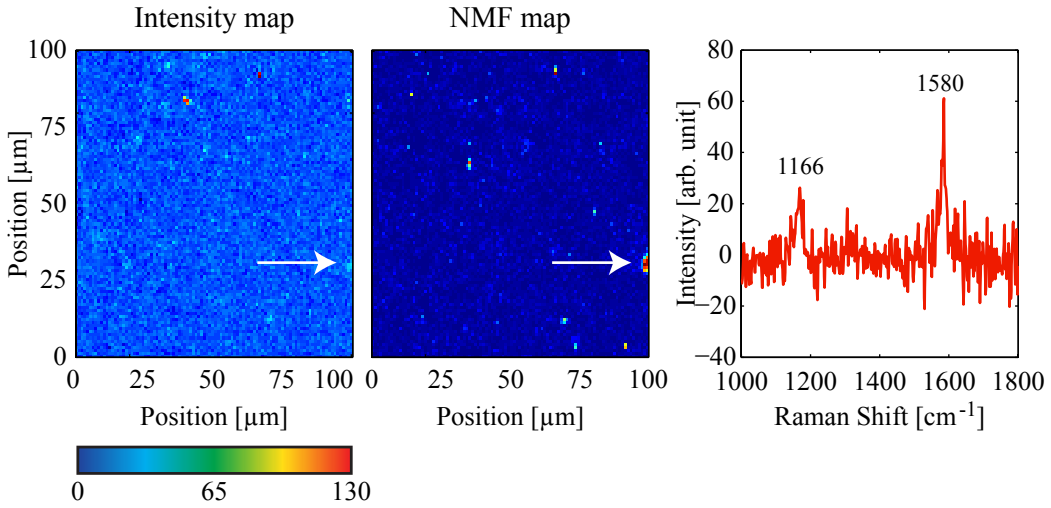


Figure 4.11: Non-negative Matrix Factorization applied on the data of 10 nM Estradiol Glow (batch: KF3-2). The area indicated by the white arrow shows no particular intensity in the intensity map, however in the NMF map the region is clearly identified. An actual spectrum from this region (right) is shown to have peaks at both 1166 $cm^{-1}$ and 1580 $cm^{-1}$, which is indicative of Estradiol Glow.

It should be noted that in this NMF analysis the average spectra of Estradiol Glow was feeded into the algoritm, which allows it to only search for a desired spectrum in a huge ensemble. This was done since the Estradiol Glow spectra of 10 nM were too faint to be recognised autonomously by the algoritm.

### 4.3.5 Observation of aptamer on silver substrates

During the cause of the experiments presented above two observations were made. These observation rendered the data obtained for aptamer functionalised substrates unusable for development of a SERS aptasensor for Estradiol Glow.

#### Incorrect aptamer modification

After all experiments had been carried out it was discovered that the modification at the 5'-end of the aptamer contained a thio-ether with a trityl group termination instead of the wanted disulphide. The data sheet is shown in Appendix A.3. This meant that the TCEP·HCl had no effect on providing thiol (-SH) terminated DNA sequences, which drastically lowered both the binding to gold and the availability of aptamer. Despite the lack of a terminal thiol DNA still binds to gold through nitrogen in the backbone. However any aptamer bound to the gold surface would suffer from laying flat on the nanopillars not being capable of obtaining a proper 3D folding for target capture. Samples containing aptamer did also reveal a different spectra compared to samples without (data not shown), but there was not observed any difference in the detection limit of Estradiol Glow. This implies that the data shown above is for **negative control samples - i.e. no aptamer was present** in the functionalisation protocol. Therefore the data represents the degree of unspecific binding of Estradiol Glow to the silver nanopillars. The conclusions drawn are therefore still valid.

#### Chemical reaction between nanoscale silver and hydrochloric acid

Another observation made was that small particles were clearly seen as aggregates on top of the nanopillar surface in optical microscopy. This was observed throughout the experimental set with varying degree. Figure 4.12 shows a normal nanopillar surface (left) and one were particles had aggregated (right). Obtaining Raman spectra from the region of high density of particles led to almost no spectrum obtained, whereas regions outside the particles where the nanopillars were exposed yielded a decent spectrum. However the origin of the particles was unknown as it had not been observed for previous experiment performed by Yang et al. [57]. Therefore it was believed that the change from gold to silver substrates had to be the reason. It was found that a chemical reaction between nanostructured silver and hydrocloric acid had been published by Li et al. [75]. They explain an observation that silver on the nanoscale can easily react with hydrocloric acid to form silvercloride particles. This is a plausible explanation since hydrocloric acid is used both in reducing agent TCEP·HCl directly and to lower the pH of the solution to aid disulphide

breakage. Removing the additional hydrocloric acid showed no change, meaning that the small amount present from the TCEP·HCl itself was enough to form the particles. The reason that the particles were not observed until MCH was added, could be due to that SAMs are formed on the particles in solution making them aggregate on the surface. This has not been further investigated as following experiments were made on gold substrates, where the formation of particles was never observed.

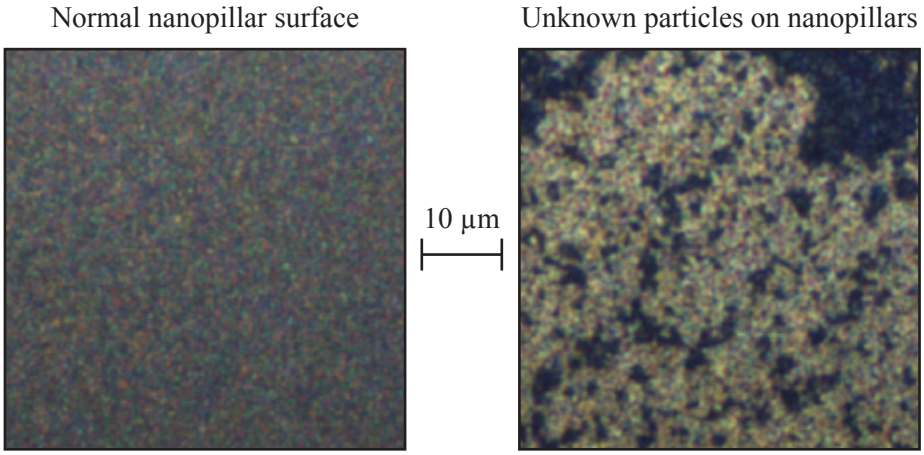


Figure 4.12: Optical images of normal silver nanopillars (left) and nanopillars where unknown particles have been deposited (right) (batch: KF5-2). It is believed that hydrocloric acid reacts with the nanoscale silver to form silvercloride particles.

### 4.3.6 Conclusion to Experiment A

Estradiol Glow was investigated on silver substrates to be implemented in a competitive assay for 17$\beta$-estradiol detection. Experiments showed that Estradiol Glow expressed very strong Raman activity, which made it ideal for initial investigation. When inspecting the data it was seen that contamination could be observed in the spectra. This could lead to miss-interpretation of intensity maps, as an enhanced background caused by e.g. aggregation of salt, would show as a false positive signal. To eliminate these errors a multivariate analysis model was employed. The NMF model successfully discriminated between true and false positive signal by analysing the entire spectrum rather than a single peak value. By applying this method the detection limit was improved by a factor 10.

Despite the successful detection of Estradiol Glow it was discovered that an incorrect aptamer modification had been used. This rendered the data for aptamer funcionalised nanopillars unusable. However data for negative control without aptamer was analysed instead.

It was also discovered that nanostructured silver reacts strongly with hydrocloric acid to form silvercloride particles. This meant that the nanopillars were etched during the functionalisation procedure, which lowered the SERS performance of the substrate. These particles aggregated on the nanopillar surface in different sizes. Some areas were completely covered in particles where left clear. Raman spectra have solemnly been acquired for particle-free areas, where the enhancement was still seen to be acceptable.

### 4.3.7 Publications

#### Patent

The following patent application have been filed based on the methods and results described in this section. It will become publicly available 18 months after filing date.

Tommy Sonne Alstrøm, Mikkel Nørgaard Schmidt, Jan Larsen, **Kasper Bayer Frøhling**, Anja Boisen, Michael Stenbæk Schmidt. Method to lower the detection limit and enhance the sensitivity of surface enhanced Raman based sensors, EPO 14185146.9-1504, filed 17 September 2014.

#### Article

Based on the results presented in this section the following article was published. It describes the use of NMF on large ensembles of SERS data.

It can be found at:
`http://ieeexplore.ieee.org/xpl/articleDetails.jsp?reload=true&arnumber=6958925`

# 4.4 Experiment B - Aptamer immobilisation

B

Following the initial attempt of developing an aptasensor it was decided to more thoroughly investigate aptamer immobilisation on the SERS substrate. This was achieved by utilizing fluorescently labelled complementary DNA (cDNA) on gold SERS substrates. Since silver substrates were shown not to be compatible with the chosen functionalisation strategy a switch to gold was required. The complementary strand was chosen due to its inherent strong binding affinity to the aptamer. It is likewise easy to obtain chemically modified DNA strands, which makes it possible to choose a labelling molecule to utilise in a SERS assay. Since the labelling molecule is conjugated to the end of the DNA strand it will not hinder binding to the aptamer, which makes it ideal for testing aptamer immobilisation. This experiment did not aim at finding the detection limit for the labelled cDNA, but only establish that aptamer binding occurs. Also it was investigated how an $O_2$ plasma cleaning prior to any functionalisation affected the obtained spectra and background. Furthermore the effect of the non-ionic detergent Tween20 during hybridisation and washing was investigated - in particular on the effect of non-specific binding of DNA to the nanopillars. Like the cantilevers used for suPAR detection (described in section 4.1), the nanopillars have two surfaces: gold and silicon. Only selective binding to gold was desired.

It should be clearly stated that the proper $C_6$-S-S disulphide modification of the 5'-end of the aptamer was used in this set of experiment (data sheet shown in Appendix A.4).

## 4.4.1 Protocol

This set of experiments were carried out immediately after the external stay at Columbia University in the city of New York. This allowed the functionalisation procedure to be optimised as per [57]. A purification step using Illustra MicroSpin G25 columns was implemented to remove unwanted compounds from the aptamer/TCEP solution. The aptamer immobilisation buffer was changed from TBS (suggested by Kim et al. [10]) to 1xPBS. The added volume of buffer to the final aptamer solution was increased to yield 1 µM solution - this change should not particularly affect the surface coverage of aptamer compared to 1.66 µM. The high ionic strength solution was changed to 2 M UREA and 7.5 mM EDTA in $H_2O$. Since DNA hybridisation was to be investigated the binding buffer was changed to 5xSSC.

The aptamer sequence from E2 aptamer #2 in Table 3.3 was employed on batch KF6-2 for all experiments in this section. This aptamer was published in February 2014 [31] and reported to have higher binding affinity towards

17$\beta$-estradiol ($K_d = 50$ nM) compared to the existing aptamer [10] ($K_d = 130$ nM). The cDNA and non-complementary DNA (ncDNA) sequences in Table 3.3 were used.

1. **Aptamer pre-treatment**

   (a) Prepare 100 µl 5 µM aptamer solution in $H_2O$.

   (b) Prepare 100 µl 500 µM TCEP·HCl solution in $H_2O$.

   (c) Mix 100 µl TCEP solution into the aptamer solution and incubate for 60 min at room temperature.

   (d) Purify on Illustra MicroSpin G25 columns.

   (e) Add 300 µl 1xPBS to the mix immediately before immersion of the SERS substrate.

   The final volume is 500 µl, which is sufficient for full immersion of several 4x4 mm SERS substrates in individual 500 µl microtubes. The final aptamer concentration is 1 µM.

2. **Substrate pre-treatment and aptamer functionalisation**

   (a) Clean the substrate by 35 sec exposure to $O_2$ plasma.

   (b) Immerse the substrate in 99 % ethanol for 3 min.

   (c) Immerse the substrate $H_2O$ for 3 min.

   (d) Transfer into the aptamer/TCEP solution and incubate for 180 min at room temperature.

3. **Blocking and aptamer folding**

   (a) Transfer the substrate directly into 1 mM MCH in $H_2O$ and incubate for 60 min.

   (b) Immerse into $H_2O$ for 3 min.

   (c) Immerse into 2 M UREA and 7.5 mM EDTA in $H_2O$ for 3 min.

   (d) Immerse into $H_2O$ for 3 min. Repeat once.

4. **Target binding and rinsing**

   (a) Prepare 1 µM cDNA or ncDNA in binding buffer +/- 0.1 % Tween20.

   (b) Immerse substrate into solution and incubate for 60 min.

   (c) Transfer directly to binding buffer +/- 0.1 % Tween20 and incubate for 5 min. Repeat twice.

   (d) Transfer directly to binding buffer and incubate for 5 min. Repeat twice.

(e) Dip quickly for 2 sec in $H_2O$ to prevent salt aggregation on substrate. Repeat once.

(f) Leave the substrate to dry.

Once the substrate is dry Raman measurements can be obtained.

### 4.4.2 Raman acquisition settings

In this set of experiments the settings in Table 4.3 were used for Raman acquisition. The number of data points measured was $n = 300$ for all experiments. These were obtained in a 30x10 point mapping configuration with 2 µm step size. A few changes compared to Experiment A have been made: power lowered to 0.1 mW; exposure time reduced to 0.1 s; number of exposures reduced to 1 and no baseline correction was done. These changes were made to lower the acquisition time, while still obtaining a strong Raman signal.

Table 4.3: Raman acquisition settings for Experiment B.

| Parameter | Setting |
|---|---|
| Wavelength | 780 nm |
| Estimated laser spot size | 1.6 µm |
| Power | 0.1 mW |
| Magnification | 50x |
| Exposure time | 0.1 sec |
| No. of exposures | 1 |
| Baseline correction | None |

### 4.4.3 Raman spectra of DY776 fluorophore

The fluorophore chosen for this experiment was named DY-776 and obtained from Dyomics GmbH (Germany). It was conjugated to the 5'-end of the cDNA and ncDNA strand by the manufacturer DNA Technology (Denmark) (data sheets shown in Appendix A.5 and A.6). The label was chosen without prior knowledge about its Raman activity since this information was not available. It was therefore chosen on the basis of the absorbance maximum, which at 771 nm was close to the wavelength of the laser used in the experiments (780 nm). It was therefore necessary to investigate the Raman spectra of the labelled DNA before using it in actual experiments. Figure 4.13 shows the average spectra

(here $n = 25$ only) of varying concentrations of labelled cDNA. These spectra show raw data and have not been offset. The spectra were obtained by allowing 1 µl solution in $H_2O$ to dry on the 4x4 mm substrate after cleaning in ethanol and $H_2O$.

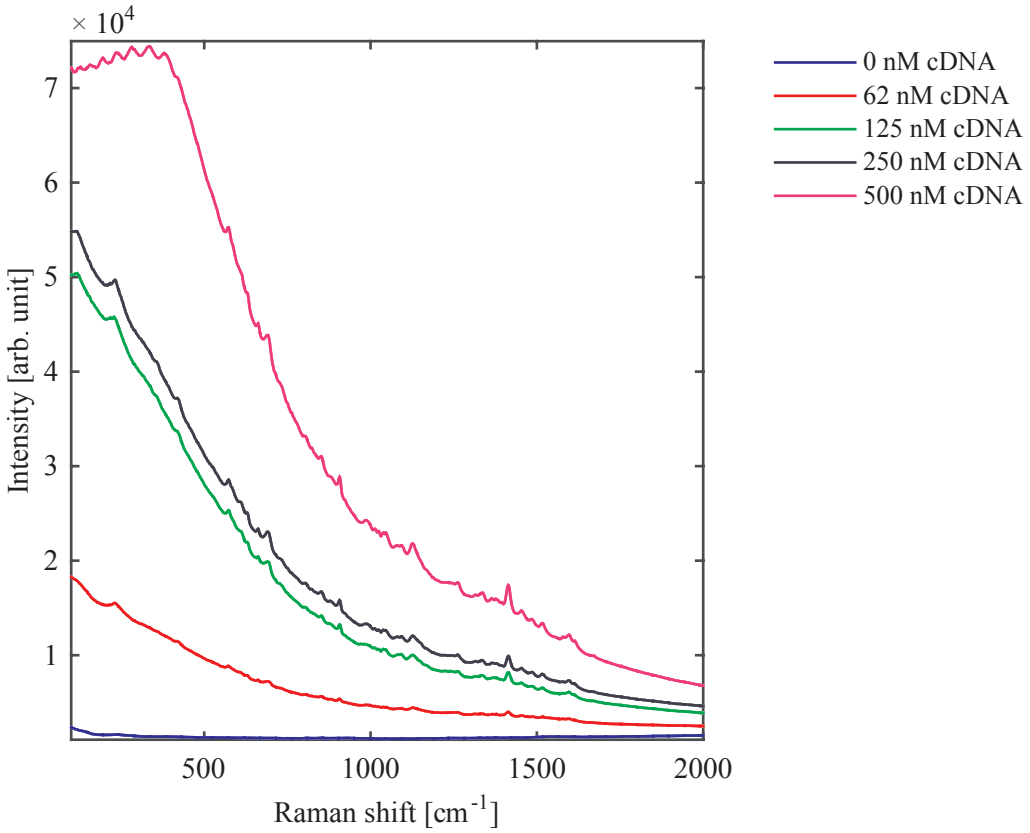


Figure 4.13: Average spectra of varying concentrations of DY-776 labelled cDNA (batch: KF6-2). Some minor peaks are seen, however a greatly enhanced background for low Raman shifts are seen. This is due to fluorescence of the chosen label and can clearly be seen to increase with DNA concentration.

As can be seen for the 500 nM sample the detector of the Raman spectrometer becomes saturated at low wavenumbers (around 500 $cm^{-1}$). This is evident from the very regular oscillations seen from this point and below. Therefore the following plots are shown in the range 500-2000 $cm^{-1}$. In general only minor peaks are seen, while there is a strong tendency of high intensity background for low wavenumbers. This is how flourescence appear in Raman spectra, which makes sense due to the absorbance maximum of the fluorophore being close to excitation wavelength of the laser. Despite the high fluorescence these spectra show that the labelled cDNA can easily be detected by the system.

In order to better visually examine all data each of the 5x25 spectra were plotted as a color coded line as shown in Figure 4.14. Here the x-axis shows the

Raman shift, the y-axis represents the order of which the spectra was obtained and the colorbar shows the Raman intensity. As can be seen there is some variation of the spectra for each measurement, but the fluorescence is clearly seen at low wavenumbers. The fluorescence is also clearly seen to increase with increasing concentration of DNA.

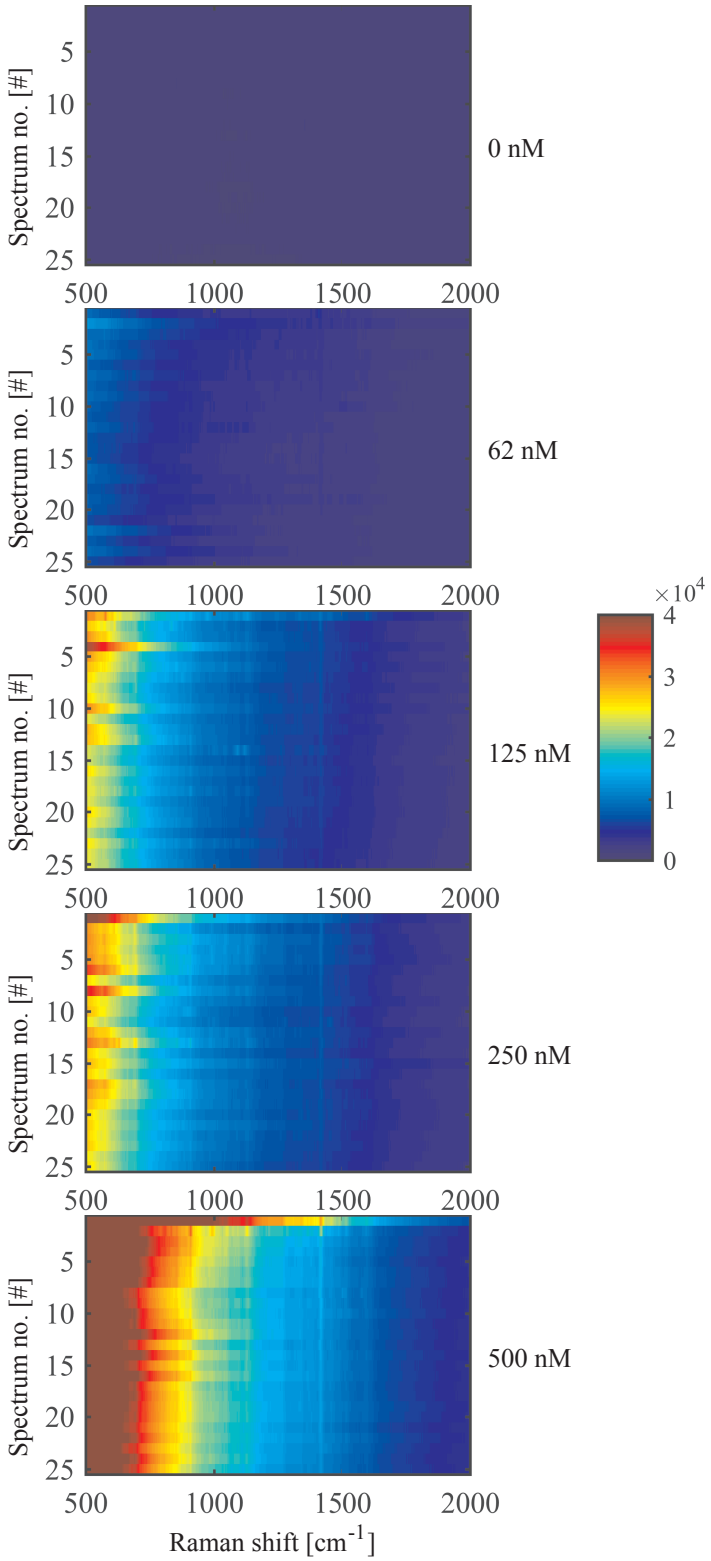


Figure 4.14: Colormaps for varying concentrations of DY-776 labelled cDNA (batch: KF6-2). A fluorescent signal at low Raman shifts is seen to increase for increasing cDNA concentration.

### 4.4.4 Experimental samples

The experiment was divided into three different tests based on the actual sample. Either cDNA, water or ncDNA was tested in order to investigate the selectivity and specificity of the sensor. All samples were tested on both aptamer functionalised and blank substrates. The ncDNA was chosen so that a maximum of four base pairs in a row matched the aptamer sequence. The set of 31 individual experiments was randomised in order to eliminate day-to-day, chip-to-chip and other non-casual effects. The background spectra obtained for the experiment (i.e. substrate submerged in $H_2O$ for 300 min after cleaning) is shown in Figure 4.15. As seen no particular background is present for this batch of chips[1].

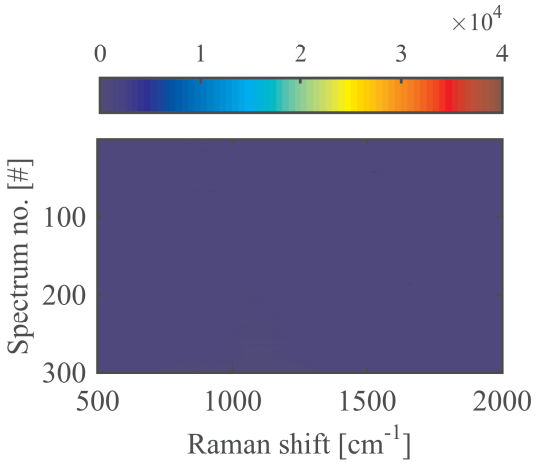


Figure 4.15: Colormap of $H_2O$ background (batch: KF6-2). No particular spectrum is seen, which indicates that the fluorescence obtained in experiments originates from the labelled cDNA or ncDNA.

#### Complementary DNA sample

Colormaps of the spectra from experiments with cDNA is shown in Figure 4.16. It is clearly seen that a fluorescent signal from the DY-776 label is present at low wavenumbers in all samples containing aptamer. The strongest signal is seen for experiments where the substrates have been $O_2$ plasma cleaned prior to functionalisation with aptamer. No unspecific binding is occurring for either experiment without aptamer, which indicates that the cDNA binds specifically to it. It is also observed that removing the non-ionic detergent Tween20 from the hybridisation buffer significantly decreases the signal obtained from non-$O_2$

[1]It should be noted that even though $n = 300$ it is not possible for printers or computer screens to show all 300 lines in small areas. The color plots however still represent a valid visual overview of the data.

plasma treated substrates. Since both the addition of Tween20 to the hybridisation buffer and the $O_2$ plasma treatment of the substrate have the inherent property of altering the surface tension between the buffer and substrate (enhanced wetting), this might be a crucial factor to control in order to achieve strong binding. The surface tension has not been measured, but it was visually observed that $O_2$ plasma cleaning made the gold substrates very hydrophilic, as if the batch was recently fabricated.

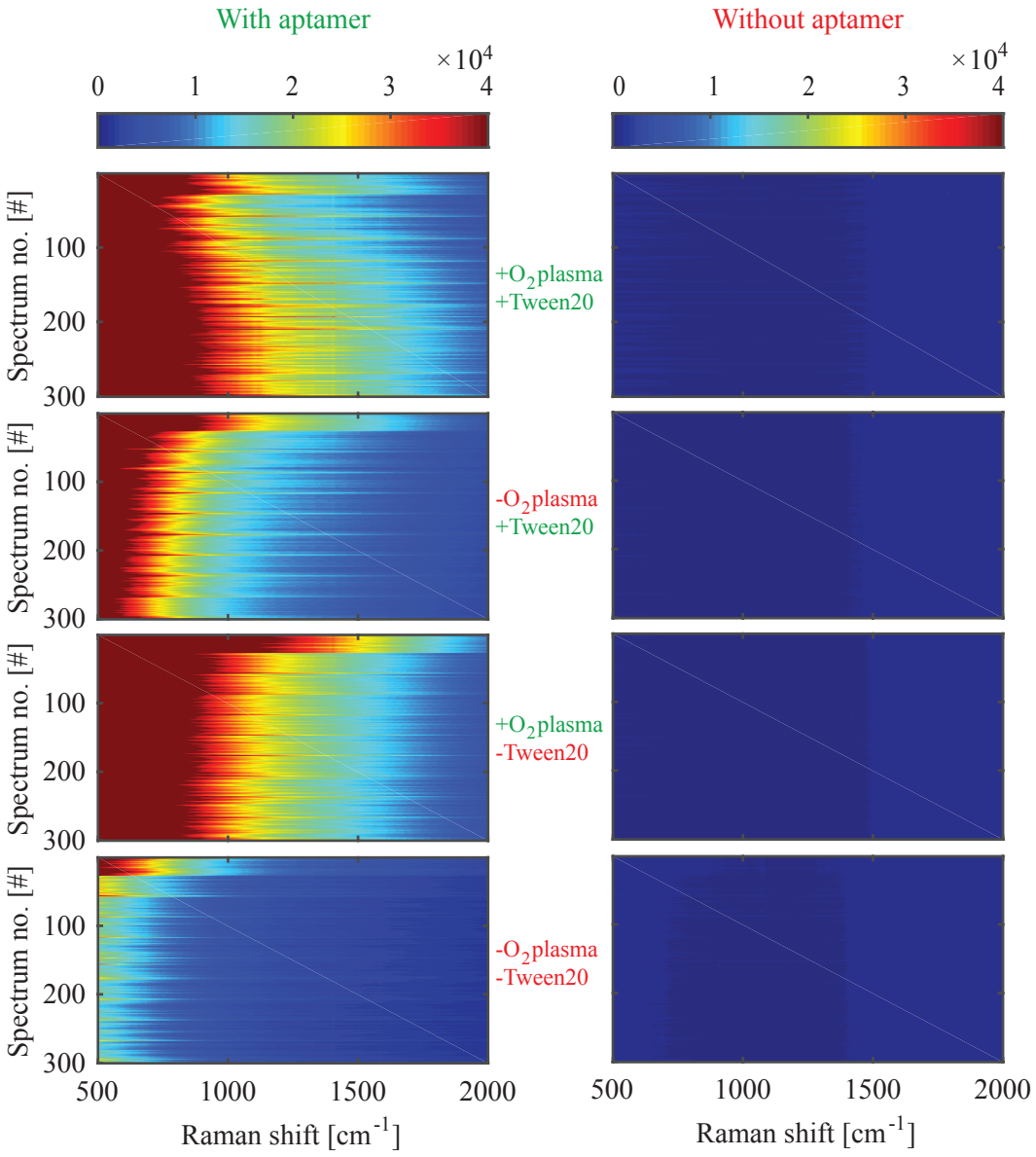


Figure 4.16: Colormaps of cDNA samples on substrates with (left) and without (right) aptamer functionalisation (batch: KF6-2). It is clearly seen, that fluorescent signals are only obtained for aptamer functionalised substrates. This indicates that cDNA binds to the immobilised aptamer and that practically no unspecific-binding to the nanopillars occur. Samples for substrates treated with $O_2$ plasma is seen to yield stronger signals than substrates without. Likewise the presence of Tween20 in the hybridisation buffer seems to increase the signals for non-$O_2$ cleaned subtrates.

### Water sample

Samples containing water instead of cDNA in the hybridisation step was used as a negative control. Colormaps are shown in Figure 4.17, where it is evident that almost no signal is seen for these samples. In fact only a slight background signal is seen from the aptamer when $O_2$ cleaned substrates are used in combination with Tween20 in the hybridisation buffer. The aptamer signal is however very low compared to the cDNA signals seen previously. Again the strongest signal is seen for $O_2$ plasma cleaned substrates, whereas the spectra of non-functionalised chips exhibit almost identical spectra to that of the $H_2O$ background (Figure 4.15).

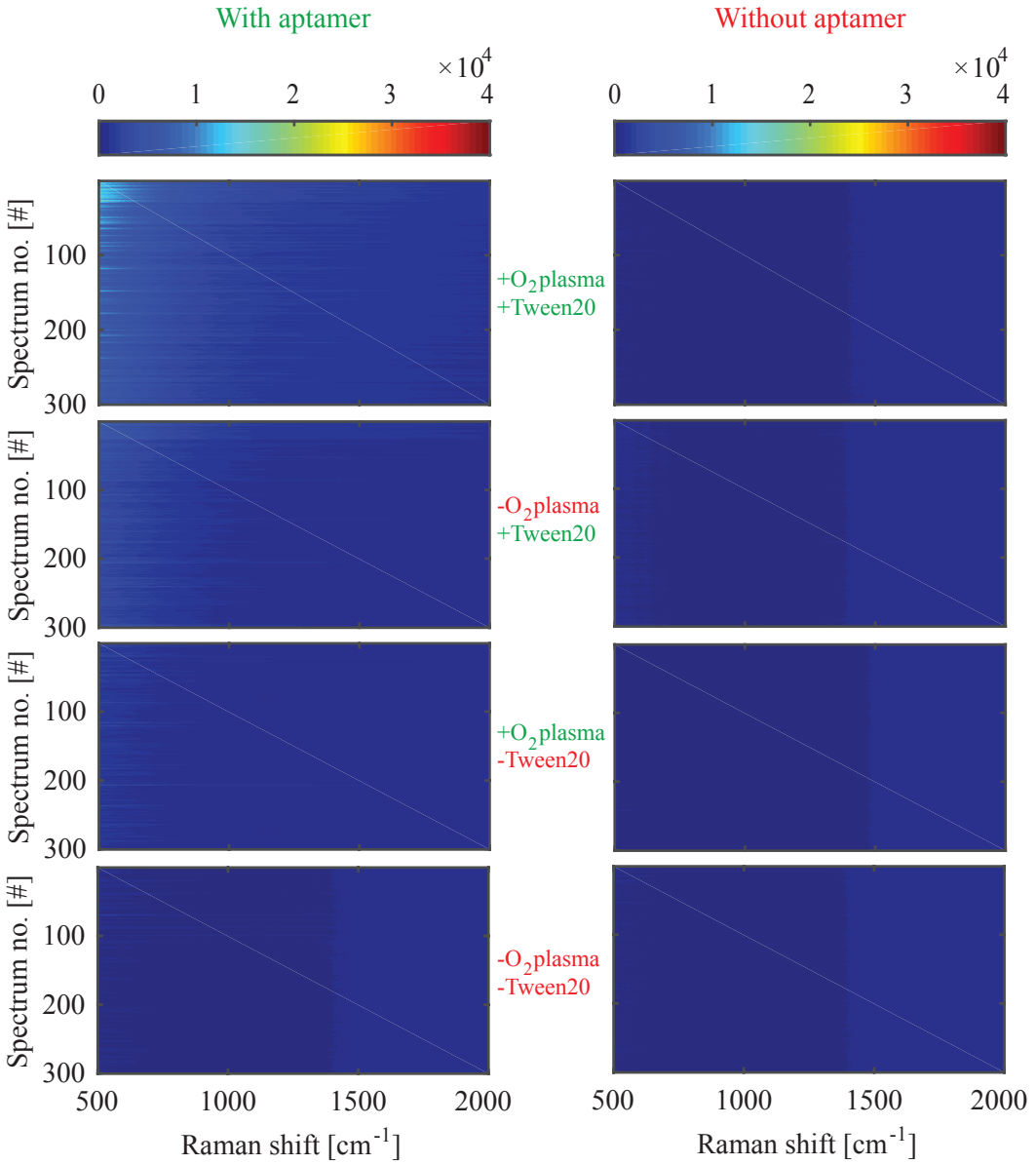


Figure 4.17: Colormaps of water samples on substrates with (left) and without (right) aptamer functionalisation (batch: KF6-2). Almost no signal is obtained for any sample regardless of the surface treatment. A minor signal for the aptamer functionalised, $O_2$ treated sample with Tween20 in the hybridisation buffer is seen.

### Non-complementary DNA sample

Samples containing non-complementary DNA (ncDNA) were used to test the specificity of the aptamer towards the cDNA sequence. The ncDNA has the same length as the cDNA (18 bases), but only a maximum of four bases in a row will match anywhere on the aptamer. Colormaps of the spectra obtained are shown in Figure 4.18, where it is seen that no fluorescence is observed regardless of the surface functionalisation and treatment. This is evidence of the aptamer binding specifically to the cDNA, which demonstrates that the aptamer is properly immobilised on the nanopillar surface with the ability of forming bonds to other molecules. This was an important conclusion to draw since it is pivotal for developing a functioning aptasensor towards 17$\beta$-estradiol.

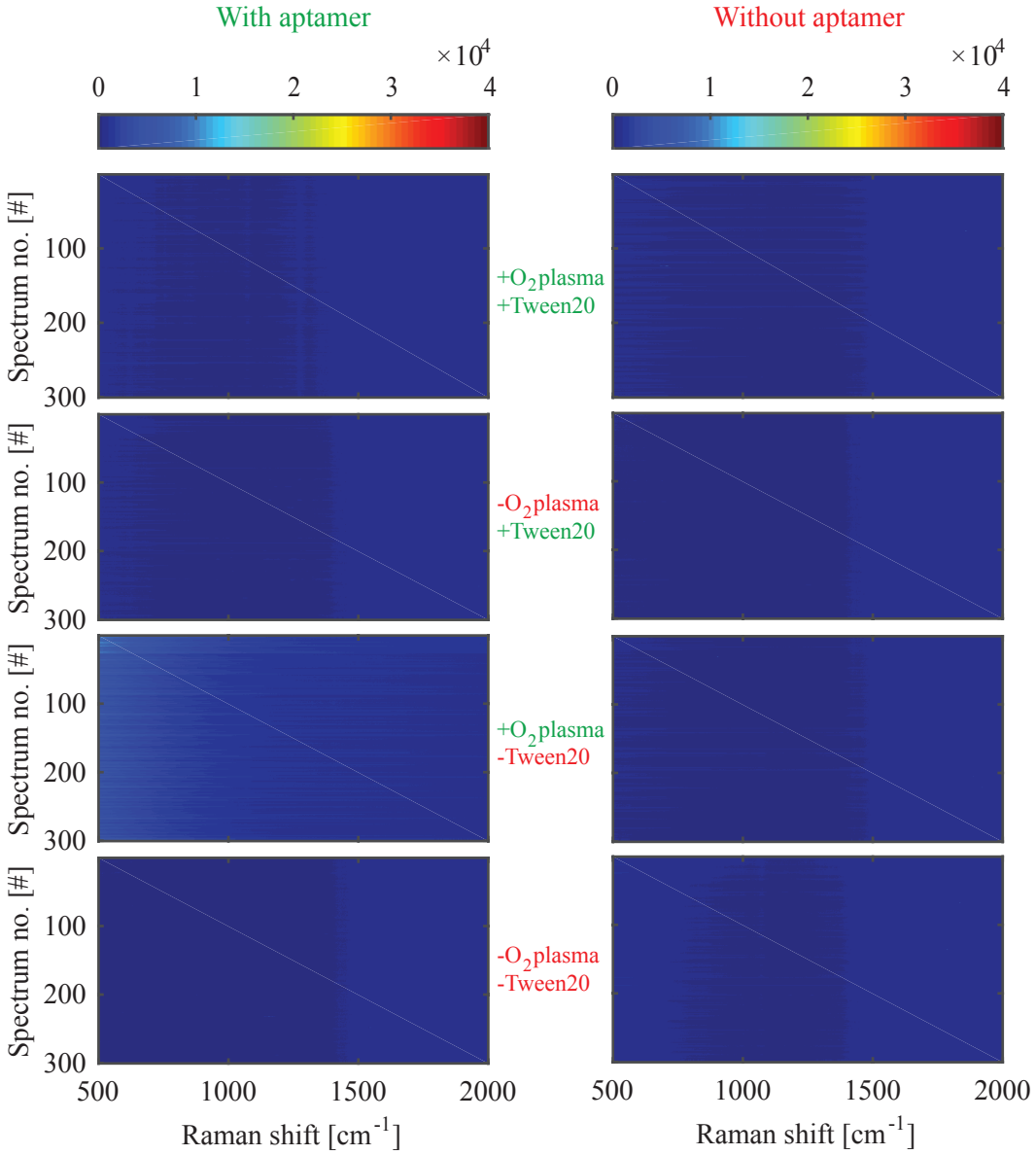


Figure 4.18: Colormaps of ncDNA samples on substrates with (left) and without (right) aptamer functionalisation (batch: KF6-2). As for the water sample almost no fluorescence is observed regardless of the surface functionalisation or treatment. This is evidence of the aptamer being properly immobilised on the nanopillar surface and capable of selectively binding a sample.

### 4.4.5 The effect of Tween20 in wash buffer

Is was additionally tested which role Tween20 played in the washing buffer. For all experiments described above Tween20 was added to the washing buffer to aid in removal of unbound molecules. This also includes the samples decribed where Tween20 was removed from the hybridisation. Figure 4.19 shows colormaps where Tween20 was removed from the washing buffer. Only samples which had been $O_2$ plasma cleaned prior to functionalisation was tested as these where shown to give the strongest signal. It is clearly seen that unspecific binding of cDNA is occuring for both cDNA and ncDNA samples without aptamer. As expected no fluorescence is seen for water samples. The strongest unspecific binding is however seen for ncDNA on aptamer functionalised samples. This is probably due to the fact that small fractions (maximum four bases) of the ncDNA strand will be complementary to the aptamer sequence. Therefore a minor degree of binding will occur. By adding Tween20 to the washing buffer the stringency is increased, which shows that the cDNA is much more strongly bound to the aptamer than the ncDNA. In general it is also seen that Tween20 in the washing buffer lowers the signal intensity, but the specificity is greatly enhanced.

One observation is also, that Tween20 might strongly affect the unspecific binding to silicon compared to gold. Since gold is already passivated with MCH, the majority of the unspecific binding will be to silicon. As seen from the fabrication process silicon is exposed to the liquid sample along the stem leading up to the metal head. It was recently proven by other group members that a strong hot spot exists right at the border between the metal head and the silicon stem [61]. This is a plausible explanation of why Tween20 was proven to be as effective as observed. Elimination of uspecifically bound molecules in hot spots will have tremendous influence on the Raman signal obtained.

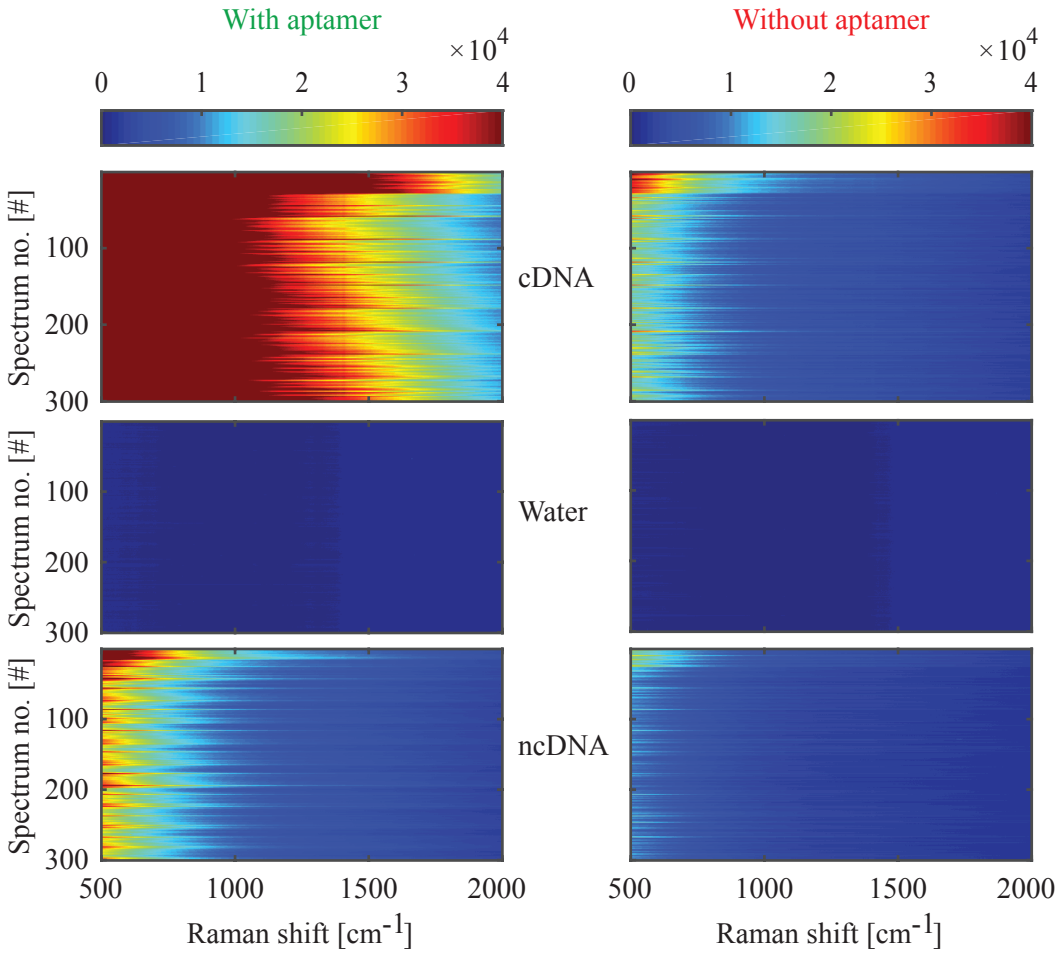


Figure 4.19: Colormaps of samples without Tween20 in washing buffer (batch: KF6-2). Is it clearly seen that unspecific binding of ncDNA occurs in these samples. The signal intensity is seen to be stronger compared to samples with Tween20 in the washing buffer (Figure 4.16-4.18). This shows that Tween20 effectively improves the selectivity of the aptasensor with respect to cDNA.

### 4.4.6 Conclusions to Experiment B

In this set of experiments it was established that aptamer is properly immobilised onto the gold nanopillar surface using the developed chemical functionalisation protocol. By inspecting the fluorescent signal from labelled cDNA it was demonstrated that specific binding occurs with respect to ncDNA. Negative controls (water samples) shows no background fluorescence. The effect of cleaning the gold substrates in $O_2$ plasma for 35 sec was clear: stronger signals are obtained when $O_2$ plasma is used. Likewise the presence of the non-ionic detergent Tween20 in hybridisation and washing buffers was found to greatly enhance the selectivity of the aptasensor.

C

## 4.5 Experiment C - Aptasensor development

Experiment B proved that selective hybridisation of cDNA to the immobilised aptamer on gold substrates was possible. Hence it was proved that aptamer was captured on the gold covered nanopillar surface and capable of forming bonds to other molecules. It was then investigated how different functionalisation parameters influenced the degree of functionaliation with aptamer and MCH. The aim was to get an in-depth understanding of each of the functionalisation steps in the protocol on the gold SERS substrate using only the SERS signal from each molecule. This type of analysis is generic to all aptamers and hence should provide a strong pathway for SERS aptasensor development.

### 4.5.1 Data analysis

During the course of the experiments it was discovered that additional analysis of the SERS spectra was required. Since 300 measurements were to be obtained for each sample it was important to develop a statistical approach to data analysis. Therefore a peak-fitting model was developed in collaboration with DTU Compute. The aim of this model was to enable statistical analysis of peak position and peak height in a given spectral window. Compared to the previously developed NMF analysis the peak-fitting model only analysed a small spectral window where a peak was expected to be present. This type of analysis could be conducted on the samples presented below since a positive signal was expected for almost all measured spots. This was expected since the chemical functionalisation of aptamer and MCH was to be uniformly covering all nanopillars, which is in great contrast to the NMF model that has its merits within identifying rare, specific spectra in a large ensemble.

#### Peak-fitting model

Peak-fitting was achieved by decomposing a Raman spectrum into several components. A spectrum was modelled as the additive contribution of peak distributions, background signal and measurement noise given by

$$f(x) = \sum_{i=1}^{N_p} A_i p_i(x) + b(x) + \epsilon, \tag{4.3}$$

where $f(x)$ is the measured spectrum, $x$ is the Raman shift wavenumber, $N_p$ is the number og peaks, $p_i(x)$ is the peak model for the $i$'th peak, $A_i$ is the amplitude of the $i$'th peak, $b(x)$ is the background model and $\epsilon$ is the measurement noise. For spectral peaks in vibrational spectroscopy a pseudo-Voigt function is commonly used [73]. It consists of a linear combination of

Gaussian ($G$) and Lorentzian ($L$) shaped curves defined as [76]

$$p(x, x_0, \omega, \eta) = \eta L(x, x_0, \omega) + (1 - \eta)G(x, x_0, \omega), \tag{4.4}$$

where $\omega$ is the width of the peak and $0 < \eta < 1$ is a shape parameter. The Lorentzian curve is defined as

$$L(x, x_0, \omega) = \frac{1}{1 + \frac{(x-x_0)^2}{\omega^2}}, \tag{4.5}$$

which accounts for the response from vibrational states of a molecule, whereas the Gaussian curve, defined by

$$G(x, x_0, \omega) = \exp\left(-\frac{\ln(2)}{\omega^2}(x - x_0)^2\right), \tag{4.6}$$

accounts for vibrational noise. The background model was a linear correction in the spectral window analysed and the measurement noise was assumed normally distributed. In order for Bayesian inference to be eligible prior distributions of the parameters must be given. Suitable and flexible choices are

$$A \sim \Gamma(A_a, A_b), \tag{4.7}$$
$$x_0 \sim N(\mu_0, \sigma_0), \tag{4.8}$$
$$\omega \sim \Gamma(\omega_a, \omega_b), \tag{4.9}$$
$$\eta \sim \beta(1, 1), \tag{4.10}$$

where $\Gamma$ is the gamma distribution, $N$ is the normal distribution and $\beta$ is the beta distribution. A Metropolis Hastings sampling algorithm [77, 78] was used for model inference with $10^5$ iterations and a burn-in of $5 \times 10^4$ iterations. An example of a fitted peak is shown in Figure 4.20, where it is seen that the model accurately fits to the peak within the measurement noise. The linear background is displayed and aid the model to obtain true spectroscopic peaks.

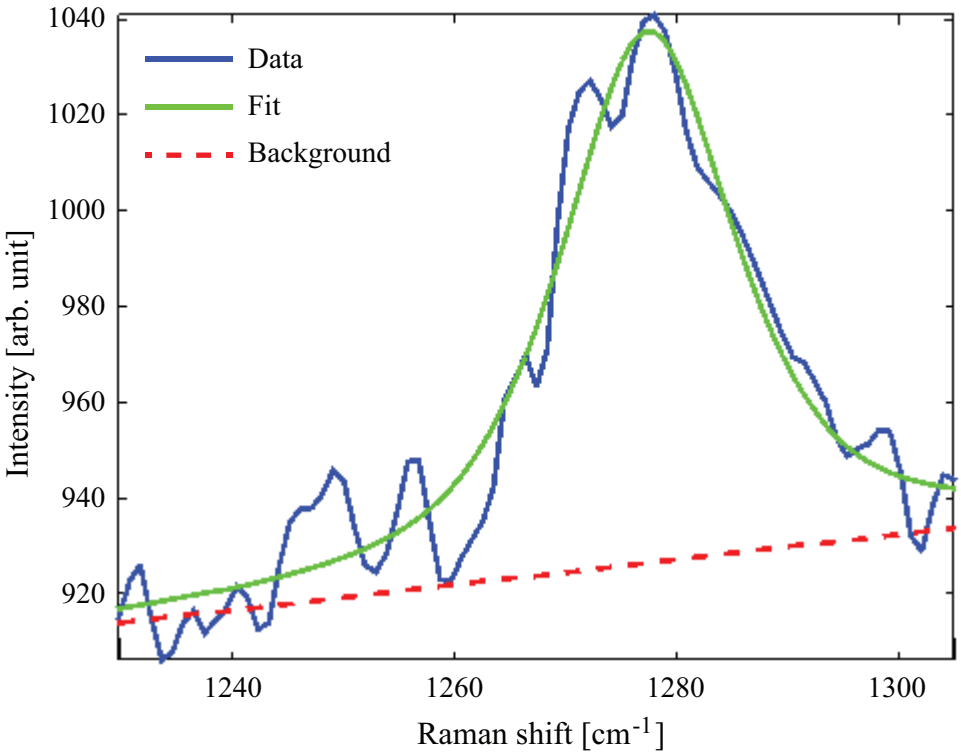


Figure 4.20: Example of peak-fitting to a single peak. The model is seen to accurately describe the data within the measurement noise given a linear background in a spectral window.

### 4.5.2 Protocol

The protocol for chemical functionalisation of gold nanopillars with aptamer and MCH is described below. Based on the experience gained from Experiment B a 35 sec $O_2$ plasma cleaning procedure was implemented. No other changes were made to the functionalisation protocol.

1. **Aptamer pre-treatment**
   (a) Prepare 100 µl 5 µM aptamer solution in $H_2O$.
   (b) Prepare 100 µl 500 µM TCEP·HCl solution in $H_2O$.
   (c) Mix 100 µl TCEP solution into the aptamer solution and incubate for 60 min at room temperature.
   (d) Purify on Illustra MicroSpin G25 columns.
   (e) Add 300 µl assay buffer to the mix immediately before immersion of the SERS substrate.

   The final volume is 500 µl, which is sufficient for full immersion of several 4x4 mm SERS substrate in individual 500 µl microtubes. The final aptamer concentration is 1 µM.

2. **Substrate pre-treatment and aptamer functionalisation**
   (a) Clean the substrate by 35 sec exposure to $O_2$ plasma.
   (b) Immerse the substrate in 99 % ethanol for 3 min.
   (c) Immerse the substrate $H_2O$ for 3 min.
   (d) Transfer into the aptamer/TCEP solution and incubate for 0-240 min at room temperature.

3. **MCH blocking**
   (a) Transfer the substrate directly into MCH solution (0-2000 µM in $H_2O$) and incubate for 0-120 min.
   (b) Dip quickly for 2 sec in $H_2O$ to remove unbound molecules and prevent salt aggregation on substrate. Repeat once.
   (c) Leave the substrate to dry.

   Once the substrate is dry Raman measurements can be obtained.

### 4.5.3 Raman acquisition settings

The settings for Raman acquisition listed in Table 4.4 was used. The only change compared to Experiment B is the increase in exposure time from 0.1 to 1 second. This was required since the molecules investigated did not exhibit as strong Raman activity as the DY776 fluorophore. All measurements were acquired in a 30x10 point mapping with 2 µm step size in both directions.

Table 4.4: Raman acquisition settings for Experiment C.

| Parameter | Setting |
|---|---|
| Wavelength | 780 nm |
| Estimated laser spot size | 1.6 µm |
| Power | 0.1 mW |
| Magnification | 50x |
| Exposure time | 1 sec |
| No. of exposures | 1 |
| Baseline correction | None |

### 4.5.4 Experimental results

#### Pure DNA aptamer spectrum

In order to investigate the interplay between aptamer and MCH their respective 'pure' spectra had to be obtained. Figure 4.21 shows the average spectra ($n = 300$) obtained from varying aptamer incubation time on cleaned ($O_2$ plasma, ethanol and water treatment) SERS substrates (batch: KF7-1). The 'background' signal was obtained on a cleaned chip that was allowed to dry after the water step.

The background (0 min DNA) spectrum is clearly distiguished from the functionalised spectra, in that no peaks are seen. Even 5 min incubation in DNA is enough to obtain an average spectrum with most of the characteristics seen for the longest incubation time (240 min). One difference is however the peak at 1280 $cm^{-1}$, which seem to be the most well defined peak when considering the peak height compared to the width. For 5 min this peak is not as prominent in the spectrum compared to other incubation times, which might suggest a low degree of aptamer bound to the surface. The spectra of 240 min is shown in Figure 4.22, where the strongest peaks are highlighted.

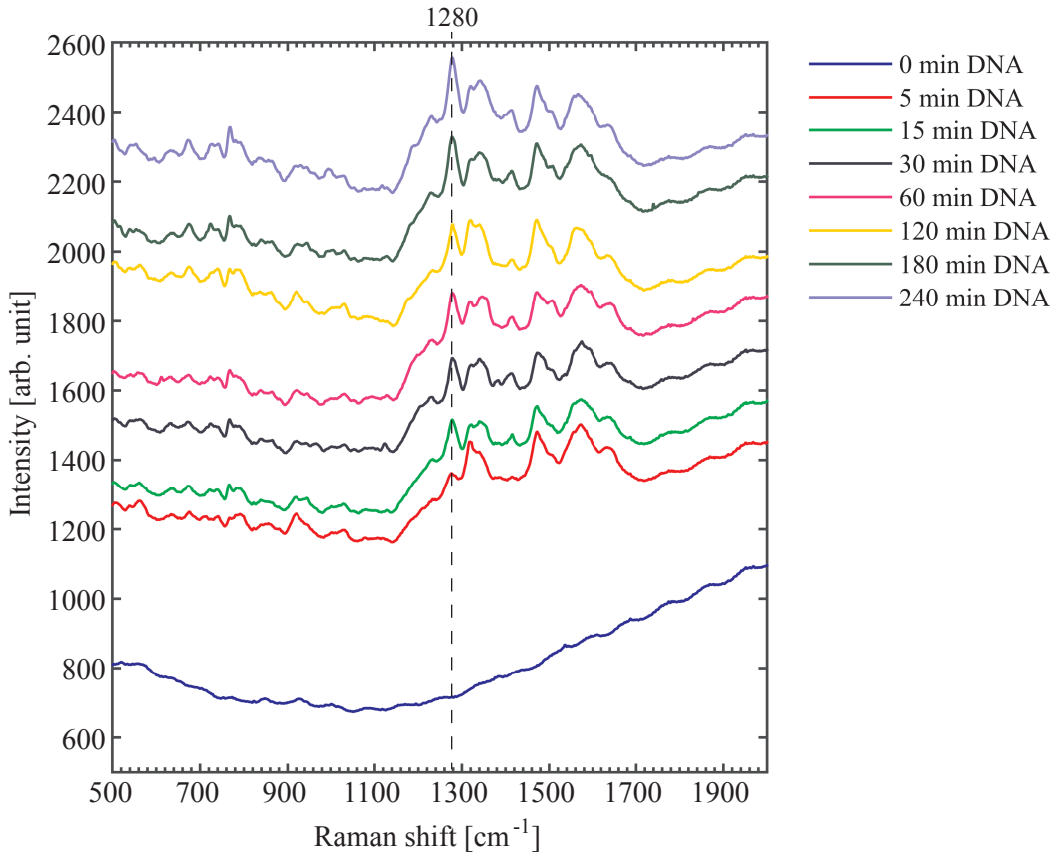


Figure 4.21: Average spectra of varying aptamer incubation time for a constant concentration of 1 µM (batch: KF7-1). It is seen that a clear signal is seen after only 5 min of incubation. Incubation for longer time increases the sharpness of the peaks - especially 1280 $cm^{-1}$. This peak was used as an indication of aptamer immobilisation.

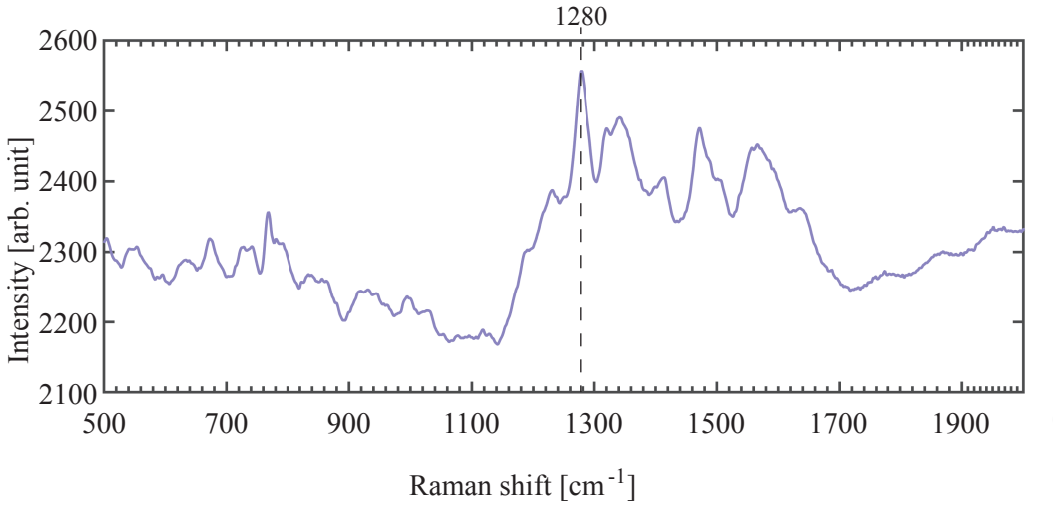


Figure 4.22: Average spectrum of 240 min of 1 µM aptamer (batch: KF7-1). The sharpest peak is clearly seen at 1280 $cm^{-1}$, but the region from 1100 $cm^{-1}$ to 1700 $cm^{-1}$ shows multiple weaker peaks.

It should be observed that the region from approximately 1100 $cm^{-1}$ to 1700 $cm^{-1}$ exhibits the strongest Raman activity, but especially the 1280 $cm^{-1}$ peak is of interest. This is due to the fact that in later functionalisation steps this peak was a strong indicator of immobilised aptamer.

To obtain a clearer visualisation and understanding of the data the peak fitting model was applied on the data sets (8x300 spectra). The model fitted a peak to the region 1230-1330 $cm^{-1}$ for every single spectrum, using no predetermined priors. This means that the model could fit any peak in the given spectral window. By allowing the model to determine the peak freely no user influence is contaminating the results. Both the centre position of the peak and the peak height was fitted. A combined plot of these parameters are shown in Figure 4.23. The histograms reveal interesting features of the data shown in the average spectra of Figure 4.21 for the 1280 $cm^{-1}$ peak. It is seen that a fairly broad distribution of both peak position and peak height is obtained from the fitting model. These histograms carry information otherwise unobtainable by simple averaging. It should be noted that the model struggles to fit to a specific peak for 0 min incubation, which is demonstrated by the very narrow distribution of intensities (towards low intensities) and the almost uniform distribution of peak position. This is also evidence of the model not being forced to fit peaks to a pre-determined Raman shift. Once the incubation time is increased the 1280 $cm^{-1}$ peak is beginning to appear in most of the 300 spectra fitted. Even after 5 min incubation in aptamer solution, there is a clear tendency of a peak position around 1280 $cm^{-1}$, but with relatively low peak intensity. Increasing the incubation time to 15 min yields a more narrow

distribution of peak positions with a higher intensity. This is interpreted as more aptamer being adsorbed on the nanopillar surface. Beyond 15 min incubation seems to yield no change in distribution of the peak parameters.

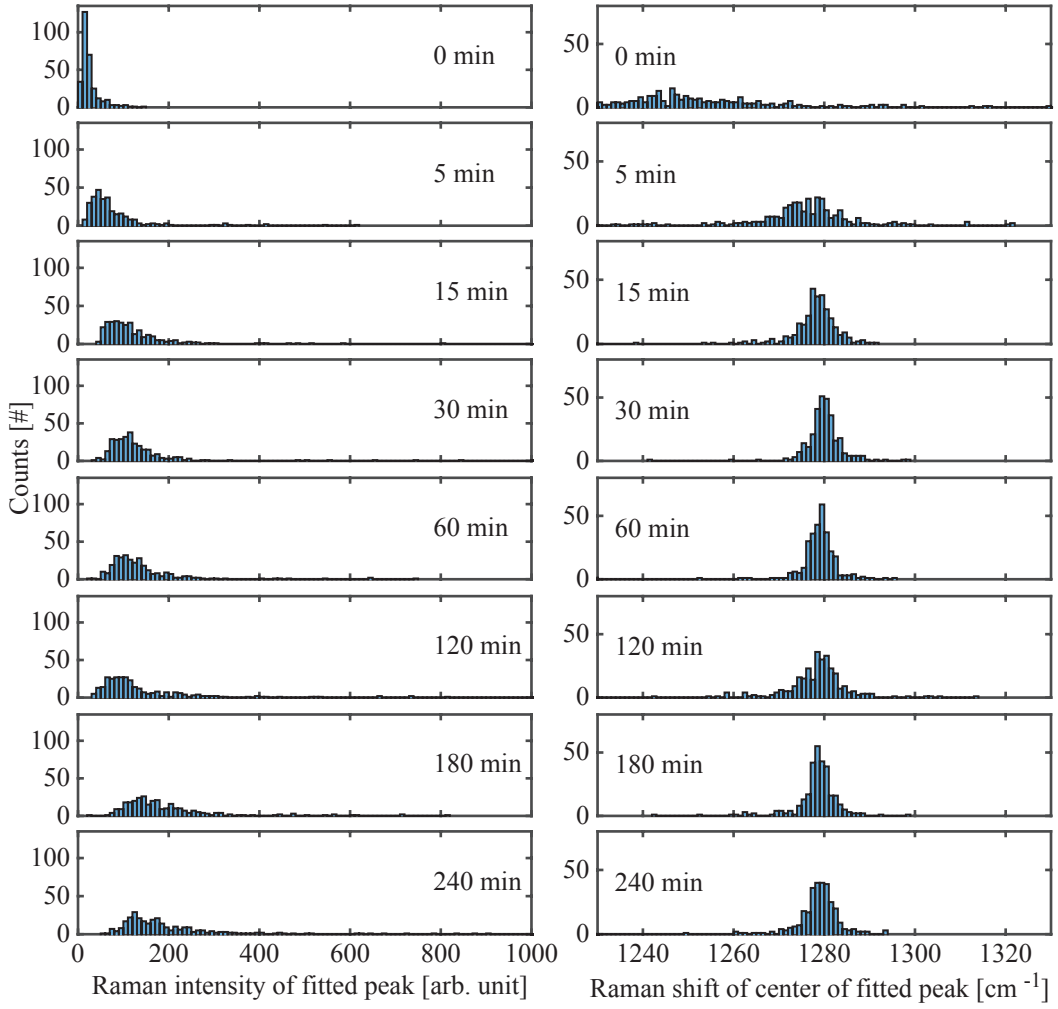


Figure 4.23: Histograms of the 1280 $cm^{-1}$ peak for varying aptamer incubation time (batch: KF7-1). As the time is increased the distribution of the centre of the fitted peaks become very narrow around 1280 $cm^{-1}$. Given that no priors were used in the fitting model it is seen that in almost all of the $n = 300$ spectra obtained for each incubation time (except 0 and 5 min) there exist a peak at 1280 $cm^{-1}$.

Even though a strong and specific signal was seen after only 15 min of incubation, it was decided to incubate in aptamer solution for 120 min. This was to ensure that the thiol-gold bond had enough time to be formed. When the aptamer first comes in contact with the substrate a physical adsorption happens due to electrostatic interactions. This means, that aptamer is present on the surface after this short incubation time, however a stable, covalent-like bond between gold and the thiol group of the aptamer has not yet been established. Since this is a crucial step in obtaining a selective sensor, it was decided to allow a longer, sufficient incubation time. This is also consistent with a study by Georgiadis et al. on a flat gold surface. They demonstrate that most of the thiolated DNA is attached within 120 min [79].

### Pure 6-mercapto-1-hexanol spectrum

Spectra of pure MCH was acquired on batch KF6-3. Initially the concentration of MCH was varied while the incubation time was kept at 60 min. The results are shown in Figure 4.24, where it is observed that not much change in the signal is seen from the lowest concentration investigated (50 µM) compared to the highest (4000 µM). However a distinct spectrum from MCH was obtained. The peaks were very reproducible as shown by peak fitting of the double peak at 1060 $cm^{-1}$ and 1085 $cm^{-1}$ (data shown in Appendix A.7).

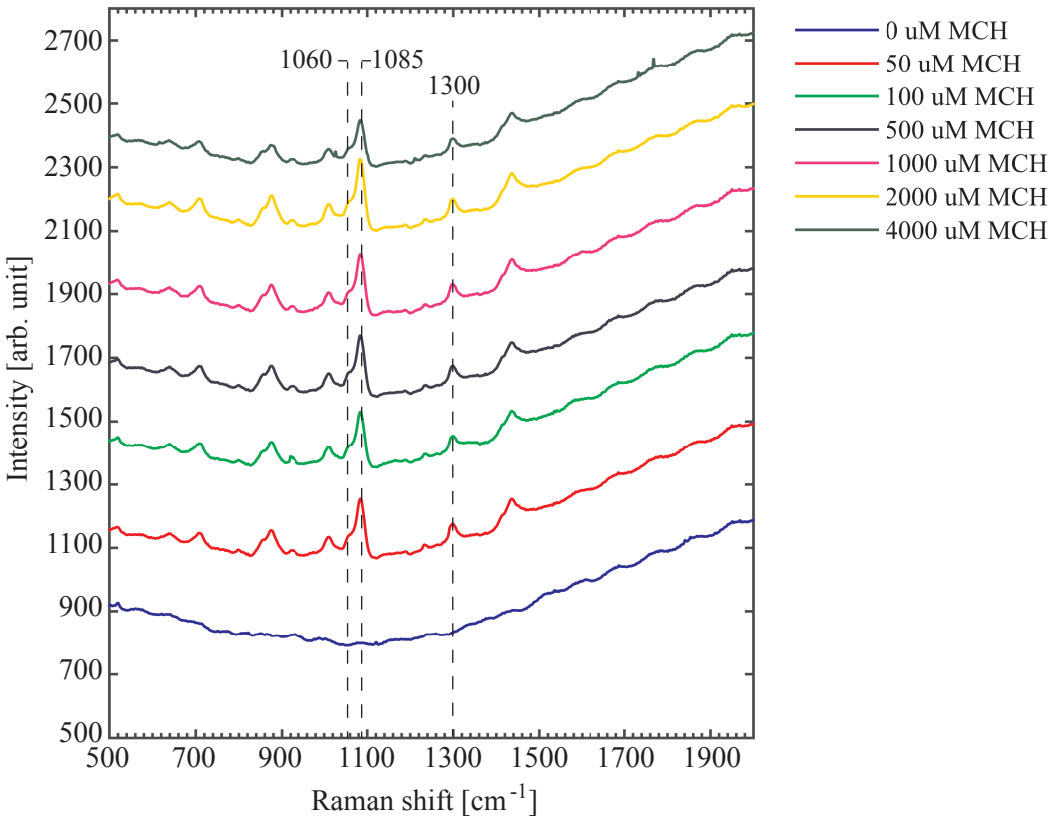


Figure 4.24: Average spectra of MCH with varying concentration (batch: KF6-3). It is seen that even the lowest tested amount of MCH (50 µM) yields as good a spectrum as the highest (4000 µM). The characteristic double peak at 1060 $cm^{-1}$ and 1085 $cm^{-1}$ was later used for determination of succesful MCH immobilisation, since it does not overlay any peak of the aptamer signal.

Figure 4.25 shows a close up of the 50 µM MCH spectra, where the most dominant peaks have been highlighted. It is seen that the strongest peak it in fact a double peak at 1060 and 1085 $cm^{-1}$. This double peak was later seen to be very distinct in identifying MCH immobilisation. Another peak characteristic of MCH is seen at 1300 $cm^{-1}$, which is very close to the 1280 $cm^{-1}$ aptamer peak. These peaks might interfere with each other, making it challenging to analyse.

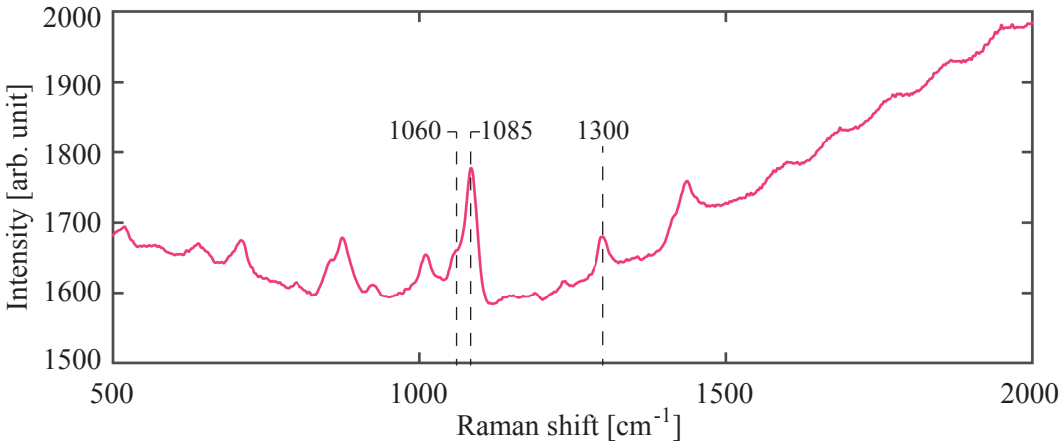


Figure 4.25: Average spectrum of 1000 µM MCH (batch: KF6-3). The characteristic double peak is clearly seen to be the strongest, but the minor peak at 1300 $cm^{-1}$ might have an influence on the strong 1280 $cm^{-1}$ aptamer peak.

Since the high concentration spectra yielded no difference in signal, spectra of pure MCH at lower concentration was acquired on a newer batch of chips (KF8-1). The average spectra are shown in Figure 4.26. This particular batch had good enhancement of Raman signals, but a much worse background spectrum compared to the previous batches. The reason for this sudden increase in background spectrum is unknown, but could be due to several factors relating to the fabrication process. Since the fabrication machines are constantly being used and maintained it is impossible to keep track of possible contaminating factors that might have been introduced since last batch process. Two likely contaminations arise from either the RIE process, where previous users might have processed wafers with various materials present, or from the metal deposition, where the piece of metal is exchanged regularly. Both of these processes might introduce contaminating molecules on the surface, which is visible in the background spectrum.

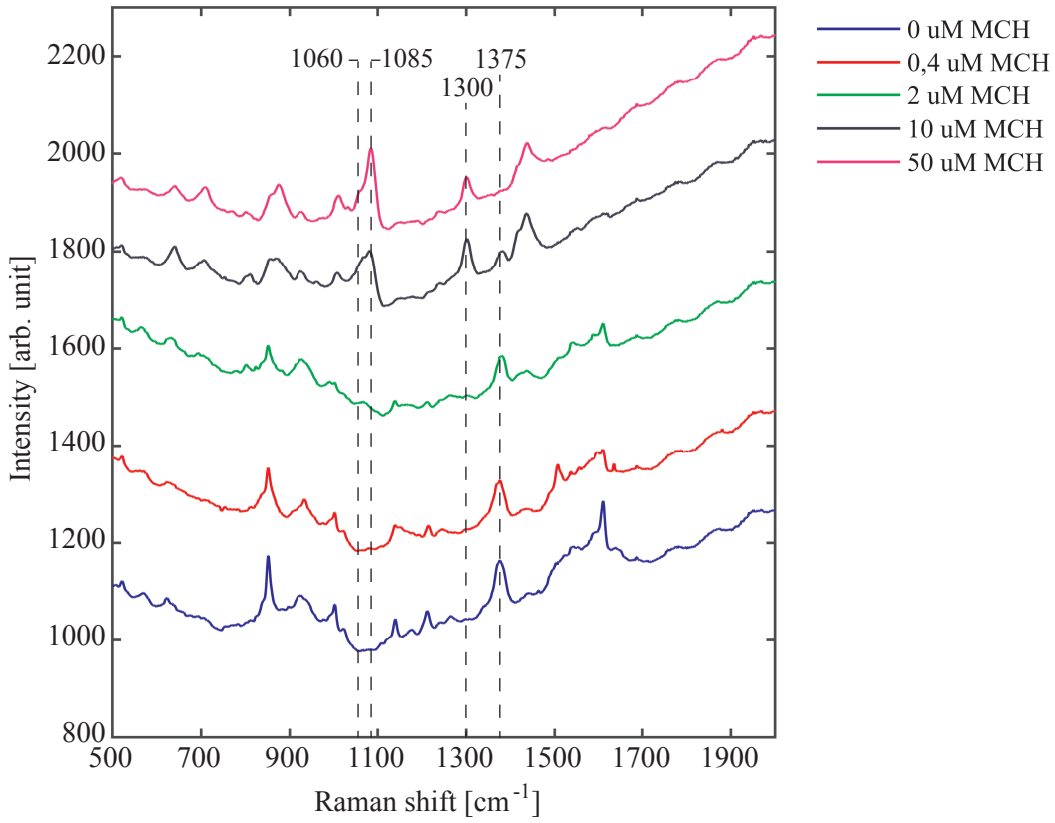


Figure 4.26: Average spectra of MCH with varying concentration. The range of MCH concentration was lower than the previous experiment, but conducted on a newer batch of chips (KF8-1). A strong background signal is seen for low concentration MCH, but this is supressed when the amount of MCH is increased.

Despite the background issue the experiments provided very useful information. As the concentration is increased several phenomena appear. Firstly at low concentration (0.4-2 µM) the intensity of the background signal is diminished without any specific MCH peaks appearing. At 10 µM concentration the MCH peaks are clearly seen, but one small peak (1375 $cm^{-1}$) from the background is still present. The appearance of the MCH signal indicates that the amount of molecules on the surface is becoming larger. Since MCH is capable of forming SAMs it is assumed that this occurs roughly at this concentration on bare gold nanopillars. It should also be noted that for the 50 µM concentration no peaks from the background is seen. This is evidence of MCH being capable of suppressing molecules on the surface. Since MCH is applied after the aptamer incubation, no specific set of parameters could be chosen at this point, since it might change when combined with aptamer. However this experiment yielded estimates of where interesting phenomena might occur together with valuable information regarding the pure MCH spectra.

### Effect of MCH on aptamer spectrum

Investigation of the interplay between aptamer and MCH was performed on substrates with 120 min incubation of aptamer on batch KF7-1. After incubation the substrates were dipped twice in $H_2O$ in order to remove unbound molecules. Initially the incubation time of MCH was kept constant at 60 min, while the concentration was varied. The resulting average spectra can be seen in Figure 4.27. The concentration range was chosen based on the previous experiments with MCH on cleaned chips (no aptamer). From this it was expected that at approximately 10 µM a change in signal would be observed. The average spectra show the appearance of the MCH signal at 50 µM instead. This change is backed up by the peak fitting model (see Figure 4.28), where there is a clear appearance of a double peak at 50 µM. At lower concentration there is a tendency of a double peak, but the distribution of the centre of the fitted peak is very broad. The change in concentration of MCH before the specific peaks are seen (from 10 µM to 50 µM) is due to the influence of the aptamer. Since the aptamer has made a thiol bond to the gold covered nanopillars the MCH can not as easily suppress it compared to the background issue of batch KF8. It should be noted that increasing the MCH concentration does not yield a stronger MCH signal.

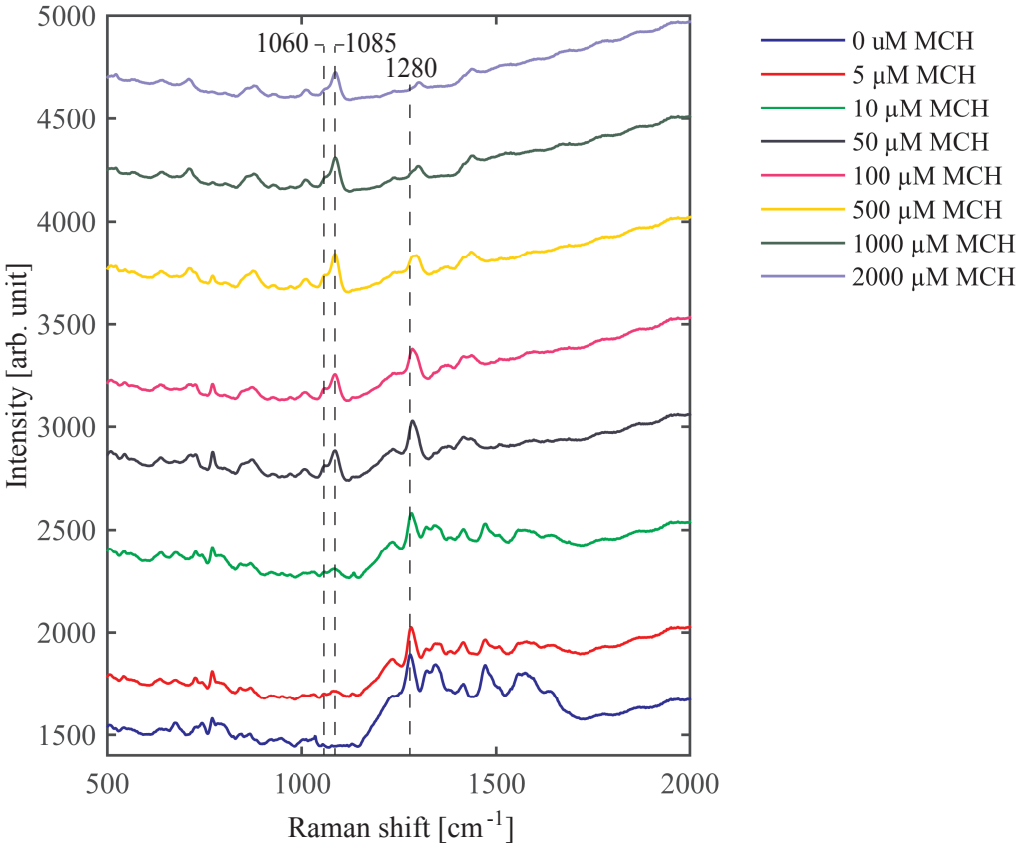


Figure 4.27: Average spectra of varying MCH concentration on aptamer functionalised chips (batch: KF7-1). At 50 µM the characteristic double peak of MCH is seen at 1060 $cm^{-1}$ and 1085 $cm^{-1}$. The 1280 $cm^{-1}$ aptamer peak is seen to diminish and shift towards higher wavenumbers as the MCH concentration is increased. Due to the importance of being able to see both peaks an MCH concentration of 50 µM was chosen for later experiments.

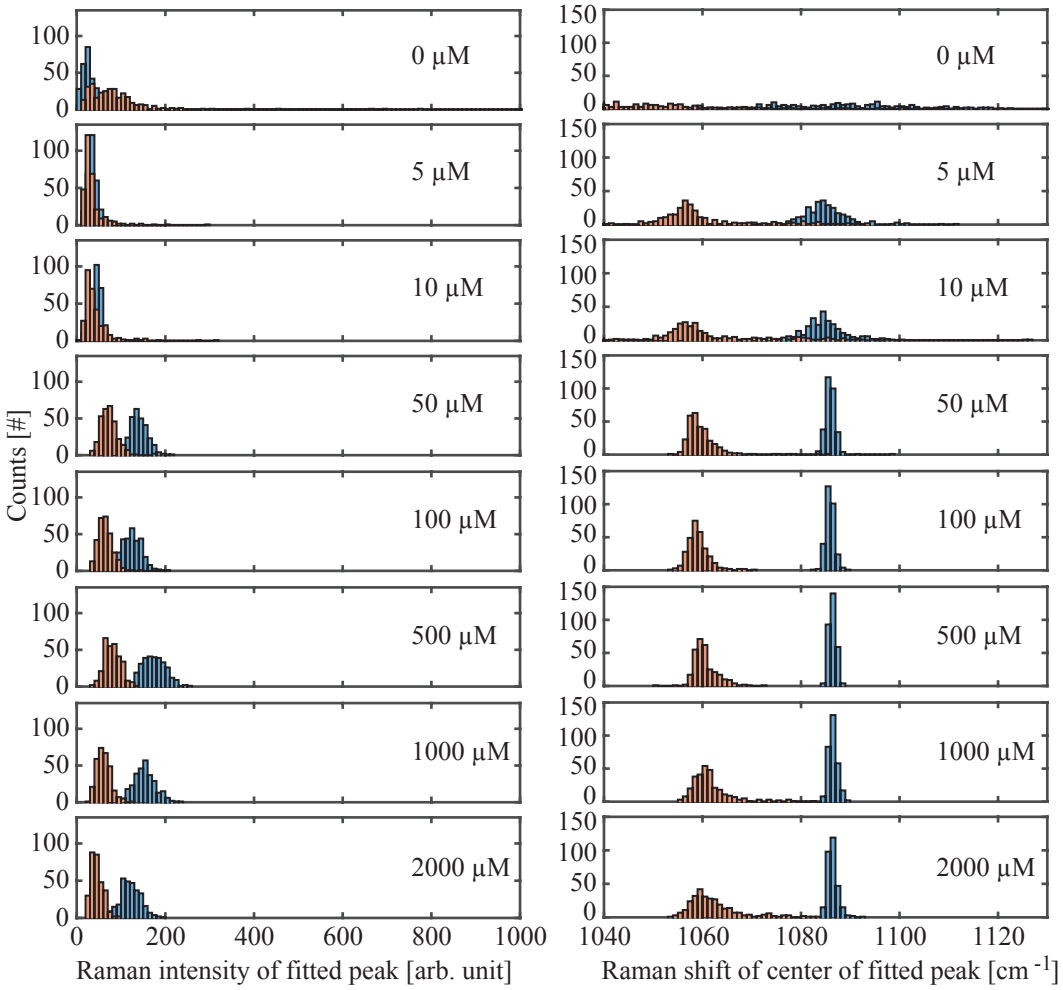


Figure 4.28: Histograms of MCH peaks varying MCH concentration (batch: KF7-1). There is a tendency of a double peak appearing already at the lowest concentrations tested. However the distributions of the fitted centres are very broad, whereas for 50 µM they are much sharper. Increasing the amount of MCH above 50 µM has no influence on the MCH peaks.

Inspection of the 1280 $cm^{-1}$ aptamer peak reveals an interesting trend: the strength of the peak seems to diminish and shifts slightly towards higher Raman shift when the MCH concentration is increased. The peak fitting model captures this phenomenon very well as shown in Figure 4.29. Here it is clearly seen that the peak is shifting from 1280 $cm^{-1}$ (pure aptamer) towards 1300 $cm^{-1}$ (pure MCH). When applying an increasing amount of MCH, the intensity of the fitted peak is also decreasing. The transistion in between actually consists of a double peak overlapping each other, but it is still easily seen when fitting only one peak. The double peak is very hard to distinguish from a single noisy peak, which would be troublesome for the model, if asked to fit two peaks in the range.

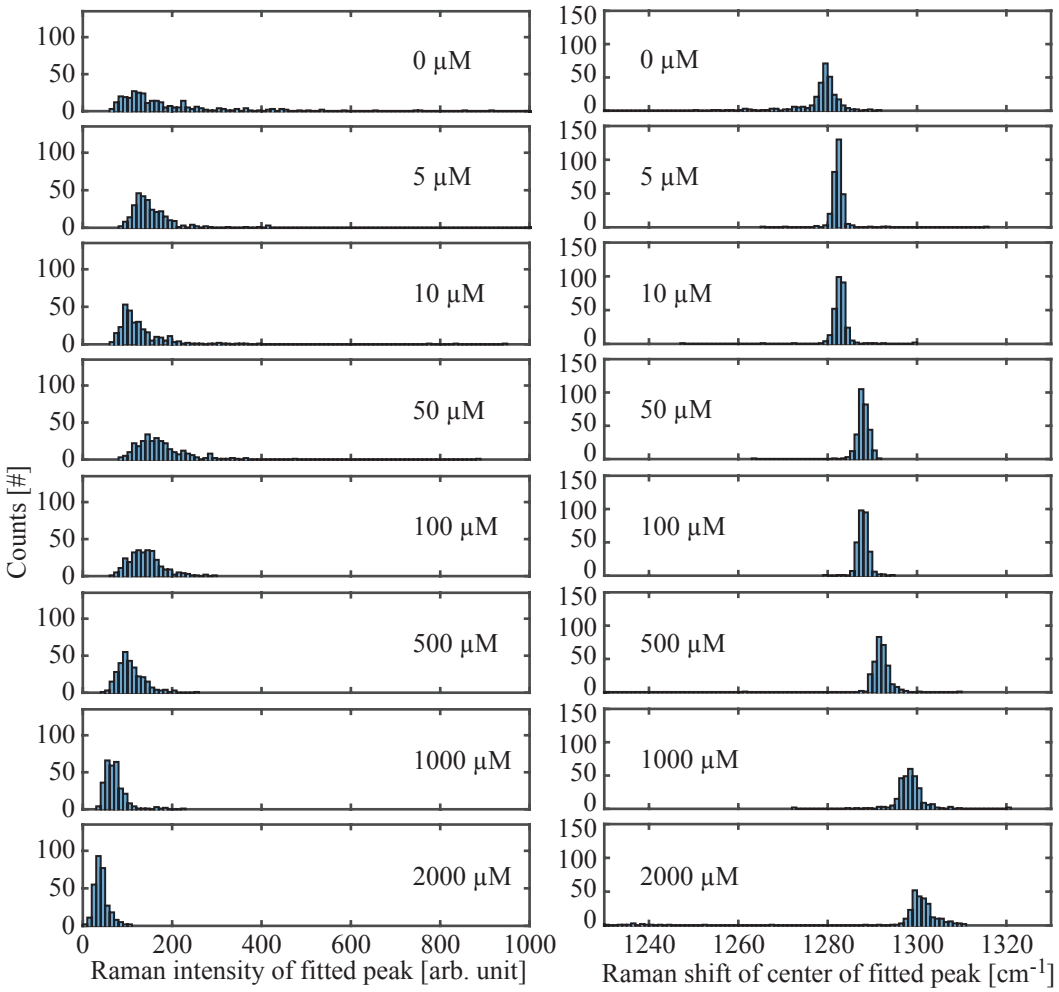


Figure 4.29: Histograms of the aptamer peak for varying MCH concentration (batch: KF7-1). A shift of the peak towards higher wavenumbers is clearly visible when the MCH concentration is increased. Simultaneously the peak intensity is decreased. At 50 µM the shift of the peak is still minor, yet observable, which indicates some, but not much, MCH have been immobilised on the nanopillars.

Since it is possible to see both the aptamer and the MCH peaks for 50 µM MCH it is recommended to proceed with this concentration. It is also evident from the histograms, that the aptamer peak almost conserves its attributes at this concentration. This concentration of MCH should be sufficient to prevent unspecific binding of target molecules to the gold surface, but it is still low enough not to remove most of the aptamer. When MCH forms SAMs on the gold surface it is capable of pushing other thiol bound molecules around the surface. Since it is a strict competition between MCH and the other molecule the MCH can eventually remove it from the surface in a ligand exchange reaction. Le Ru et al. [50] argues that being able to see unperturbed peaks from two individual molecules in one spectrum should be evidence of the molecules not interacting. This is important, since the functionality of the aptamer relies solemnly on the capability of folding in the proper manner. If the MCH interacts with some part of the aptamer, then it will be the $C_6$-linker, which is identical in length to MCH and has no influence on the folding of the aptamer. The 50 µM concentration chosen is vastly different from the initial 2000 µM previously used. Achieving the proper ratio between aptamer and MCH could be of significantly higher importance in label-free sensing, since the detection method relies on subtle changes in the SERS spectrum, which might be suppressed by an overflow of MCH.

It was then investigated how the incubation time of MCH for 50 µM concentration influenced the SERS spectra. The average spectra are shown in Figure 4.30, where the MCH double peak is seen after only 1 min incubation. This shows that MCH is very quick at adsorbing to the gold surface. However the uncertainty in the experimental handling makes the 1 min measurement point unreliable. The experiment was repeated (data shown in Appendix A.8) and here the MCH signal first appeared after 5 min. Hence it was deemed necessary for the MCH to have some time to attach to the surface. 15 min incubation was chosen, because this should allow sufficient time for MCH to properly bind to the surface, while still keeping the incubation time low. According to Georgiadis et al. [79] keeping the incubation time at a minimum greatly reduces desorption of DNA from the surface. In combination, the 50 µM 15 min incubation of MCH is significantly less than the initial 2000 µM 60 min incubation. The chosen parameters are also close to those reported by Pang et al. [66], where 40 µM MCH was incubated for 60 min on silver dendrites for a label-free SERS aptasensor.

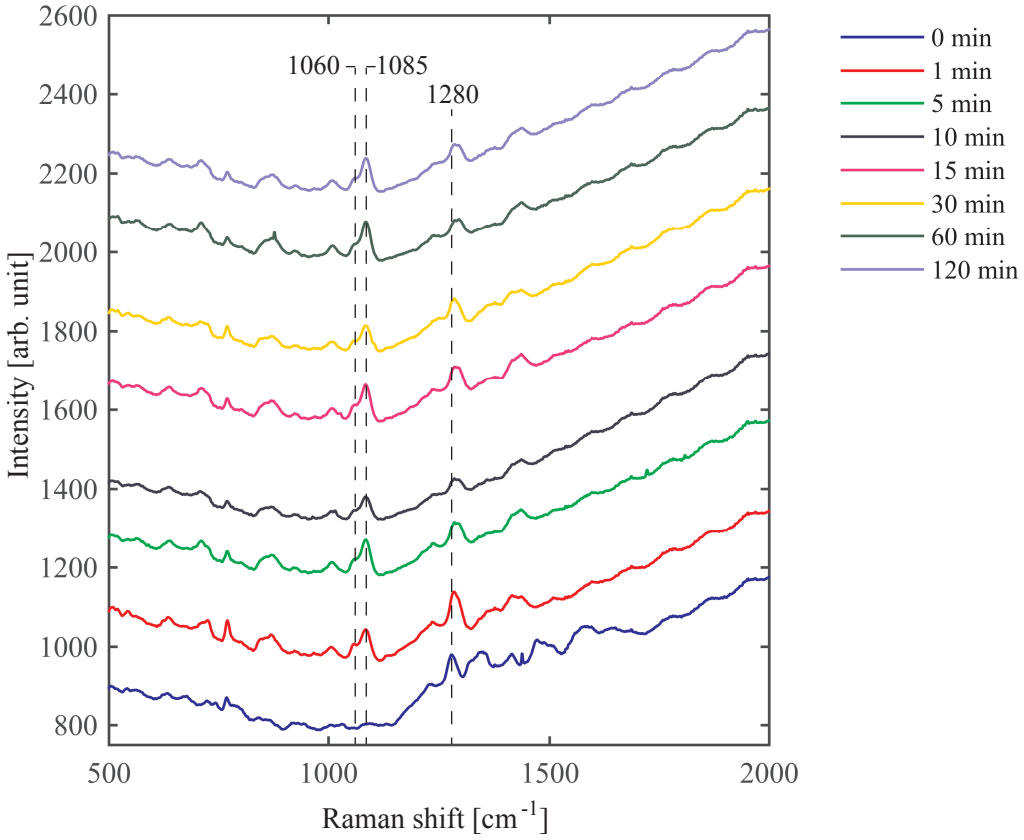


Figure 4.30: Average spectra of varying MCH incubation time on aptamer functionalised nanopillars (batch: KF7-1). After only 1 minu incubation the characteristic double peak of MCH is seen. Increasing the incubation time does not show any changes in the spectraum. However once the experiment was repeated the double first appeared after 5 min incubation. For this reason a prolonged 15 min incubation time was chosen for future experiments.

### 4.5.5 Conclusion to Experiment C

The interplay between immobilised aptamer and MCH was investigated directly via the Raman spectrum. Peak positions were analysed with the developed peak-fitting model to encompass for the large amount of data acquired. It was observed that DNA aptamer was quickly bound to the gold nanopillar surface by physical adsorption. However allowing sufficient time for the covalent-like thiol-gold bond to be formed was deemed nescessary. When applying MCH to block the remaining gold binding sites it was observed to remove aptamer from the surface by a ligand exchange reaction seen by a clear shift in peak position. By altering the concentration and incubation time of MCH it was possible to directly obtain proper functionalisation parameters, where both DNA aptamer and MCH peaks were visible in the obtained spectrum. This analysis is generic to all SERS aptasensors and can be applied regardless of the target in question.

### 4.5.6 Publications

#### Oral presentation at ICAVS8

The following abstract was accepted for an oral presentation at the 8th International Conference on Advanced Vibrational Spectroscopy (ICAVS-8) July 12-19th 2015 in Vienna, Austria. Briefly, it describes the application of the peak-fitting model to ensembles of SERS data for determination of optimal functionalisation parameters.

It can be found at:
`http://www.icavs.org/icavs8/images/program/Abstracts_Oral_web.pdf`

#### Article in Vibrational Spectroscopy

An article have been submitted as a proceeding of the ICAVS-8 conference to a special issue of 'Vibrational Spectroscopy'. This work covers more in-depth analysis of the ICAVS-8 conference abstract. Especially thorough analysis of the functionalisation parameters is given. **Review in progress**.

D

## 4.6 Experiment D - 17$\beta$-estradiol aptasensor

Based on the funcionalisation parameters obtained from Experiment C it was attempted to develop a sensitive SERS aptasensor towards 17$\beta$-estradiol. Aptamer incubation was kept at 120 min and MCH was applied at 50 µM for 15 min. Raman acquisition settings were identical to that of Experiment C.

### 4.6.1 Protocol

After immobilisation with aptamer and additional blocking with MCH, 17$\beta$-estradiol was incubated using the following protocol. It should be noted that the binding buffer of E2 aptamer #2 listed in Table 3.3 is [31]: 2 mM Tris–HCl, 10 mM NaCl, 0.5 mM KCl, 0.2 mM $MgCl_2$, 0.1 mM $CaCl_2$, 5 % ethanol. 0.1 % Tween20 was added to eliminate unspecific binding as proven in Experiment B.

1. **Aptamer folding**
   Start this protocol right after MCH blocking described in Experiment C.
   (a) Immerse substrate directly from MCH solution into $H_2O$ for 3 min.
   (b) Immerse into 2 M UREA and 7.5 mM EDTA in $H_2O$ for 3 min.
   (c) Immerse into $H_2O$ for 3 min. Repeat once.
2. **Target binding and rinsing**
   (a) Prepare 500 nM 17$\beta$-estradiol in binding buffer + 0.1 % Tween20.
   (b) Immerse substrate into solution and incubate for 60 min.
   (c) Transfer directly to pure binding buffer to remove unbound target molecules. Incubate for 15 min.
   (d) Dip quickly for 2 sec in $H_2O$ to prevent salt aggregation on substrate. Repeat once.
   (e) Leave the substrate to dry.

   Once the substrate is dry Raman measurements can be obtained.

### 4.6.2 Experimental results

#### Pure 17$\beta$-estradiol spectrum

Spectrum of pure 17$\beta$-estradiol in ethanol was obtained. This was done on cleaned chips from batch KF7-1 by immersion in the pure 17$\beta$-estradiol solution (0-1000 nM in ethanol) for 60 min. The initial results with high concentration is shown in Figure 4.31. As previously seen the background signal for

this batch was very good, however the average spectra does not reveal many sharp peaks. A few minor peaks at 808 $cm^{-1}$ and 1540 $cm^{-1}$ is though seen. Histograms from peak-fitting to the 808 $cm^{-1}$ peak are shown in Appendix A.9.

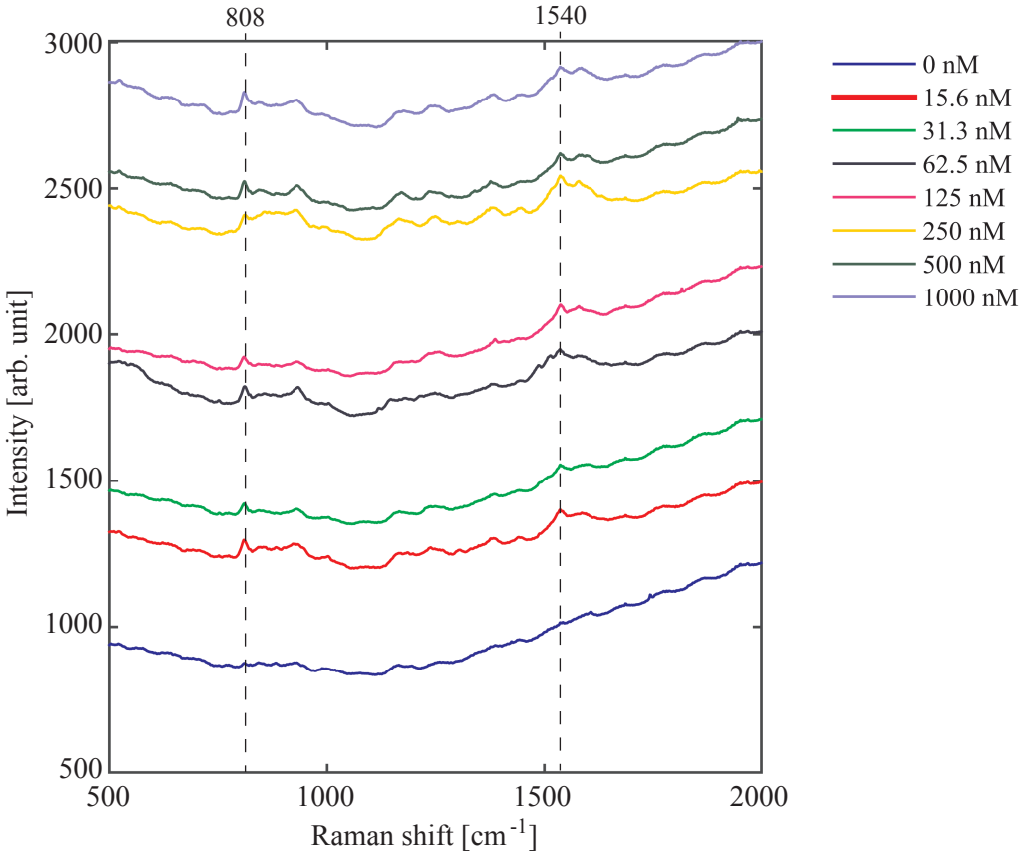


Figure 4.31: Average spectra of 17$\beta$-estradiol for varying concentrations (batch: KF7-1). No strong peaks are observed, but a minor peak at 808 $cm^{-1}$ and 1540 $cm^{-1}$ are showing. The spectra are still clearly distinguishable to the background spectrum.

Figure 4.32 shows the 15.6 nM data only where the background signal have been subtracted, which more clearly display the two peaks. However the 1540 $cm^{-1}$ peak seems to be a mixture of several peaks, which might be troublesome to analyse in combination with the aptamer and MCH signal. Especially the aptamer signal could have significant influence on the visibility of this peak, as the average spectrum of aptamer showed SERS activity in the 1100 $cm^{-1}$ to 1700 $cm^{-1}$ range. Despite this these data on cleaned chips show that the peaks are detectable to the lowest tested concentration (15.6 nM) on this batch of nanopillars.

Two other batches (KF7-2 and KF8-1) of nanopillars were used to investigate the spectra from 17$\beta$-estradiol at lower concentrations. The average spectra

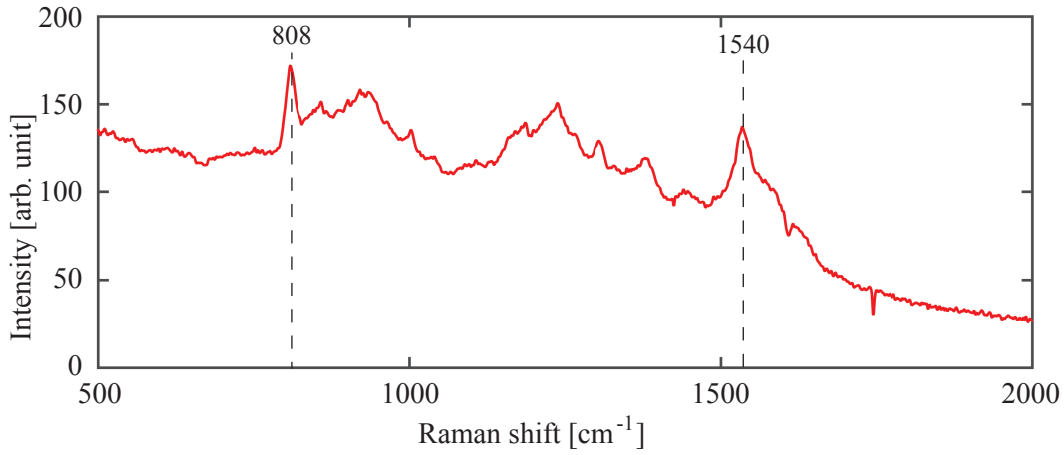


Figure 4.32: Average spectrum of 15 nM 17$\beta$-estradiol in ethanol on cleaned chips (batch: KF7-1). Here the background have been subtracted in order to better visualise the small peaks occuring. It should be noted that the 808 $cm^{-1}$ peak is much sharper than other peaks seen, which might prove useful for further detection using aptamer and MCH.

from batch KF7-2 is shown in Figure 4.33. Here it is observed that even 15 pM 17$\beta$-estradiol could be detected. This result was however not repeatable. This was probably mainly due to the background issue related to batch KF8-1. When the experiment was performed on this batch of chips, it became impossible to separate the background from the 808 $cm^{-1}$ peak of 17$\beta$-estradiol (data shown in Appendix A.10). Especially the peak fitting model had troubles in distinguishing the actual 17$\beta$-estradiol peak from the background (data not shown).

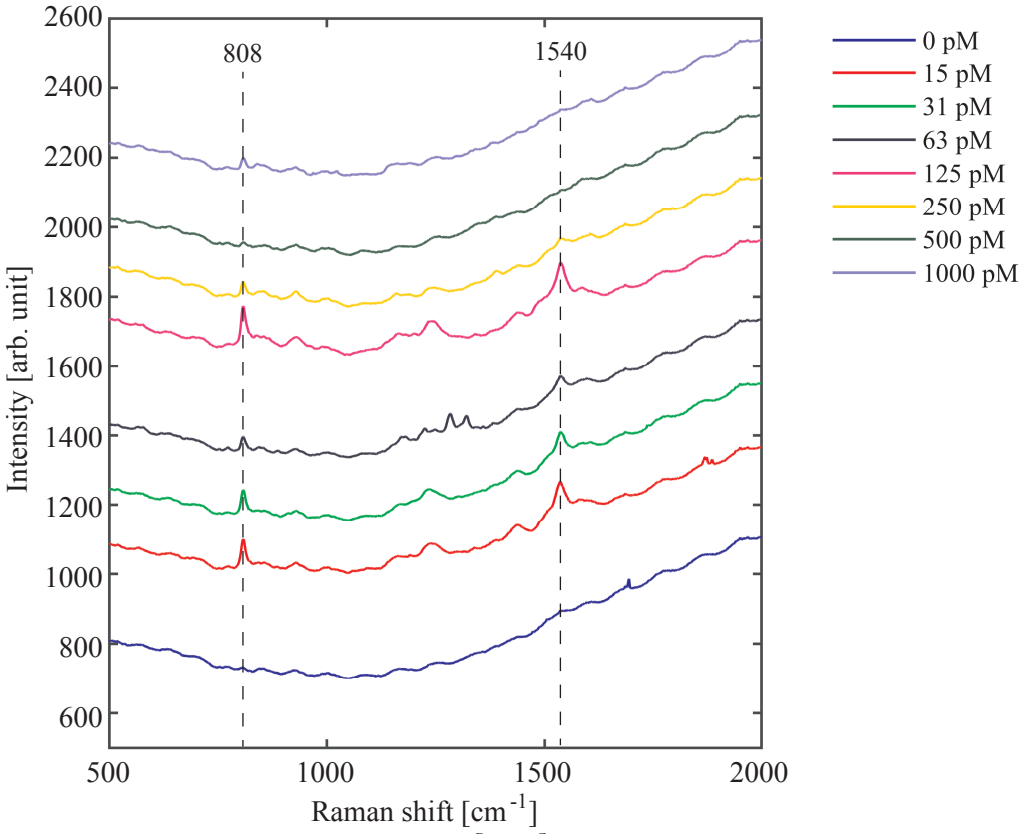


Figure 4.33: Average spectra of pure 17$\beta$-estradiol in ethanol on cleaned chips (batch KF7-2). The 808 $cm^{-1}$ peak is clearly visible in the lowest concentration of 15 pM. These experiments could not be repeated due to enhanced background on a new batch of SERS substrates.

### Label-free 17$\beta$-estradiol detection

Label-free detection of 17$\beta$-estradiol was then attempted using the developed functionalisation parameters for aptamer and MCH immobilisation on batch KF7-2. Target incubation time in binding buffer was set to 60 min at 500 nM, which should be sufficient for aptamer-target binding [69]. Average spectra are shown in Figure 4.34, where the left column is without and the right column is with 17$\beta$-estradiol. Four different cases were tested:

1. Blank, cleaned nanopillars.
2. With aptamer only (no MCH).
3. With MCH only (no aptamer).
4. With both aptamer and MCH.

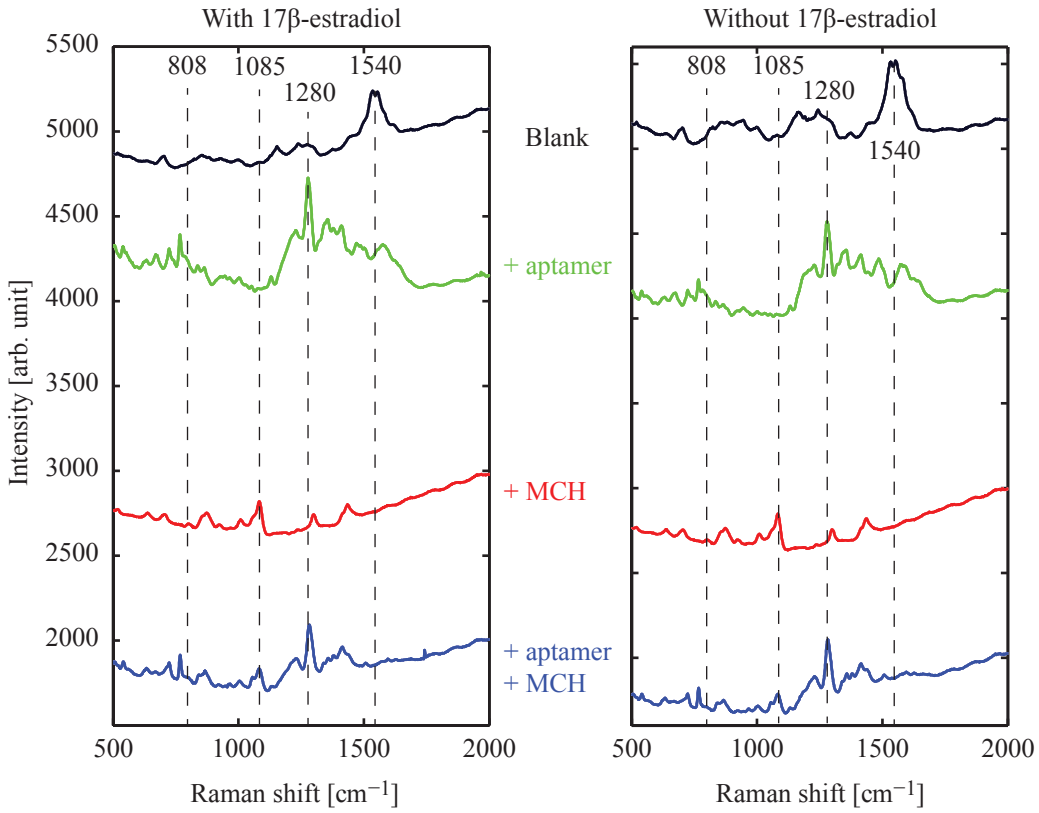


Figure 4.34: Average spectra of 17$\beta$-estradiol detection for different types of functionalisation (batch: KF7-2). As seen no particular peaks are arising when the chips are exposed to 17$\beta$-estradiol for either of the experiments. The background signal seen in the blank samples is fully suppressed by the functionalisation.

As can be seen the average spectra yielded no visual change in the signal for neither of the four cases tested when 17$\beta$-estradiol was present. The peak-fitting model was set to investigate the 808 $cm^{-1}$ peak observed for pure 17$\beta$-estradiol. However since the aptamer has a minor peak around 765 $cm^{-1}$ the model struggled to find a stronger peak at 808 $cm^{-1}$ (data not shown).

Since the capture of a target should inflict conformational changes to the aptamer, the aptamer peak at 1280 $cm^{-1}$ was investigated by the model. Figure 4.35 shows scatterplots of the fitted peaks. The horizontal axis is the peak position, the vertical axis is peak intensity and the distributions are shown in the histograms. Only the four data sets for chips with aptamer are shown (with/without MCH and 17$\beta$-estradiol).

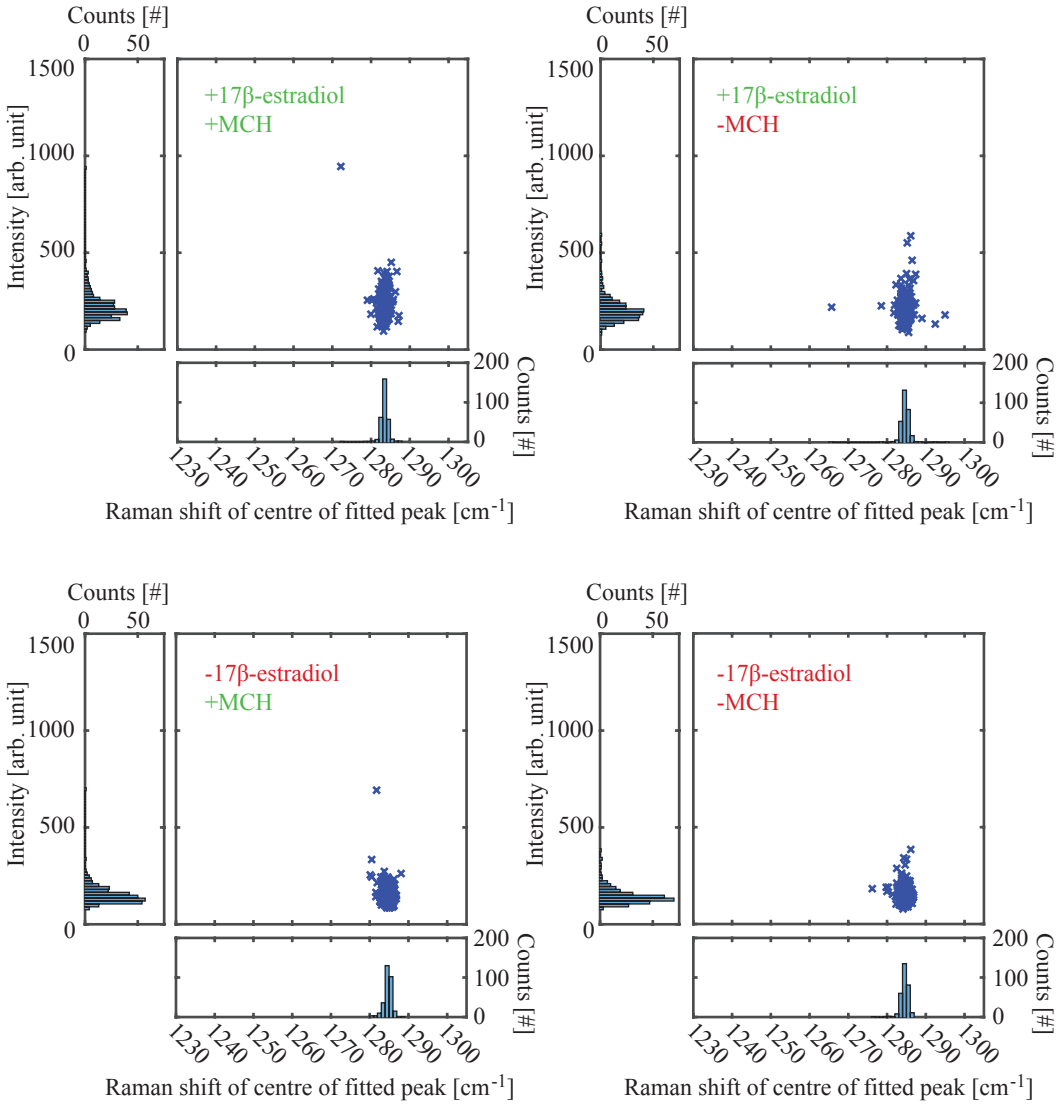


Figure 4.35: Scatterplots of the 1280 $cm^{-1}$ aptamer peak for varying functionalisation (batch: KF7-2). A slight change (elongation of the 2D distribution) in the intensity profile can be observed when 17$\beta$-estradiol was tested. This could originate from the aptamer changing its 3D configuration upon capture of the target. However the trend could not be reproduced.

As can be seen from the scatterplots the distributions of fitted peaks are very narrow. Most peak lies close to each other, which means that in all of the spectra obtained the characteristic peaks can be seen. This is evidence of a very uniform functionalisation with aptamer and MCH. A slight change towards higher intensities in the intensity distribution might be seen when 17$\beta$-estradiol is present. This could be explained by the aptamer changing its 3D configuration when the target is captured, but this trend could not be reproduced.

It was then investigated whether the presence of Tween20 in the washing buffer solution, might influence the binding of aptamer and 17$\beta$-estradiol. The surfactant may act too strongly in removing unbound molecules, in that the aptamer-target complex is not a particularly strong bond (dissociation constant $K_d = 50$ nM). This bond might be disrupted by the addition of Tween20 in the binding buffer. It was not the case for Experiment B, where the addition of Tween20 enhanced the specificity of the sensor by eliminating weakly bound molecules. But in that case the bond between the aptamer and the 100 % complementary strand of DNA is very strong due to the amount of hydrogen bonds formed between the base pairs.

In the investigation of the effect of Tween20 on the aptamer-17$\beta$-estradiol complex the same protocol was used, except for the exclusion of the 3x3 min wash step in binding buffer with 0.1 % Tween20 added. By mistake the 17$\beta$-estradiol binding solution was made to 500 µM instead of 500 nM. This saturated the solution since 17$\beta$-estradiol has a solubility in water around 1 µM. This effectively increased the intended concentration in contact with the aptamer/MCH coated nanopillar surface. Despite this mishap the experiment provided information regarding the effect of Tween20 in the washing buffer. The average spectra is shown in Figure 4.36, where no difference is obtained for samples with or without 17$\beta$-estradiol. Running the data through the peak-fitting model for the 808 $cm^{-1}$ peak yielded no other conclusions (data not shown).

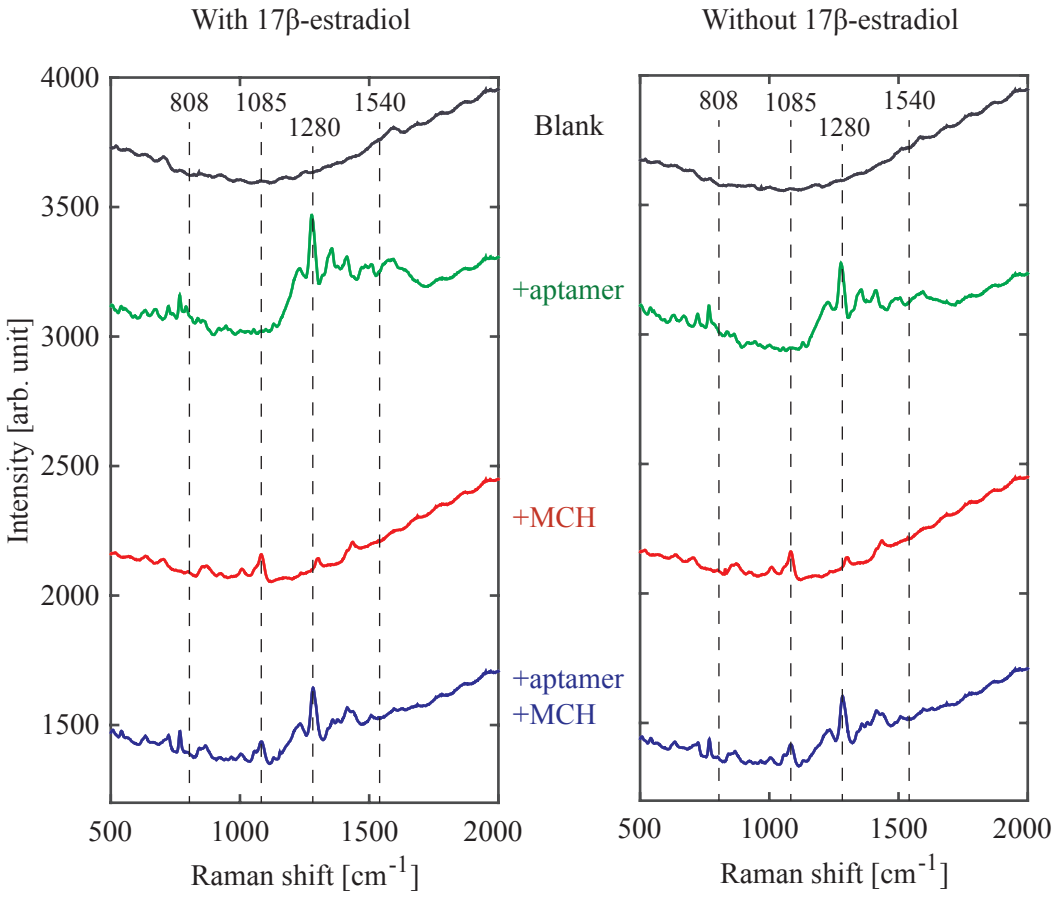


Figure 4.36: Average spectra of 17$\beta$-estradiol detection without Tween20 in the washing buffer (batch: KF7-2). A very high concentration (500 µM) of 17$\beta$-estradiol was accidentally used. The experiments however still revealed no change in the overall spectra.

Based on these experiments it was concluded that selective and specific label-free detection of 17$\beta$-estradiol using aptamer was not possible based solemnly on the SERS spectra. This was despite a very high concentration of 17$\beta$-estradiol (500 µM) was used. The reason for unsuccessful detection could be either of one of following reasons:

1. The aptamer is not capturing the target.
2. The assay worked as intended, but the Raman peaks arising from capture of 17$\beta$-estradiol are too weak to be detected.

Re item 1 - this would explain why no 17$\beta$-estradiol peaks are seen. Inability of the aptamer to capture the target could be due to the binding buffer composition or the 3D conformation of the aptamer. The buffer composition must both support the 3D folding of the aptamer while optimising the chances of target binding. The buffer was therefore chosen to be the one reported from the SELEX process where the aptamer was selected. The 3D conformation was tried to be obtimised with the use of a high salt solution (2 M UREA and 7.5 mM EDTA in $H_2O$), but it was not possible to measure if the right 3D structure had been obtained. Re item 2 - this is more likely since the Raman spectrum obtained for pure 17$\beta$-estradiol did not show any particularly strong peaks. Only a minor peak at 808 $cm^{-1}$ peak was seen, but this could not be retrieved in the complex spectra of the full assay. The amount of target bound to the aptamer might also be a limiting factor, in that only one molecule pr. aptamer is caught (in theory), which is a much less amount compared to the amount immobilised during experiment with only 17$\beta$-estradiol where a more uniform coverage is expected.

### Labelled 17$\beta$-estradiol detection

Since a label-free sensor for detection of 17$\beta$-estradiol could not be obtained it was pursued to detect Estradiol Glow instead. To investigate the spectrum of pure Estradiol Glow on gold nanopillars one droplet of 1 mM solution in ethanol was applied and dried on the substrate. This substrate was not cleaned beforehand, but the ethanol solution was seen to spread nice and evenly on the surface. Once dried the Raman spectra were obtained. The average spectra is shown in Figure 4.37.

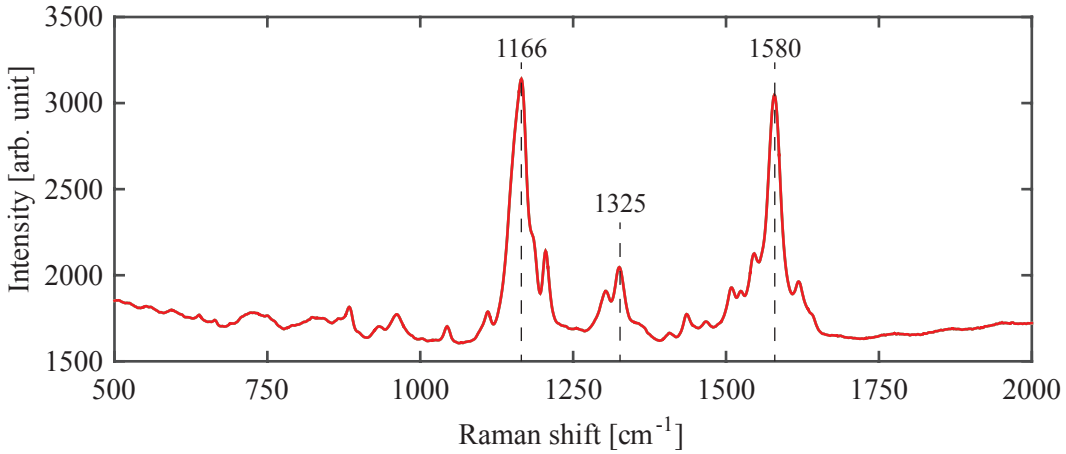


Figure 4.37: Average spectrum of Estradiol Glow (1 mM in ethanol, batch KF7-1). The spectrum reveals strong peaks at 1166 $cm^{-1}$, 1325 $cm^{-1}$ and 1580 $cm^{-1}$, which can be used for detection when employing the aptamer assay.

From this spectrum it can be seen that several very strong peaks are present as for the silver substrate (Experiment A). Especially peaks at 1166 $cm^{-1}$, 1325 $cm^{-1}$ and 1580 $cm^{-1}$ are prominent and were anticipated to be detectable when using the aptamer assay. The same protocol as for label-free detection of 17$\beta$-estradiol was employed for detection of Estradiol Glow aptamer capture. This experiment also investigated the role of Tween20 in the washing buffer. Average spectra are shown in Figure 4.38.

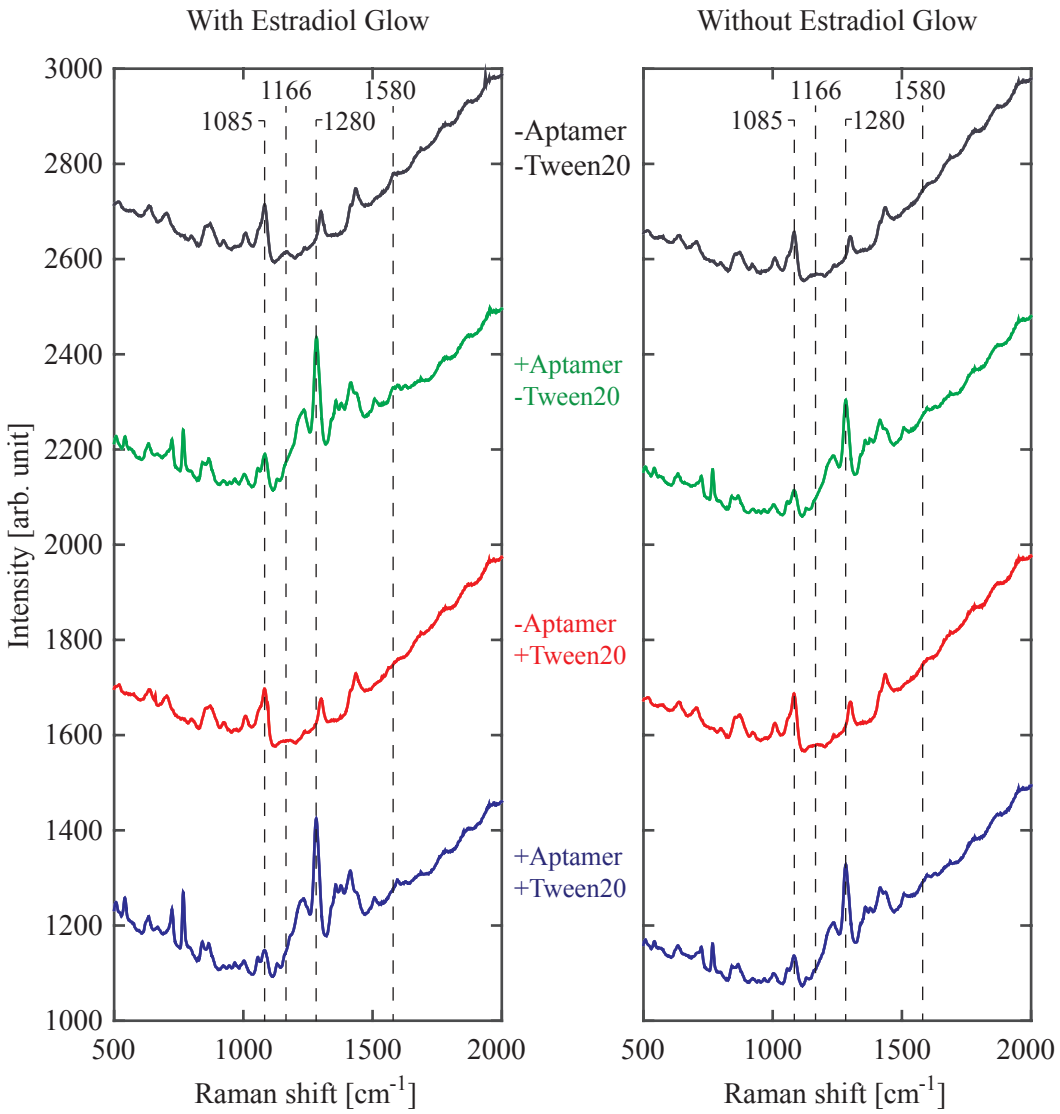


Figure 4.38: Average spectra of the Estradiol Glow experiment (batch: KF7-2). As for the experiment with pure 17$\beta$-estradiol no change in the spectra is seen. This could be due to the aptamer not being capable of binding Estradiol Glow due to the fluorescent label blocking the binding site.

As can be seen there are no additional peaks appearing for any assay combination when the substrate is exposed to Estradiol Glow. The addition of Tween20 seems to have no influence on the Raman spectra as well. When applying the peak fitting model on the 1280 $cm^{-1}$ aptamer peak it shows a slight increase in intensity profile as seen for regular 17$\beta$-estradiol (see Figure 4.39), but this could just be a statistical artifact. A more thorough statistical analysis could be done in order to determine the shape parameters of the distribution, but this might require more than 300 measurements to be statistically valid (cf. Etchegoin et al. [55]).

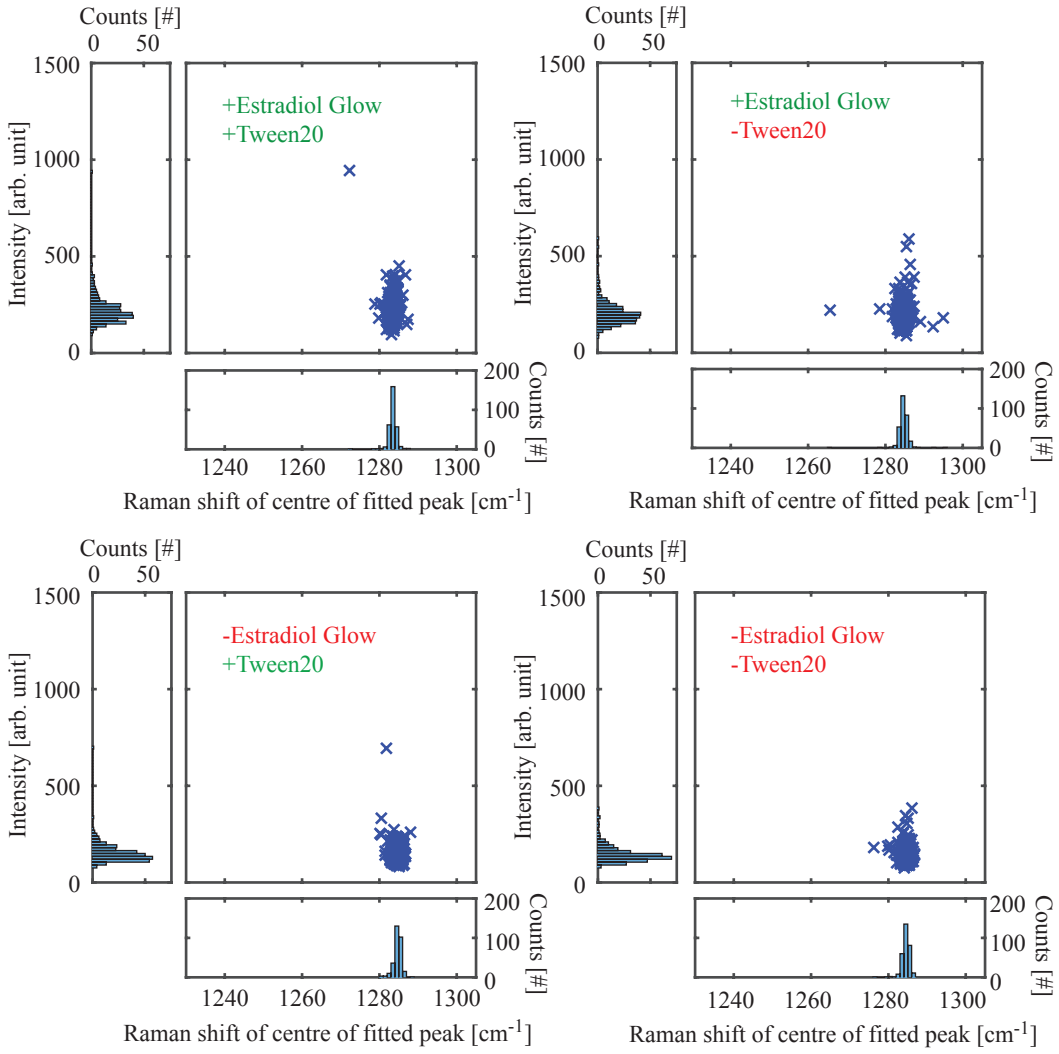


Figure 4.39: Scatterplots of the Estradiol Glow Experiment (batch: KF7-2). A slight elongation of the intensity distribution is again seen. However further statistical analysis have to be done to make any conclusion. The $n = 300$ measurements might be too few for proper statistical analysis.

Based on these experiments it was determined that Estradiol Glow could not be selectively detected using the aptamer assay. This could be due to the same reasons as for failed label-free detection of 17$\beta$-estradiol. Especially the uncertainty that the aptamer is capable of binding Estradiol Glow should be considered, since the fluorescent label might obstruct the binding site.

### 4.6.3 Investigation of aptamer-target binding

Two additional analysis methods were also investigated; QCM-D and matrix-assisted laser desorption/ionization time-of-flight (MALDI-TOF). QCM-D was employed in the early stage of protocol development to see if any information could be extracted from the system. QCM-D experiments were performed on commercial gold coated crystals in order to investigate the effect of the initial (standard) protocol on the surface. The different functionalisation steps were performed multiple times, but no clear results were obtained. This could relate to that QCM-D is a mass sensitive technique, which has detection limit in the range of the mass of 17$\beta$-estradiol [10]. It was also concluded that if a set of functionalisation parameters was obtained for QCM-D experiments it might be vastly different when investigating functionalisation of gold coated nanopillars.

MALDI-TOF experiments were performed on standard stainless steal templates, where a suitable matrix (3-Hydroxypicolinic acid) was mixed with aptamer-17$\beta$-estradiol mixture in binding buffer and dried. By laser irradiation the matrix absorbs energy and ionizes the matrix-aptamer-target complex, which is accelerated in an electric field towards a detector. By measuring the time-of-flight the molecular weight can be determined. It was sought to investigate if aptamer-target mixtures could be distinguished from aptamer-only samples. Despite several attempts no clear signal could be obtained for any samples, which might relate to that 75-mer DNA strands are challenging to characterise by MALDI-TOF [80]. It was intended to validate the functionalisation protocol by MALDI-TOF directly on the nanopillar surface.

Both techniques are definitely viable in terms of being capable of analysing aptamer-target complexes, however each of them requires extensive optimisation before any useful conclusions can be drawn. For these reasons both of the techniques were abandoned before too much time was spent.

### 4.6.4 Conclusion to Experiment D

Development of a SERS aptasensor for 17$\beta$-estradiol detection was attempted using the gold SERS substrate. By employing the functionalisation protocol developed in Experiment C it was expected that peaks from either pure 17$\beta$-estradiol or Estradiol Glow would appear in the aptamer/MCH spectra. However no successful detection was obtained for either molecule. It was seen

that spectra originating from pure 17$\beta$-estradiol on gold nanopillar (without functionalisation) revealed that it does not exhibit any particularly strong Raman peaks. This is troublesome if label-free detection is sought, as it relies on changes to the spectrum. The unsuccessful detection of Estradiol Glow could be due to the fluorescent label hindering proper aptamer binding. Applying the peak-fitting model did not alter the result.

# 5 Conclusion

In this project it was attempted to develop a sensitive surface enhanced Raman spectroscopy (SERS) aptasensor for detection of medical residues. Specifically 17$\beta$-estradiol was investigated. In particular a suitable chemical functionalisation protocol for the sensor surface was needed for proper sensor function.

SERS substrates based on silver or gold coated silicon nanopillars were successfully fabricated repeatedly. The substrates were very efficient for enhancement of Raman signals. Therefore the chemical functionalisation protocol was analysed using only Raman signals.

First silver substrates were used as a SERS substrate, since the enhancement was seen to be greater than for gold substrates. It was however found that silver at the nanoscale unintentionally reacted with hydrocloric acid which was needed for disulphide reduction in the DNA aptamer strand. Particles, assumed to be silvercloride, were seen to aggregate on the nanopillar surface. Despite this, a multivariate analysis of the spectra obtained from Estradiol Glow was developed. Non-negative Matrix Factorization (NMF) was employed on the data sets and it showed to increase the detection limit by at least one order of magnitude. NMF proved to be very well suited for analysing large data sets (1000+ spectra) by identifying regions of interest.

Secondly, gold substrates were investigated. Proper immobilisation of aptamer was investigated by the use of fluorescently labelled complementary DNA (cDNA). Experiments showed that cDNA could selectively be captured by the aptamer compared to non-complementary DNA (ncDNA). This proved that aptamer was properly immobilised on the gold coated nanopillars and capable of forming bonds to a target in solution. The role of the non-ionic detergent Tween20 was also investigated, and it was found to greatly reduce unspecific binding.

Further investigation of the chosen chemical functionalisation strategy was then employed. It was quickly discovered that manual inspection of the data sets would be extremely labour intensive. NMF could not be utilised in this

stage of development, since a uniform coverage of aptamer and 6-mercapto-1-hexanol on the nanopillars was sought. Therefore a peak-fitting model was developed. By analysing a given spectral window in which a peak is expected, it was possible to fit a pseudo-Voigt function to the data sets. This allowed for a more thorough analysis than previously conducted, which meant that optimal chemical functionalisation parameters could be obtained. This analysis was generic for all SERS aptasensors.

Detection of both label-free and labelled 17$\beta$-estradiol (Estradiol Glow) was lastly attempted. Unfortunately no additional peaks were seen for either of them. Despite several attempts 17$\beta$-estradiol could not be selectively detected by the SERS aptasensor. This is probably due to the low Raman signature of 17$\beta$-estradiol, which was observed for pure samples. Also the aptamer have not been selected towards Estradiol Glow, which meant that binding was not guaranteed.

# 6 Outlook

Aptasensors have the potential to be an integral part of the biosensor industry. The relatively easy synthesis of DNA aptamers drive the motivation of aptasensor development. Since aptamers can be synthesised towards practically any biological target, they have a great potential to substitute or at least supplement classical antibody-based immunosensors.

Utilizing the strengths of SERS in combination with aptamers yields a powerful and versatile tool for small molecule detection. The chemical 'fingerprinting' capability of SERS is very well suited for small molecule detection as larger molecules will contain a multitude of vibrational modes, which can be troublesome to analyse. Whereas small molecules often only have a few distinct vibrational modes that is more easily recognised in a complex sample. Especially if considering a label-free aptasensor, SERS is an excellent candidate as chemical information can be obtained.

## 6.1 Medical residues

Medical residues are becoming priority substances to monitor in both environmental, industrial and domestic waters [2]. Most of these are small molecules, which could be well suited for a SERS aptasensor. There are continuously reports of new DNA aptamer sequences towards medical residues such as diclofenac [81], ampicillin [82] and ibuprofen [83]. The best suited candidates for a SERS aptasensor, would however be those which exhibit an intrinsically strong Raman activity. This property is not easily recognised, but a comprehensive guideline is described by Nakamoto [84]. In general, ring-structures and double/triple bonds without too much steric hindrance are suitable candidates. This is exemplified by the molecular structure of BPE (insert of Figure 4.2) and Estradiol Glow (Figure 4.3), which both yielded very strong Raman spectra. The structure of BPE is almost entirely present in the structure of the fluorescent label of Estradiol Glow. This means that medical residues contain-

ing structural similarities to BPE and the fluorescent label of Estradiol Glow are strong candidates for label-free SERS aptasensors.

## 6.2 17$\beta$-estradiol

Despite that 17$\beta$-estradiol could not successfully be detected by the SERS aptasensor described in this thesis, further development is definitely possible. The hormone is heavily studied by research groups worldwide [38, 85–87], which demonstrates the need for development of a sensitive sensor. Especially the recent work of Vanschoenbeek et al. [87] is of interest for a SERS aptasensor. They report on a variety of aptamers which target different regions of 17$\beta$-estradiol. This is particularly interesting in combination with Estradiol Glow, as the aptamer used throughout the project was never guaranteed to bind Estradiol Glow. However by having a library of aptamers targetting different regions, this obstacle could be overcome. If this is achieved Estradiol Glow could be implemented in an competitve assay towards 17$\beta$-estradiol.

Experimental work in this thesis showed promising detection limits of pure 17$\beta$-estradiol. This could be pursued and optimised to be used in a downstream detection detection step of purified samples. Standardised affinity column purifications are commonly used to determine the level of 17$\beta$-estradiol in water samples. Here SERS is a viable alternative to the mass spectrometer subsequently used for analysis. SERS provides a quick and sensitive response on a minute (microliter) sample.

## 6.3 Statistical SERS tools

As demonstrated in this thesis SERS is a statistical analysis method. In order to analyse large data sets statistical tools are needed. Both the NMF and peak-fitting algorithm presented in this thesis proved to be powerful tools. If a SERS aptasensor is to be developed, then these or similar tools must be implemented in the data analysis.

## 6.4 Sensor integration

Integration of a SERS aptasensor on a microfluidic platform is definitly viable. Especially the proposed DVD platform in the MUSE project would be a suitable platform. The SERS substrates are small in size, which enables easy integration in DVD-shaped polymer discs. Since SERS is an optical technique it would only require that the nanopillar surface is accessible for a laser beam

to be functional. However technical challenges relating to polymer noise, liquid interference and substrate wettability should be addressed.

# Bibliography

[1] Maria Thunø, Betina Macho, and Jesper Eugen-Olsen. suPAR: the molecular crystal ball. *Disease markers*, 27(3):157–72, January 2009.

[2] European Commission. Environment and water: proposal to reduce water pollution risks, January 2012. [Press release. Online; accessed 2015-08-03. `http://europa.eu/rapid/press-release_IP-12-88_en.htm`].

[3] M.I. Vasquez, A. Lambrianides, M. Schneider, K. Kümmerer, and D. Fatta-Kassinos. Environmental side effects of pharmaceutical cocktails: What we know and what we should know. *Journal of Hazardous Materials*, 279:169–189, August 2014.

[4] Michael Stenbæk Schmidt, Natalie Kostesha, Filippo Bosco, Jesper Kenneth Olsen, Carsten Johnsen, Kent a. Nielsen, Jan Oskar Jeppesen, Tommy Sonne Alstrøm, Jan Larsen, Thomas Thundat, Mogens Havsteen Jakobsen, and Anja Boisen. Xsense: a miniaturised multi-sensor platform for explosives detection. In Thomas George, M. Saif Islam, and Achyut K. Dutta, editors, *Proceedings of SPIE*, volume 8031, pages 803123–803123–7, May 2011.

[5] Robert Burger, Daniel Kirby, Macdara Glynn, Charles Nwankire, Mary O'Sullivan, Jonathan Siegrist, David Kinahan, Gerson Aguirre, Gregor Kijanka, Robert A Gorkin III, and Jens Ducrée. Centrifugal microfluidics for cell analysis. *Current Opinion in Chemical Biology*, 16(3-4):409–414, August 2012.

[6] Michael Stenbaek Schmidt, Jörg Hübner, and Anja Boisen. Large Area Fabrication of Leaning Silicon Nanopillars for Surface Enhanced Raman Spectroscopy. *Advanced Materials*, 24(10):OP11–OP18, March 2012.

[7] Miriam A Kelly, Antoinette M Reid, Kathryn M Quinn-Hosey, Andrew M Fogarty, James J Roche, and Concepta A Brougham. Investigation of the estrogenic risk to feral male brown trout (Salmo trutta) in the Shannon International River Basin District of Ireland. *Ecotoxicology and Environmental Safety*, 73(7):1658–1665, October 2010.

[8] National Institute of Health. A timeline of pregnancy testing. [Online; accessed 2015-08-03. `http://history.nih.gov/exhibits/thinblueline/timeline.html`].

[9] Adam B. Steel, Tonya M. Herne, and Michael J. Tarlov. Electrochemical Quantitation of DNA Immobilized on Gold. *Analytical Chemistry*, 70(22):4670–4677, November 1998.

[10] Yeon Seok Kim, Ho Sup Jung, Toshihiko Matsuura, Hea Yeon Lee, Tomoji Kawai, and Man Bock Gu. Electrochemical detection of 17$\beta$-estradiol using DNA aptamer immobilized gold electrode chip. *Biosensors and Bioelectronics*, 22(11):2525–2531, May 2007.

[11] Bhavya Sharma, M. Fernanda Cardinal, Samuel L. Kleinman, Nathan G. Greeneltch, Renee R. Frontiera, Martin G. Blaber, George C. Schatz, and Richard P. Van Duyne. High-performance SERS substrates: Advances and challenges. *MRS Bulletin*, 38(08):615–624, August 2013.

[12] Eleonora Petryayeva and Ulrich J. Krull. Localized surface plasmon resonance: Nanostructures, bioassays and biosensing—A review. *Analytica Chimica Acta*, 706(1):8–24, November 2011.

[13] Jürgen Fritz. Cantilever biosensors. *The Analyst*, 133(7):855, July 2008.

[14] Yasuhide Ohno, Kenzo Maehashi, and Kazuhiko Matsumoto. Label-Free Biosensors Based on Aptamer-Modified Graphene Field-Effect Transistors. *Journal of the American Chemical Society*, 132(51):18012–18013, December 2010.

[15] Joseph Wang. Electrochemical glucose biosensors. In *Electrochemical Sensors, Biosensors and their Biomedical Applications*, pages 57–I. Elsevier, 2008.

[16] Tonya M. Herne and Michael J. Tarlov. Characterization of DNA Probes Immobilized on Gold Surfaces. *Journal of the American Chemical Society*, 119(38):8916–8920, September 1997.

[17] Hannu Häkkinen. The gold–sulfur interface at the nanoscale. *Nature Chemistry*, 4(6):443–455, May 2012.

[18] David J. Griffiths. *Introduction to Electrodynamics*. Pearson, 2008. Third edition. ISBN: 0-13-919960-8.

[19] Henrik Bruus. *Theoretical Microfluidics*. Oxford master series in condensed matter physics. Oxford, 2010. ISBN: 978-0-19-923508-7.

[20] RSCB Protein Data Bank. Antibodies. [Online; accessed 2015-08-05. `http://www.rcsb.org/pdb/101/motm.do?momID=21`].

[21] RSCB Protein Data Bank. Overview of antibody production and purification. [Online; accessed 2015-08-05. `https://www.lifetechnologies.com/dk/en/home/life-science/protein-biology/protein-biology-learning-center/protein-biology-resource-library/pierce-protein-methods/overview-antibody-production-purification.html`].

[22] Debra L. Robertson and Gerald F. Joyce. Selection in vitro of an RNA enzyme that specifically cleaves single-stranded DNA. *Nature*, 344(6265):467–468, March 1990.

[23] Andrew D. Ellington and Jack W. Szostak. In vitro selection of RNA molecules that bind specific ligands. *Nature*, 346(6287):818–822, August 1990.

[24] C. Tuerk and L. Gold. Systematic evolution of ligands by exponential enrichment: RNA ligands to bacteriophage T4 DNA polymerase. *Science*, 249(4968):505–510, August 1990.

[25] Omar A. Alsager, Shalen Kumar, Bicheng Zhu, Jadranka Travas-Sejdic, Kenneth P. McNatty, and Justin M. Hodgkiss. Ultrasensitive Colorimetric Detection of 17$\beta$-Estradiol: The Effect of Shortening DNA Aptamer Sequences. *Analytical Chemistry*, 87(8):4201–4209, April 2015.

[26] Florian Jarosch. In vitro selection using a dual RNA library that allows primerless selection. *Nucleic Acids Research*, 34(12):e86–e86, July 2006.

[27] Louis C. Bock, Linda C. Griffin, John A. Latham, Eric H. Vermaas, and John J. Toole. Selection of single-stranded DNA molecules that bind and inhibit human thrombin. *Nature*, 355(6360):564–566, February 1992.

[28] K. Padmanabhan and A. Tulinsky. An Ambiguous Structure of a DNA 15-mer Thrombin Complex. *Acta Crystallographica Section D Biological Crystallography*, 52(2):272–282, March 1996.

[29] Irene Russo Krauss, Antonello Merlino, Antonio Randazzo, Ettore Novellino, Lelio Mazzarella, and Filomena Sica. High-resolution structures of two complexes between thrombin and thrombin-binding aptamer shed

light on the role of cations in the aptamer inhibitory activity. *Nucleic Acids Research*, 40(16):8119–8128, September 2012.

[30] Diane M. Tasset, Mark F. Kubik, and Walter Steiner. Oligonucleotide inhibitors of human thrombin that bind distinct epitopes. *Journal of Molecular Biology*, 272(5):688–698, October 1997.

[31] Omar A. Alsager, Shalen Kumar, Geoff R. Willmott, Kenneth P. McNatty, and Justin M. Hodgkiss. Small molecule detection in solution via the size contraction response of aptamer functionalized nanoparticles. *Biosensors and Bioelectronics*, 57:262–268, July 2014.

[32] Minjoung Jo, Ji-Young Ahn, Joohyung Lee, Seram Lee, Sun Woo Hong, Jae-Wook Yoo, Jeehye Kang, Pooja Dua, Dong-Ki Lee, Seunghun Hong, and Soyoun Kim. Development of Single-Stranded DNA Aptamers for Specific Bisphenol A Detection. *Oligonucleotides*, 21(2):85–91, April 2011.

[33] Xiaoli Zhu, Jinghua Yang, Min Liu, Yao Wu, Zhongming Shen, and Genxi Li. Sensitive detection of human breast cancer cells based on aptamer–cell–aptamer sandwich architecture. *Analytica Chimica Acta*, 764:59–63, February 2013.

[34] Ciara K. O'Sullivan. Aptasensors – the future of biosensing? *Analytical and Bioanalytical Chemistry*, 372(1):44–48, January 2002.

[35] Rasaq A. Olowu, Omotayo Arotiba, Stephen N. Mailu, Tesfaye T. Waryo, Priscilla Baker, and Emmanuel Iwuoha. Electrochemical Aptasensor for Endocrine Disrupting 17$\beta$-Estradiol Based on a Poly(3,4-ethylenedioxylthiopene)-Gold Nanocomposite Platform. *Sensors*, 10(11):9872–9890, November 2010.

[36] Zhenyu Lin, Lifen Chen, Guiyun Zhang, Qida Liu, Bin Qiu, Zongwei Cai, and Guonan Chen. Label-free aptamer-based electrochemical impedance biosensor for 17$\beta$-estradiol. *The Analyst*, 137(4):819–822, 2012.

[37] Ke-Jing Huang, Yu-Jie Liu, Gang-Wei Shi, Xue-Rui Yang, and Yan-Ming Liu. Label-free aptamer sensor for 17$\beta$-estradiol based on vanadium disulfide nanoflowers and Au nanoparticles. *Sensors and Actuators B: Chemical*, 201:579–585, October 2014.

[38] Bicheng Zhu, Omar A. Alsager, Shalen Kumar, Justin M. Hodgkiss, and Jadranka Travas-Sejdic. Label-free electrochemical aptasensor for femtomolar detection of 17$\beta$-estradiol. *Biosensors and Bioelectronics*, 70:398–403, August 2015.

[39] Nimet Yildirim, Feng Long, Ce Gao, Miao He, Han-chang Shi, and April Z. Gu. Aptamer-Based Optical Biosensor For Rapid and Sensitive

Detection of 17$\beta$-Estradiol In Water Samples. *Environmental Science & Technology*, 46(6):3288–3294, March 2012.

[40] P. G. Etchegoin and E. C. Le Ru. A perspective on single molecule SERS: current status and future challenges. *Physical Chemistry Chemical Physics*, 10(40):6079, 2008.

[41] M. Procházka. Raman and surface-enhanced Raman scattering (SERS) biosensing. *SPIE Optics + Optoelectronics*, 8774:877409, 2013.

[42] Lars Kastrup and Stefan W. Hell. Absolute Optical Cross Section of Individual Fluorescent Molecules. *Angewandte Chemie International Edition*, 43(48):6646–6649, December 2004.

[43] M. Fleischmann, P. J. Hendra, and A. J. McQuillan. Raman spectra of pyridine adsorbed at a silver electrode. *Chemical Physics Letters*, 26(2):163–166, May 1974.

[44] Katrin Kneipp, Yang Wang, Harald Kneipp, Lev T. Perelman, Irving Itzkan, Ramachandra R. Dasari, and Michael S. Feld. Single Molecule Detection Using Surface-Enhanced Raman Scattering (SERS). *Physical Review Letters*, 78(9):1667–1670, March 1997.

[45] S. Nie and Steven R. Emory. Probing Single Molecules and Single Nanoparticles by Surface-Enhanced Raman Scattering. *Science*, 275(5303):1102–1106, February 1997.

[46] E J Liang and W. Kiefer. Chemical Effect of SERS with Near-Infrared Excitation. *Journal of Raman Spectroscopy*, 27(12):879–885, December 1996.

[47] B. Wehling, W. Hill, and D. Klockow. Selective chemical enhancement of SERS by iodide. *Journal of Molecular Structure*, 349:117–120, April 1995.

[48] Jerry Cabalo, Jason A. Guicheteau, and Steven Christesen. Toward Understanding the Influence of Intermolecular Interactions and Molecular Orientation on the Chemical Enhancement of SERS. *The Journal of Physical Chemistry A*, 117(37):9028–9038, September 2013.

[49] Justin E. Moore, Seth M. Morton, and Lasse Jensen. Importance of Correctly Describing Charge-Transfer Excitations for Understanding the Chemical Effect in SERS. *The Journal of Physical Chemistry Letters*, 3(17):2470–2475, September 2012.

[50] Eric C. Le Ru, Matthias Meyer, and Pablo G. Etchegoin. Proof of Single-Molecule Sensitivity in Surface Enhanced Raman Scattering (SERS) by

Means of a Two-Analyte Technique. *The Journal of Physical Chemistry B*, 110(4):1944–1948, February 2006.

[51] a. Gopalakrishnan, M. Malerba, S. Tuccio, S. Panaro, E. Miele, M. Chirumamilla, S. Santoriello, C. Dorigoni, A. Giugni, R. Proietti Zaccaria, C. Liberale, F. De Angelis, L. Razzari, R. Krahne, A. Toma, G. Das, and E. Di Fabrizio. Nanoplasmonic structures for biophotonic applications: SERS overview. *Annalen der Physik*, 524(11):620–636, November 2012.

[52] Gobind Das, Federico Mecarini, Francesco Gentile, Francesco De Angelis, Mohan Kumar HG, Patrizio Candeloro, Carlo Liberale, Giovanni Cuda, and Enzo Di Fabrizio. Nano-patterned SERS substrate: Application for protein analysis vs. temperature. *Biosensors and Bioelectronics*, 24(6):1693–1699, February 2009.

[53] Jordan F. Betz, Wei W. Yu, Yi Cheng, Ian M. White, and Gary W. Rubloff. Simple SERS substrates: powerful, portable, and full of potential. *Phys. Chem. Chem. Phys.*, 16(6):2224–2239, February 2014.

[54] Wei W. Yu and Ian M. White. Optofluidic SERS on Paper: A Lateral Flow Concentration Assay Using Inkjet Fabricated SERS-Active Substrates. In *Conference on Lasers and Electro-Optics 2012*, Washington, D.C., 2012. OSA.

[55] Pablo G. Etchegoin, Matthias Meyer, and Eric C. Le Ru. Statistics of single molecule SERS signals: is there a Poisson distribution of intensities? *Physical Chemistry Chemical Physics*, 9(23):3006, 2007.

[56] Celly M. S. Izumi, Matthew G. Moffitt, and Alexandre G. Brolo. Statistics on Surface-Enhanced Resonance Raman Scattering from Single Nanoshells. *The Journal of Physical Chemistry C*, 115(39):19104–19109, October 2011.

[57] Jaeyoung Yang, Mirko Palla, Filippo Giacomo Bosco, Tomas Rindzevicius, Tommy Sonne Alstrøm, Michael Stenbæk Schmidt, Anja Boisen, Jingyue Ju, and Qiao Lin. Surface-Enhanced Raman Spectroscopy Based Quantitative Bioassay on Aptamer-Functionalized Nanopillars Using Large-Area Raman Mapping. *ACS Nano*, 7(6):5350–5359, June 2013.

[58] Tsengyou Syau. Reactive Ion Etching of Silicon Trenches Using SF6-O2 Gas Mixtures. *Journal of The Electrochemical Society*, 138(10):3076, 1991.

[59] R. Pinto, K. V. Ramanathan, and R. S. Babu. Reactive Ion Etching in SF6 Gas Mixtures. *Journal of The Electrochemical Society*, 134(1):165, 1987.

[60] Michael D. Deal James D. Plummer and Peter B. Griffin. *Silicon VLSI Technology*. Prentice Hall Electronics and VLSI Series. Prentice Hall, 2000. ISBN: 0-13-085037-3.

[61] Kaiyu Wu, Tomas Rindzevicius, Michael Stenbæk Schmidt, Klaus Bo Mogensen, Sanshui Xiao, and Anja Boisen. Plasmon resonances of Ag capped Si nanopillars fabricated using mask-less lithography. *Optics Express*, 23(10):12965, May 2015.

[62] Anna Line Brøgger, Michael Stenbæk Schmidt, and Anja Boisen. Removal of Residues from Reactive Ion Etched Silicon Surfaces Characterized with XPS and SERS. In *Poster at 40th International Conference on Micro and Nano Engineering*, 2014.

[63] A. H. Pakiari and Z. Jamshidi. Nature and Strength of M-S Bonds (M = Au, Ag, and Cu) in Binary Alloy Gold Clusters. *The Journal of Physical Chemistry A*, 114(34):9212–9221, September 2010.

[64] Yurui Xue, Xun Li, Hongbin Li, and Wenke Zhang. Quantifying thiol–gold interactions towards the efficient strength control. *Nature Communications*, 5:4348, July 2014.

[65] Sunho Park, Katherine A. Brown, and Kimberly Hamad-Schifferli. Changes in Oligonucleotide Conformation on Nanoparticle Surfaces by Modification with Mercaptohexanol. *Nano Letters*, 4(10):1925–1929, October 2004.

[66] Shintaro Pang, Theodore P. Labuza, and Lili He. Development of a single aptamer-based surface enhanced Raman scattering method for rapid detection of multiple pesticides. *The Analyst*, 139(8):1895–1901, March 2014.

[67] Xiaoyu Zhang, Nilam C. Shah, and Richard P. Van Duyne. Sensitive and selective chem/bio sensing based on surface-enhanced Raman spectroscopy (SERS). *Vibrational Spectroscopy*, 42(1):2–8, October 2006.

[68] Eunsu Chung, Jinhyeok Jeon, Jimin Yu, Chankil Lee, and Jaebum Choo. Surface-enhanced Raman scattering aptasensor for ultrasensitive trace analysis of bisphenol A. *Biosensors and Bioelectronics*, 64:560–565, February 2015.

[69] Eva Baldrich, Alexandre Restrepo, and Ciara K. O'Sullivan. Aptasensor Development: Elucidation of Critical Parameters for Optimal Aptamer Performance. *Analytical Chemistry*, 76(23):7053–7063, December 2004.

[70] Nishi Bhatt, Po-Jung Jimmy Huang, Neeshma Dave, and Juewen Liu. Dissociation and Degradation of Thiol-Modified DNA on Gold Nanoparticles in Aqueous and Organic Solvents. *Langmuir*, 27(10):6132–6137, May 2011.

[71] Claire André, Alain Xicluna, and Yves-Claude Guillaume. Aptamer-oligonucleotide binding studied by capillary electrophoresis: Cation effect and separation efficiency. *ELECTROPHORESIS*, 26(17):3247–3255, September 2005.

[72] Steven Yampolsky, Dmitry A. Fishman, Shirshendu Dey, Eero Hulkko, Mayukh Banik, Eric O. Potma, and Vartkess A. Apkarian. Seeing a single molecule vibrate through time-resolved coherent anti-Stokes Raman scattering. *Nature Photonics*, 8(8):650–656, July 2014.

[73] Evan J. Blackie, Eric C. Le Ru, and Pablo G. Etchegoin. Single-Molecule Surface-Enhanced Raman Spectroscopy of Nonresonant Molecules. *Journal of the American Chemical Society*, 131(40):14466–14472, October 2009.

[74] Kaiyu Wu, Michael Stenbæk Schmidt, Tomas Rindzevicius, and Anja Boisen. Optimizing Signal-to-Noise Ratio of SERS Ag Capped Si Nanopillars. In *Poster at Third International Conference on Frontiers of Plasmonics*, 2014.

[75] Liang Li and Ying-Jie Zhu. High chemical reactivity of silver nanoparticles toward hydrochloric acid. *Journal of Colloid and Interface Science*, 303(2):415–418, November 2006.

[76] G. K. Wertheim, M. A. Butler, K. W. West, and D. N. E. Buchanan. Determination of the Gaussian and Lorentzian content of experimental line shapes. *Review of Scientific Instruments*, 45(11):1369, 1974.

[77] Nicholas Metropolis, Arianna W. Rosenbluth, Marshall N. Rosenbluth, Augusta H. Teller, and Edward Teller. Equation of State Calculations by Fast Computing Machines. *The Journal of Chemical Physics*, 21(6):1087, 1953.

[78] W. K. Hastings. Monte Carlo sampling methods using Markov chains and their applications. *Biometrika*, 57(1):97–109, 1970.

[79] R. Georgiadis, K. P. Peterlinz, and A. W. Peterson. Quantitative Measurements and Modeling of Kinetics in Nucleic Acid Monolayer Films Using SPR Spectroscopy. *Journal of the American Chemical Society*, 122(13):3166–3173, April 2000.

[80] Zongwei Cai, Shuying Liu, and Daiki Asakawa. *Applications of MALDI-TOF Spectroscopy*, volume 331 of *Topics in Current Chemistry*. Springer Berlin Heidelberg, Berlin, Heidelberg, 2013.

[81] Choon Bok Joeng, Javed H Niazi, Su Jin Lee, and Man Bock Gu. ssDNA aptamers that recognize diclofenac and 2-anilinophenylacetic acid. *Bioorganic & medicinal chemistry*, 17(15):5380–7, August 2009.

[82] Kyung-Mi Song, Euiyoung Jeong, Weejeong Jeon, Minseon Cho, and Changill Ban. Aptasensor for ampicillin using gold nanoparticle based dual fluorescence–colorimetric methods. *Analytical and Bioanalytical Chemistry*, 402(6):2153–2161, February 2012.

[83] Yeon Seok Kim, Chang Jun Hyun, In Ae Kim, and Man Bock Gu. Isolation and characterization of enantioselective DNA aptamers for ibuprofen. *Bioorganic & Medicinal Chemistry*, 18(10):3467–3473, May 2010.

[84] Kazuo Nakamoto. *Infrared and Raman Spectra of Inorganic and Coordination Compounds*. John Wiley & Sons, Inc., Hoboken, NJ, USA, December 2008.

[85] Jing-Jing Zhang, Jun-Tao Cao, Gui-Fang Shi, Ke-Jing Huang, Yan-Ming Liu, and Yong-Hong Chen. Label-free and sensitive electrochemiluminescence aptasensor for the determination of 17$\beta$-estradiol based on a competitive assay with cDNA amplification. *Analytical Methods*, 6(17):6796, July 2014.

[86] Ke-Jing Huang, Yu-Jie Liu, and Ji-Zong Zhang. Aptamer-based electrochemical assay of 17$\beta$-estradiol using a glassy carbon electrode modified with copper sulfide nanosheets and gold nanoparticles, and applying enzyme-based signal amplification. *Microchimica Acta*, 182(1-2):409–417, September 2014.

[87] Katrijn Vanschoenbeek, Jeroen Vanbrabant, Baharak Hosseinkhani, Veronique Vermeeren, and Luc Michiels. Aptamers targeting different functional groups of 17$\beta$-estradiol. *The Journal of Steroid Biochemistry and Molecular Biology*, 147:10–16, March 2015.

# A Appendix

## A.1 List of chemicals

| Chemical | Supplier |
|---|---|
| DNA aptamers | DNA Technology A/S |
| 6-mercapto-1-hexanol | TCI Chemicals |
| 17$\beta$-estradiol | Sigma-Aldrich |
| Estradiol Glow | Jena Bioscience GmbH |
| Molecular biology grade $H_2O$ | Sigma-Aldrich |
| 99 % ethanol | Sigma-Aldrich |
| TBS | Sigma-Aldrich |
| PBS | Sigma-Aldrich |
| SSC | GIBCO UltraPure |
| NaCl | Sigma-Aldrich |
| KCl | Sigma-Aldrich |
| $CaCl_2$ | Sigma-Aldrich |
| $MgCl_2$ | Sigma-Aldrich |
| HCl | Merck |
| TCEP·HCl | Pierce |
| Tween20 | Sigma-Aldrich |
| UREA | Sigma-Aldrich |
| EDTA | Fluka Analytical |

## A.2 Data sheet: Estradiol Glow

DATA SHEET

Jena Bioscience

# Estradiol Glow

Fluorescently labeled Estradiol

| Cat. No. | Amount |
|---|---|
| PR-958S | 100 µg |
| PR-958L | 500 µg |

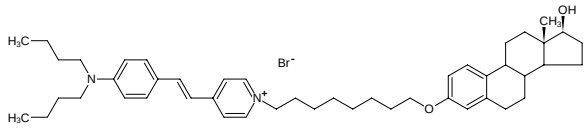


Structural formula of Estradiol Glow

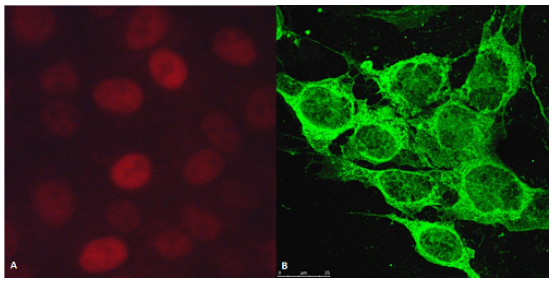


A: Nucl. accumulat. of Estradiol glow in rat paraventricular hypothalamic neurons after *in vivo* i.p. injection. 100 µm vibratome, section of the perfusion fixed brain. B: Cytopl. and nucl. uptake of estradiol glow in MCF7 breast cancer cell culture

**For *in vitro* use only!**

**Shipping:** shipped at 4 °C

**Storage Conditions:** store at 4 °C

**Additional Storage Conditions:** store dark

**Shelf Life:** 12 months

**Molecular Formula:** $C_{47}H_{67}BrN_2O_2$

**Molecular Weight:** 771.95 g/mol

**Purity:** > 97 % (DC, NMR)

**Form:** lyophilized, brownish-red, glassy to waxy appearance

**Solubility:**
High: MeOH, EtOH, PrOH, DMSO, DMF
Moderate: acetone, $CH_2Cl_2$, $CH_3Cl$, THF
Low: $H_2O$ and aqueous buffer systems (after presolution in DMSO >1 µM)
Insoluble: $Et_2O$, hydrocarbons such as hexane, heptane, benzene

**Spectroscopic Properties:**
$\lambda_{exc}$ 467 nm; $\lambda_{em}$ 618 nm; $\epsilon$ 29.0 L mmol$^{-1}$ cm$^{-1}$ (PBS pH 7.4)
$\lambda_{exc}$ 501 nm; $\lambda_{em}$ 596 nm; $\epsilon$ 52.0 L mmol$^{-1}$ cm$^{-1}$ (ethanol)

**Description:**
Estradiol Glow is the ovarian steroid hormone 17-ß-Estradiol labeled with a novel low molecular weight orange/red fluorophor thus retaining its chemical properties and it's biological activity. This allows for a wide range of applications including

- analysis of *in vivo* and *in vitro* steroid uptake in real time
- monitoring of intracellular and subcellular steroid transport
- studies on steroid-binding proteins
- use as tracer for steroid immunoassays (to replace isotopes or enzymes
- photodynamic elimination of estrogen sensitive tissues and cells in experimental settings with possible future clinical implications

Estradiol Glow can be histologically fixed using formaldehyde or glutaraldehyde without any significant loss of fluorescence intensity.

**Background**
Identification of steroid sensitive cells in target tissues has so far been attempted with either radio labelled hormones and autoradiography or with *in situ* hybridization and immuno-histochemistry for receptor proteins. Numerous studies have been performed with steroid hormones labelled with either enzymes, fluorophors or immunogenic markers, all resulting in loss of biological properties and hormonal function. Estradiol Glow is 17-ß-estradiol, labelled in a novel way with a low molecular weight biocompatible fluorophor, thus retaining biological activity of the ovarian hormone. Systemic injections into experimental animals revealed accumulation of the fluorescent steroid in nuclei of

## Estradiol Glow

Fluorescently labeled Estradiol

known estrogen target tissues, including the brain.
Estradiol Glow allows new insights into cellular uptake, intracellular transport and subcellular binding. Mechanisms of rapid steroid actions become transparent on the single cell level.

**Selected References:**

Jirikowski *et al.* (2011) Uptake, intracellular transport and physiological effects of biologically active fluorescent steroids. Rapid Responses to Steroid Hormones. *7th International Meeting, 14-17 September 2011, Crete, Greece.*

## A.3 Data sheet: Estradiol aptamer #1

# Datasheet

DNA Technology
*A Biosearch Technologies Company*

DTU Nanotech
Ørsteds Plads
bygning 345ø/rum 157

2800 Kgs. Lyngby
Danmark
Att. Mr Kasper Frøhling

Customer no.: 55000791

Ref. No.: Kasper Frøhling

| | | |
|---|---|---|
| Store at minus 20°C | For research use only | SPIN VIAL BRIEFLY BEFORE OPENING |
| DNA | | Order no.: 404762 1/1 |

Oligo name: Estradiol aptamer 15/8-13 Oligo ID: 43865

Sequence 5' /5tthio/GCT TCC AGC TTA TTG AAT TAC ACG CAG AGG GTA GCG GCT CTG CGC ATT CAA TTG CTG CGC GCT GAA GCG CGG AAG C 3'

Modifications: 5´Thiol-C6

No of bases: 76

| **Production data** | **Oligo properties** | **Oligo amount** |
|---|---|---|
| Synthesis scale: 0,20 umol | GC content: 56,6 % | $OD_{260}$: 19,0 |
| Purification: HPLC | Tm: 0,0 °C | nmoles: 26,7 |
| Quality control by: LC/MS | Molecular weight: 23913,2 g/mol | Weight: 638,09 µg |

Order date: 15-08-2013 10:00:45
Shipping date: 21-08-2013
Oligo is delivered lyophilized, for a 100 pmol/µL solution dissolve the oligo in 267 µL. in MilliQ

Special notes:

Must be shippe dried

## A.4 Data sheet: Estradiol aptamer #2

# Datasheet

DNA Technology
*A Biosearch Technologies Company*

DTU Nanotech
Ørsteds Plads
bygning 345ø/rum 157

2800 Kgs. Lyngby
Danmark
Att. Mr Kasper Frøhling

Customer no.: 55000791

Ref. No.: Kasper Frøhling

| | | |
|---|---|---|
| Store at minus 20°C | For research use only | SPIN VIAL BRIEFLY BEFORE OPENING |
| DNA | | Order no.: 408374 1/1 |
| Oligo name: Estradiol aptamer S-S #2 | | Oligo ID: 66763 |

Sequence 5' /5ThioMC6-D/ATA CGA GCT TGT TCA ATA CGA AGG GAT GCC GTT TGG GCC CAA GTT CGG CAT AGT GTG GTG ATA GTA AGA GCA ATC 3'

Modifications: 5´Thiol-C6 S-S

No of bases: 75

| **Production data** | **Oligo properties** | **Oligo amount** |
|---|---|---|
| Synthesis scale: 1,00 umol | GC content: 48,0 % | $OD_{260}$: 17,0 |
| Purification: HPLC | Tm: 0,0 °C | nmoles: 22,9 |
| Quality control by: LC/MS | Molecular weight: 23641,6 g/mol | Weight: 540,92 µg |

Order date: 20-08-2014 13:15:39
Shipping date: 29-08-2014

Oligo is delivered lyophilized, for a 100 pmol/µL solution dissolve the oligo in 229 µL.

Special notes:

## A.5 Data sheet: Complementary DNA

# Datasheet

DNA Technology
*A Biosearch Technologies Company*

DTU Nanotech
Ørsteds Plads
bygning 345ø/rum 157

2800 Kgs. Lyngby
Danmark
Att. Mr Kasper Frøhling

Customer no.: 55000791

Ref. No.: Kasper Frøhling

| | | |
|---|---|---|
| Store at minus 20°C | For research use only | SPIN VIAL BRIEFLY BEFORE OPENING |
| DNA | | Order no.: 408598 1/2 |

Oligo name: 17B cDNA DY-776 — Oligo ID: 68274

Sequence 5' /Dy776/GAT TGC TCT TAC TAT CAC 3'

Modifications: Dy-776

No of bases: 18

| **Production data** | **Oligo properties** | **Oligo amount** |
|---|---|---|
| Synthesis scale: 0,20 umol | GC content: 38,9 % | $OD_{260}$: 6,9 |
| Purification: HPLC | Tm: 41,8 °C | nmoles: 16,9 |
| Quality control by: LC/MS | Molecular weight: 6239,6 g/mol | Weight: 105,48 µg |

Order date: 09-09-2014 12:21:46
Shipping date: 19-09-2014

Oligo is delivered lyophilized, for a 100 pmol/µL solution dissolve the oligo in 169 µL.

Special notes:

## A.6 Data sheet: Non-complementary DNA

# Datasheet

DNA Technology
*A Biosearch Technologies Company*

DTU Nanotech
Ørsteds Plads
bygning 345ø/rum 157

2800 Kgs. Lyngby
Danmark
Att. Mr Kasper Frøhling

Customer no.: 55000791

Ref. No.: Kasper Frøhling

| Store at minus 20°C | For research use only | SPIN VIAL BRIEFLY BEFORE OPENING |
|---|---|---|
| DNA | | Order no.: 409068 1/1 |
| Oligo name: ncDNA DY-776 | | Oligo ID: 71445 |
| Sequence 5' /Dy776/AGT CGT CAT GGC AAG GAT 3' | | |
| Modifications: Dy-776 | | |
| No of bases: 18 | | |

| **Production data** | **Oligo properties** | **Oligo amount** |
|---|---|---|
| Synthesis scale: 0,20 umol | GC content: 50,0 % | $OD_{260}$: 7,6 |
| Purification: HPLC | Tm: 52,1 °C | nmoles: 18,1 |
| Quality control by: LC/MS | Molecular weight: 6537,7 g/mol | Weight: 118,41 µg |

Order date: 20-10-2014 10:46:23
Shipping date: 27-10-2014
Oligo is delivered lyophilized, for a 100 pmol/µL solution dissolve the oligo in 181 µL.

Special notes:

## A.7 Pure MCH peak-fitting

Histograms of peak-fitting of the double peak of MCH at 1060 $cm^{-1}$ and 1085 $cm^{-1}$ seen in Figure 4.24.

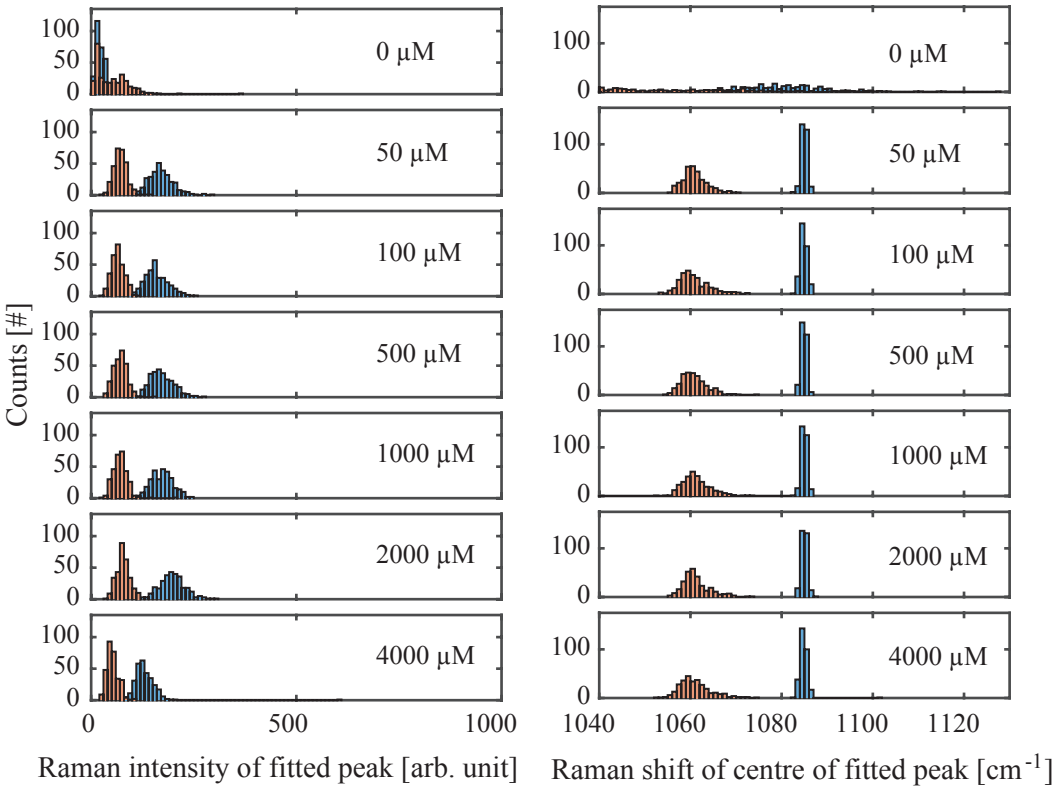

## A.8 Effect of MCH incubation time

Repeat measurement of varying MCH incubation time (see Figure 4.30) (batch: KF7-1).

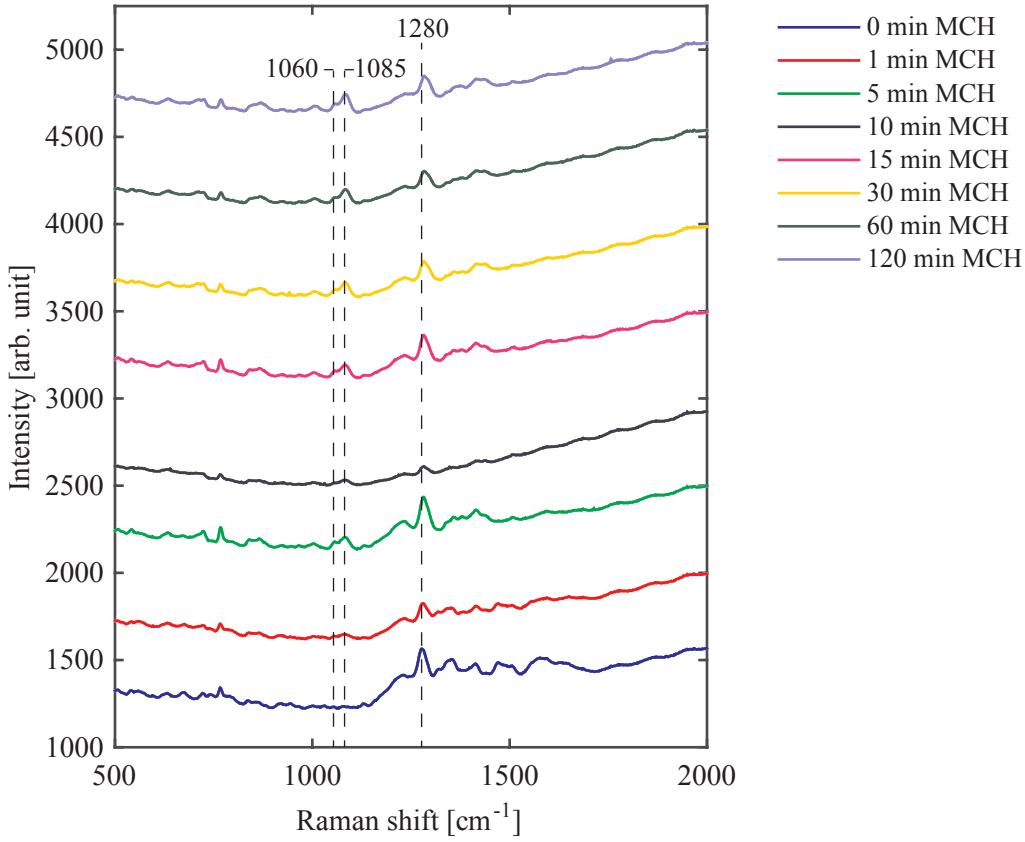

## A.9 17$\beta$-estradiol 808 cm$^{-1}$ peak

Peak-fitting of the 808 cm$^{-1}$ peak observed for 17$\beta$-estradiol in Figure 4.31 and Figure 4.32.

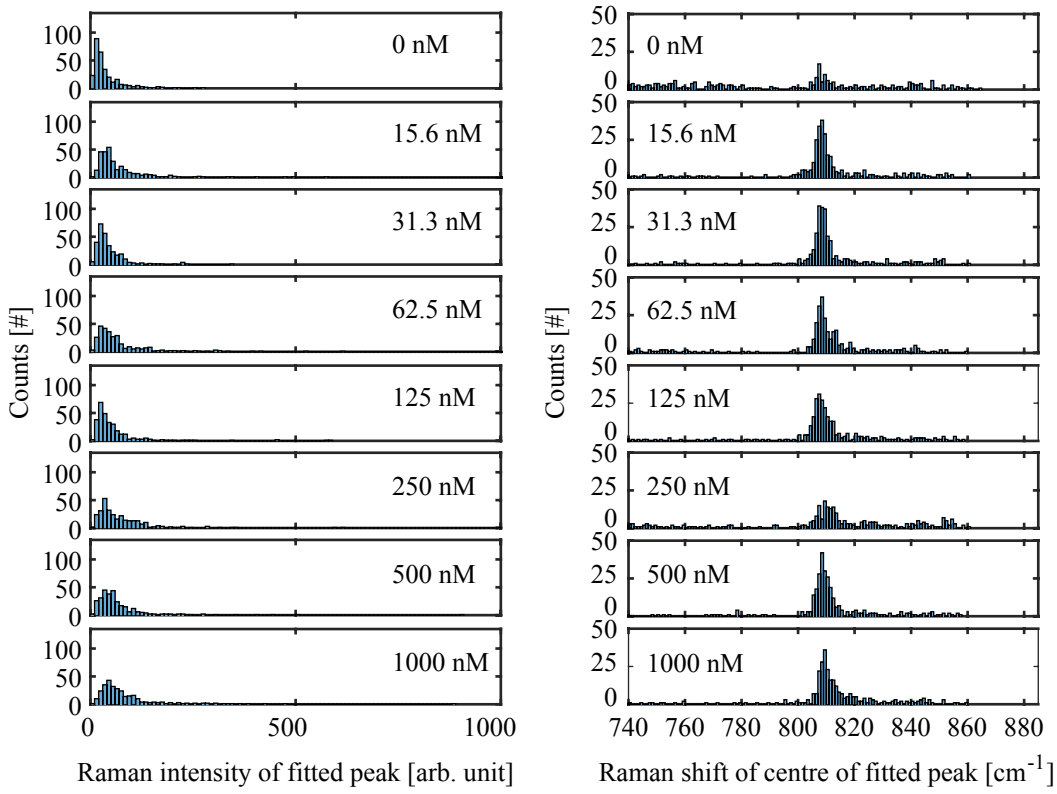

## A.10 Pure 17$\beta$-estradiol detection

Repeated measurement of varying 17$\beta$-estradiol concentration in ethanol on batch KF8-1 (see Figure 4.33).

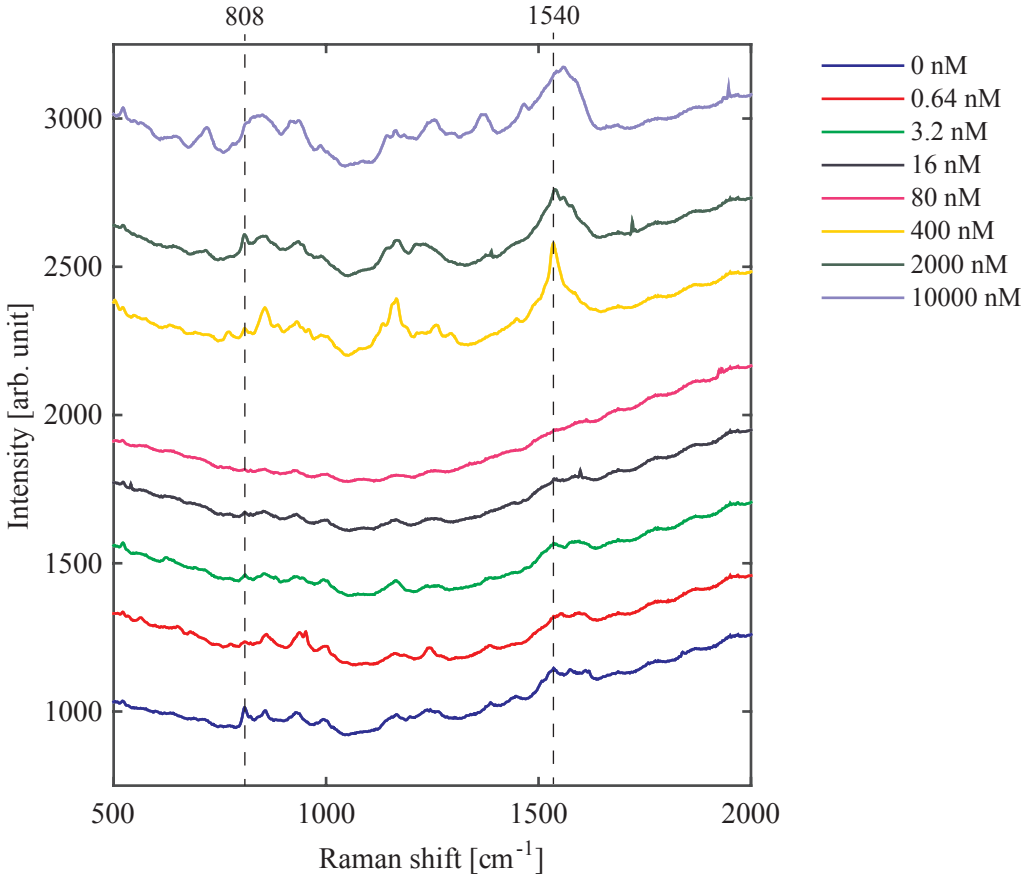

*An expert is a man who has made all the mistakes which can be made in a very narrow field.*

- Niels Bohr

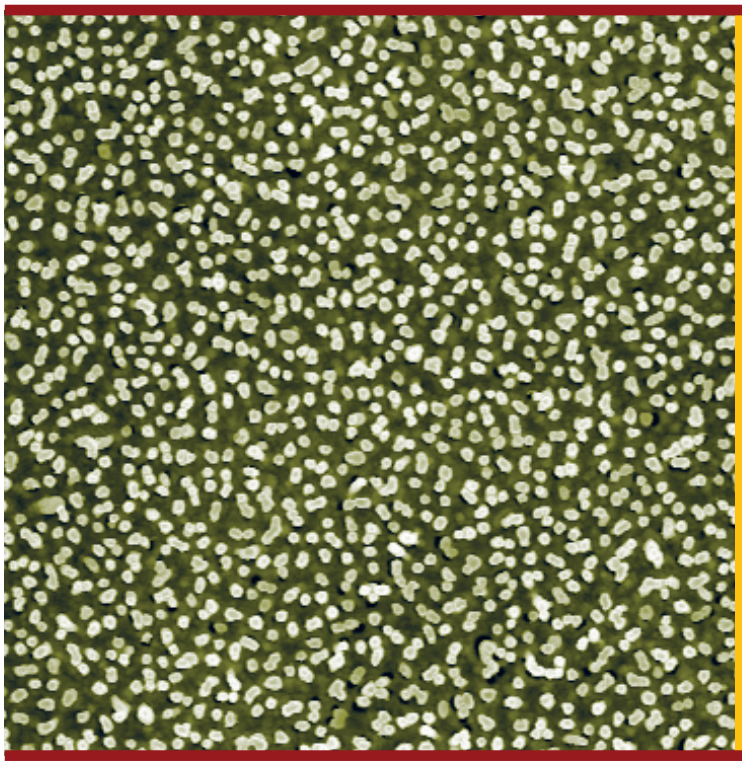



Published by:
DTU Nanotech
Department of Micro- and Nanotechnology
Technical University of Denmark
Ørsteds Plads, building 345B
DK-2800 Kgs. Lyngby